

SIMULATION OF THE DYNAMIC BEHAVIOR OF AN EXCAVATOR DUE TO
INTERACTING MECHANICAL AND HYDRAULIC DYNAMICS

ONESMUS MUTUKU MUVENGEI

MASTER OF SCIENCE

(Mechanical Engineering)

JOMO KENYATTA UNIVERSITY OF
AGRICULTURE AND TECHNOLOGY

2008

Simulation of the Dynamic Behavior of an Excavator due to Interacting
Mechanical and Hydraulic Dynamics

Onesmus Mutuku Muvengi

A thesis submitted in partial fulfilment for the Degree of Master of Science in
Mechanical Engineering in the Jomo Kenyatta University of Agriculture and
Technology

2008

DECLARATION

This thesis is my original work and has not been presented for a degree in any other University.

Signature:..... Date.....

Onesmus Mutuku Muvengei

This thesis has been submitted for examination with my approval as the University Supervisor.

Signature:..... Date.....

Eng. Prof. John M. Kihiu

JKUAT, Kenya

DEDICATION

This work is dedicated to my wife Jedidah and our daughter Mũtheu, for the joy they brought to my life.

ACKNOWLEDGEMENTS

I first and foremost thank the almighty God for availing this study opportunity and for keeping me in good health throughout the study period. I wish to wholeheartedly thank my Supervisor Eng. Prof. J.M. Kihuu for his invaluable guidance, assistance, constructive criticism, scheduled and unscheduled discussions throughout the realization of my Master's degree. I truly appreciate his time, wisdom, effort not only in the preparation of this thesis, but in all aspects of academic life.

I would like to sincerely thank the Chairman of Mechanical Engineering Department, Dr. Karanja Kibicho for the wise words of encouragement and for making my research proposal be processed in time. I would also like to thank Doris Ratemo, my former undergraduate classmate, for the journal articles she downloaded and forwarded to me while in her stay in United Kingdom. Also lot of thanks goes to Mr. Evans Kibiro for his kind assistance in the Computer Laboratory and departmental library. I also wish to sincerely thank the 20-sim group for the trial version they made available to me, which greatly helped me in appreciating the simulation concept of bond graphs. To James Kuria and Zachary Kithinji, your companionship, comments and suggestions cannot go unmentioned. My thanks are also due to my colleagues in the department of Mechanical Engineering, and my friends wherever they are, for their encouragement and support throughout the course of this work. Finally, my very special thanks go to my entire family for their love, patience, support and understanding during my studies.

This work has been made possible by the financial support from the Jomo Kenyatta University of Agriculture and Technology. I owe gratitude to them for this support.

TABLE OF CONTENTS

DECLARATION	i
DEDICATION	ii
ACKNOWLEDGEMENTS	iii
TABLE OF CONTENTS	iv
LIST OF TABLES	ix
LIST OF FIGURES	x
LIST OF APPENDICES	xviii
LIST OF ABBREVIATIONS	xix
LIST OF SYMBOLS	xx
LIST OF SUBSCRIPTS	xxii
ABSTRACT	xxiii
CHAPTER 1	1
INTRODUCTION	1
1.1 Background Information	1
1.2 Problem Statement	3
1.3 Objectives	5
1.4 Organization of the Thesis	5
CHAPTER 2	7
LITERATURE REVIEW	8
2.1 Dynamic Modeling of Excavators.	8
2.2 Manipulator Dynamics	10

2.2.1	Newton-Euler Method	10
2.2.2	Lagrangian Method	11
2.2.3	Kane's Method	12
2.2.4	Bond Graph Method	12
2.3	Modeling Soil-tool Interaction in Excavators	13
2.4	Summary	15
CHAPTER 3	16
MODELING THE MANIPULATOR DYNAMICS	16
3.1	Bond Graph Model Development	16
3.1.1	Kinematic Analysis of the Excavator Manipulator	17
3.1.2	Forward Recursive Equations	21
3.1.2.1	Angular Velocity	21
3.1.2.2	Translational Velocity of the Origin of Link Coordinate Frame	22
3.1.2.3	Translational Velocity of the Center of Mass of a Link	22
3.1.2.4	Applying the Recursive Equations to the Boom Link $i = 2$	23
3.1.2.5	Applying the Recursive Equations to the Arm Link $i = 3$	27
3.1.2.6	Applying the Recursive Equations to the Bucket Link $i = 4$	33
3.1.3	Modeling the Bucket Digging Force	38
3.1.4	A Non Causal Bond Graph Model of the Manipulator's Dynamics	45

3.2	Checking the Model	46
CHAPTER 4	51
	MODELING THE DYNAMICS OF HYDRAULIC ACTUATION	
	OF THE EXCAVATOR	51
4.1	Bond Graph Model Development	51
4.1.1	Pump	53
4.1.2	Spool Valves	53
4.1.3	Linear Cylinders	58
4.1.3.1	Modeling Compressibility of Oil in a Hydraulic Cylinder	60
4.1.3.2	Modeling the Leakage Flows	63
4.1.3.3	Modeling the Viscous Friction	63
4.1.4	Bond Graph Model of a Valve Controlled Cylinder	64
4.2	Checking the Bond Graph Model	64
4.3	Inter-Actuator Interaction	69
CHAPTER 5	78
	DYNAMIC COUPLING OF THE MECHANICAL AND HYDRAULIC	
	MODELS OF THE EXCAVATOR	78
5.1	Introduction	78
5.2	Deriving the Jacobi Expressions for the Manipulator	79
5.2.1	Boom Link	80
5.2.2	Arm Link	82
5.2.3	Bucket Link	84

5.3 Overall Bond Graph Model of the Hydraulic and Mechanical Dynamics	86
CHAPTER 6	90
SYSTEM ANALYSIS AND DESIGN USING INVERSE DYNAMICS	90
ICS	90
6.1 Introduction	90
6.2 Parameter Identification	90
6.2.1 Boom Link Parameters	91
6.2.2 Bucket Link Parameters	92
6.2.3 Arm Link Parameters	93
6.3 Trajectory Planning	94
6.4 Simulink Model for the Inverse Dynamics of the 3 DOF System	97
6.5 Torque Profiles	100
6.6 Power Profiles	104
6.7 Force Profiles	108
6.8 Sizing the Hydraulic Actuators and Valves Based on Inverse Dynamics	109
6.8.1 Pressure Drop Profiles	110
6.8.2 Actuator Sizing	112
6.8.3 Flow Profiles	114
6.8.4 Valve Sizing	116
CHAPTER 7	121
DYNAMIC RESPONSE USING FORWARD DYNAMICS	121
7.1 Introduction	121
7.2 Block Expansion	121

7.3	Transient and Steady-State Responses	125
7.3.1	Link Angular Velocity and Displacement Responses	126
7.3.2	Piston Velocity and Displacement Responses	127
7.3.3	Flow Rate Responses	128
7.3.4	Pressure Responses at the Cylinder Chambers	129
CHAPTER 8	132
CONCLUSIONS AND RECOMMENDATIONS	132
8.1	Conclusions	132
8.2	Recommendations for Future Work	134
REFERENCES	136
APPENDIX	143

LIST OF TABLES

Table 3.1	Structural kinematic parameters	19
Table 4.1	Hydraulic cylinder parameters	65
Table 4.2	Pump, valve and hydraulic parameters	66
Table 6.1	Boom link geometric parameters	92
Table 6.2	Bucket link geometric parameters	93
Table 6.3	Arm link geometric parameters	94
Table 6.4	Manipulator motion cases	101
Table A.1	Generalized variables for each energy domain.	144
Table A.2	Causal properties for bond graph elements.	153
Table A.3	Block diagram expansion for bond graph elements	157

LIST OF FIGURES

Figure 1.1	Schematic drawing of a part of assembled excavator	2
Figure 1.2	Schematic drawing of a part of hydraulic circuit of the excavator	3
Figure 3.1	Coordinate System assignment for excavator	18
Figure 3.2	Kinematic analysis for the boom link	23
Figure 3.3	Bond graph representation of the boom's mechanical dynamics	27
Figure 3.4	Kinematic analysis for the arm link	28
Figure 3.5	Bond graph representation of the arms's mechanical dynamics	32
Figure 3.6	Kinematic analysis for the bucket link	33
Figure 3.7	Bond graph representation of the buckets's mechanical dynamics	38
Figure 3.8	Wedge model that accounts for the material being retained in the bucket	39
Figure 3.9	The variation of N_w factor with the slip angle β_d	41
Figure 3.10	Bucket digging force at the tip	42
Figure 3.11	Bond graph representation of velocity of the buckets's tip .	45
Figure 3.12	A non causal bond graph model representing the mechanical dynamics of the manipulator	46
Figure 3.13	A two link planar manipulator	47
Figure 3.14	A non causal bond graph model representing the mechanical dynamics of a 2-link manipulator	49
Figure 4.1	Schematic diagram of a valve controlled hydraulic cylinder .	52

Figure 4.2	Constant pressure pump bond graph model	53
Figure 4.3	Variation of valve orifice area with spool movement	56
Figure 4.4	Bond graph representation of valve resistance to forward flow	58
Figure 4.5	Bond graph representation of valve resistance to return flow	58
Figure 4.6	Schematic diagram of the linear actuator	59
Figure 4.7	Bond graph representation of the pressure difference in cylinder chambers	60
Figure 4.8	<i>C</i> -element representing fluid compressibility	61
Figure 4.9	Displacement Modulated <i>C</i> element	62
Figure 4.10	Displacement Modulated <i>C</i> element of cylinder chamber A	62
Figure 4.11	Displacement Modulated <i>C</i> element of cylinder chamber B	62
Figure 4.12	Bond graph model representing the leakage in piston and cylinder wall clearance	63
Figure 4.13	Bond graph model representing the viscous friction due to piston movement	64
Figure 4.14	A causal bond graph model for the cylinder during extension	65
Figure 4.15	Simulated open loop responses of the arm cylinder for extension case; (a) Head side chamber pressure (b) Rod side chamber pressure (c) Piston displacement (d) Piston velocity	68
Figure 4.16	Simulated open loop responses of the arm cylinder for retraction case; (a) Head side chamber pressure (b) Rod side chamber pressure (c) Piston displacement (d) Piston velocity	69
Figure 4.17	Hydraulic circuit for two cylinders powered by one pump .	71

Figure 4.18	Bond graph models of two hydraulic cylinders powered by one pump	72
Figure 4.19	Simulated open loop responses for case 1; (a) Piston displacements (b) Piston velocities (c) Pump flow rate (d) Flow rate to cylinders (e) Head sides chamber pressures (f) Rod side chamber pressures	73
Figure 4.20	Simulated open loop responses for case 2; (a) Piston displacements (b) Piston velocities (c) Pump flow rate (d) Flow rate to cylinders (e) Head sides chamber pressures (f) Rod side chamber pressures	74
Figure 4.21	Simulated open loop responses for case 3; (a) Piston displacements (b) Piston velocities (c) Pump flow rate (d) Flow rate to cylinders (e) Head sides chamber pressures (f) Rod side chamber pressures	75
Figure 4.22	Simulated open loop responses for case 4; (a) Piston displacements (b) Piston velocities (c) Pump flow rate (d) Flow rate to cylinders (e) Head sides chamber pressures (f) Rod side chamber pressures	77
Figure 5.1	Dynamic coupling between the mechanical and hydraulic systems of an excavator	78
Figure 5.2	Boom cylinder length	80
Figure 5.3	Coupling the hydro-mechanical dynamics of the boom link .	82
Figure 5.4	Arm cylinder length	82
Figure 5.5	Coupling the hydro-mechanical dynamics of the arm link .	84

Figure 5.6	Bucket cylinder length	84
Figure 5.7	Coupling the hydro-mechanical dynamics of the bucket link	86
Figure 5.8	Non-causal bond graph model of the excavating mechanism	87
Figure 5.9	Causal bond graph model of the excavating mechanism . . .	89
Figure 6.1	Schematic diagram of the boom link	91
Figure 6.2	Schematic diagram of the bucket link	92
Figure 6.3	Schematic diagram of the arm link	93
Figure 6.4	(a) Boom link's angular displacement trajectory (b) Arm link's angular displacement trajectory (c) Bucket link's angular displacement trajectory	96
Figure 6.5	(a) Boom link's angular velocity trajectory (b) Arm link's angular velocity trajectory (c) Bucket link's angular velocity trajectory	97
Figure 6.6	(a) Boom link's angular acceleration trajectory (b) Arm link's angular acceleration trajectory (c) Bucket link's angular acceleration trajectory	97
Figure 6.7	The overall Simulink block for the inverse dynamics	98
Figure 6.8	The Simulink block for computing the joint torques using inverse dynamics	99
Figure 6.9	The torque profiles at joints, when the manipulator is moving in a free space and for REE case; (a) Boom joint torque (b) Arm joint torque (c) Bucket joint torque	102

Figure 6.10	The torque profiles at joints, when the manipulator is moving in a free space and for ERR case; (a) Boom joint torque (b) Arm joint torque (c) Bucket joint torque	102
Figure 6.11	The torque profiles at manipulator joints, when the bucket is digging a sandy-loom soil; (a) Boom joint torque (b) Arm joint torque (c) Bucket joint torque	104
Figure 6.12	(a) Boom joint power (b) Arm joint power (c) Bucket joint power (d) Total joints power ;when the manipulator is moving in free space and at the initial cycle times	105
Figure 6.13	(a) Boom joint power (b) Arm joint power (c) Bucket joint power (d) Total joints power ;when the bucket is digging a sandy-loom soil and at the initial cycle times	106
Figure 6.14	(a) Boom joint power (b) Arm joint power (c) Bucket joint power (d) Total joints power ;when the manipulator is digging a sandy-loom soil and at the optimal cycle times	107
Figure 6.15	(a) Boom cylinder force profile (b) Arm cylinder force profile (c) Bucket cylinder force profile; when the manipulator is moving in a free space	108
Figure 6.16	(a) Boom cylinder force profile (b) Arm cylinder force profile (c) Bucket cylinder force profile; when the bucket is digging a sandy-loom soil	109

Figure 6.17	The Pressure drop profiles across the cylinders, when the bucket is digging a sandy-loam soil and at original piston diameters; (a) Boom cylinder (b) Arm cylinder (c) Bucket cylinder	110
Figure 6.18	The Pressure drop profiles across the cylinder valves, when the bucket is digging a sandy-loam soil and at optimal piston diameters; (a) Boom cylinder valve (b) Arm cylinder valve (c) Bucket cylinder valve	111
Figure 6.19	The pressure drops versus piston diameters; (a) Boom cylinder (b) Arm cylinder (c) Bucket cylinder	113
Figure 6.20	The Pressure drop profiles across the cylinders, when the bucket is digging a sandy-loam soil and at optimal piston diameters; (a) Boom cylinder (b) Arm cylinder (c) Bucket cylinder	113
Figure 6.21	The Pressure drop profiles across the cylinder valves, when the bucket is digging a sandy-loam soil and at optimal piston diameters; (a) Boom cylinder valve (b) Arm cylinder valve (c) Bucket cylinder valve	114
Figure 6.22	(a) Total flow rate profile (b) Flow rate profile to boom cylinder (c) Flow rate profile to arm cylinder (d) Flow rate profile to bucket cylinder	115

Figure 6.23	Pressure drops versus flow curves, when the manipulator is moving in a free space and at the initial sizes of the valve's orifices; (a) Boom cylinder valve (b) Arm cylinder valve (c) Bucket cylinder valve	118
Figure 6.24	Pressure drops versus flow curves, when the bucket is digging a sandy-loam soil and at the initial sizes of the valve's orifices; (a) Boom cylinder valve (b) Arm cylinder valve (c) Bucket cylinder valve	118
Figure 6.25	Pressure drops versus flow curves, when the manipulator is moving in a free space and at the optimal sizes of the valve's orifices; (a) Boom cylinder valve (b)Arm cylinder valve (c) Bucket cylinder valve	119
Figure 6.26	Pressure drops versus flow curves, when the bucket is digging a sandy-loam soil and at the optimal sizes of the valve's orifices; (a) Boom cylinder valve (b)Arm cylinder valve (c) Bucket cylinder valve	120
Figure 7.1	The Simulink block diagram representing the bond graph model of the interacting hydraulic and mechanical dynamics	122
Figure 7.2	The Simulink block for the hydraulic dynamics	123
Figure 7.3	The Simulink block for the mechanical subsystem dynamics	124
Figure 7.4	The input command to the system	126
Figure 7.5	The simulated angular velocity and displacement responses for; (a) Boom link (b) Arm link (c) Bucket link	126

Figure 7.6	The simulated piston velocity and displacement responses for; (a) Boom cylinder (b) Arm cylinder (c) Bucket cylinder	127
Figure 7.7	The simulated flow rate response; (a) Flow rate responses to individual cylinders (b) Total flow rate	128
Figure 7.8	The simulated head and rod side pressure responses for; (a) Boom cylinder (b) Arm cylinder (c) Bucket cylinder	130
Figure A.1	Bond Representation	143
Figure A.2	SE and SF-element representation	145
Figure A.3	C and I-elements representation	146
Figure A.4	R-element representation	147
Figure A.5	0-junction representation	148
Figure A.6	1-junction representation	149
Figure A.7	Transformer and Gyrator element representation	149
Figure A.8	Definition of the causal stroke	151

LIST OF APPENDICES

APPENDIX A: BOND GRAPH MODELING 143

LIST OF ABBREVIATIONS

<i>BG</i>	Bond graph
<i>CAMP – G</i>	Computer Aided Modeling Program with Graphical input
<i>DYMOLA</i>	Dynamic Modeling Laboratory
<i>HYLIB</i>	Hydraulic Library
<i>MATLAB</i>	Matrix Laboratory
<i>ODE</i>	Ordinary Differential Equation
<i>SCAP</i>	Sequential Causality Assignment Procedure
<i>TUTSIM</i>	Technical University of Twente Simulation
20 – <i>SIM</i>	Twente Simulation

LIST OF SYMBOLS

Symbols

A_O	Area of the orifice opening	m^2
A_p	Cross section area of the piston	m^2
A_r	Cross section area of the rod	m^2
A_1	Cross section area of the piston at head side chamber	m^2
A_2	Cross section area of the piston at rod side chamber	m^2
c	Radial clearance between the piston and cylinder bore	m
C_A	Fluid compliance at the head side of the hydraulic cylinder	m^3/Pa
C_B	Fluid compliance at the rod side of the hydraulic cylinder	m^3/Pa
C_d	Discharge coefficient of the spool orifice.	
D_p	Diameter of the cylinder piston	m
D_r	Diameter of the cylinder rod	m
J_i	Mass inertia of link i , for $i = 2, 3, 4$ about the centroid	kg/m^2
K_q	Flow gain of the directional control valve	m^2/s
L_{AB}	Length of line segment from point A to B	m
L_{cy}	Length of the cylinder chamber	m
L_p	Length of the cylinder piston	m
M_i	Mass of link i , for $i = 2, 3, 4$	kg
M_p	Mass of the cylinder piston and rod	kg
P_A	Pressure at the head side of the cylinder	Pa
P_B	Pressure at the rod side of the cylinder	Pa
P_L	Pressure drop across the cylinder	Pa
P_S	Pump supply pressure	Pa
P_r	Return pressure	Pa

Q_A	Fluid flow to the head side of the cylinder	m^3/s
Q_B	Fluid flow from the rod side of the cylinder	m^3/s
Q_{il}	Internal leakage flow in the cylinder	m^3/s
r	Radius of the inlet port of the directional control valve	m
R_{il}	R-element representing the internal leakage coefficient	Nm/s
R_N	R-element representing the viscous friction	Ns/m
v_{G_ix}	Horizontal component of the mass center's velocity of the i^{th} link, referenced to the base frame	m/s
v_{G_iy}	Vertical component of the mass center's velocity of the i^{th} link, referenced to the base frame	m/s
x	Linear displacement of the piston	m
\dot{x}	Linear velocity of the piston	m/s
y_d	Overlap of the directional control valve	m
y_v	Linear displacement of the directional control valve	m

Greek Symbols

β	Bulk modulus of the hydraulic fluid	Pa
θ_i	Joint variables of the links	rad
$\dot{\theta}_i$	First time derivative of the joint variable	rad/s
ρ	Mass density of the hydraulic fluid	kg/m^3
μ	Absolute viscosity of the hydraulic fluid	m^2/s

LIST OF SUBSCRIPTS

<i>a</i>	Arm
<i>bo</i>	Boom
<i>bu</i>	bucket

ABSTRACT

This research project primarily describes the modeling of mechanical and hydraulic dynamics of an excavating mechanism previously designed to be used with small tractors, which are fabricated in the Engineering Workshops of Jomo Kenyatta University of Agriculture and Technology. The developed models were then used to optimize the hydraulic system design, and also to simulate the open loop transient and steady state responses of the system.

In this study, bond graph method was chosen as the modeling method because, firstly, it is a domain-independent graphical method of representing the dynamics of physical systems. Therefore, systems from different engineering disciplines can be described in the same way. Secondly, the available literature shows that the method being relatively new, has not been thoroughly applied to model the dynamics of nonlinear systems such as excavators. The bond graph method was first reviewed, and then used to develop a complete dynamic model of the excavator by modeling the hydraulic actuation system and the manipulator linkage separately. The two models representing different domain dynamics were coupled to a complete model using appropriate manipulator jacobians which were treated as Modulated Transformer Elements. The bond graph method was found to reduce significantly the number of recursive computations performed on a manipulator for a mechanical dynamic model to result. This indicated, that bond graph method is more computationally efficient than the Newton-Euler method in developing dynamic models of manipulators.

The mechanical bond graph model of the manipulator was verified by comparing the joint torque expressions of a two link planar manipulator to those obtained by using Newton-Euler and Lagrangian methods as analyzed in robotic textbooks. The expressions were found to agree indicating that the model captures the aspects of

rigid body dynamics of the manipulator. Also the bond graph model of the hydraulic system was verified by comparing the open loop state responses to those of an ODE model which has been developed in literature based on the same assumptions. The results were found to correlate very well both in the shape of the curves, magnitude and the response times, thus indicating that the developed model represents the hydraulic dynamics of a valve controlled cylinder.

Based on the model developed, actuator sizing and valve sizing methodologies were developed and used to obtain the optimal sizes of the pistons and spool valve ports respectively. It was found that using the pump with the sized flow rate capacity, the engine of the tractor is able to power the excavating mechanism in digging a sandy-loam soil. The causal bond graph model of the excavator was expanded into block diagrams and simulated on MATLAB/SIMULINK to determine the transient and steady state responses of the system. From the responses obtained, the model developed was found to capture the inter-component interactions and also the interaction between the hydraulic and mechanical dynamics. Therefore it can be concluded that the model developed can be used to design control laws necessary for controlling the dynamics and motions of the excavating manipulator.

CHAPTER 1

INTRODUCTION

1.1 Background Information

The excavating mechanism designed in [1] will be used with the small tractors which are fabricated in the Engineering Workshops of Jomo Kenyatta University of Agriculture and Technology in digging medium-height trenches for small scale farmers. When the mechanism is attached to the tractor, a small excavator will be obtained whose common structure consists of a swing body and a front manipulator as shown in Figure 1.1. The boom, arm and bucket will be the three main links comprising the front manipulator of the excavator, and their motions together with the swing motion will be the most frequent motions of the excavator during the digging operation.

Since digging is typically a planar motion, only the last three degrees of freedom, that is the bucket, arm and boom motions are modeled. The boom, arm, and bucket are controlled by extending or retracting the hydraulic actuators across each joint. A pressure compensated, axial piston pump will provide hydraulic power to the excavating mechanism at a constant pressure. A constant pressure system has a mechanism to keep constant pressure supplied by the pump, while varying the flow rate to one or more actuators. A small pilot flow is maintained from the pump through the closed center control valve to the pump compensator. This pilot flow forces the pump to deliver little flow at a minimum pressure in a stand-by position [2]. A part of the hydraulic circuit which controls the boom, arm and bucket links is shown in Figure 1.2.

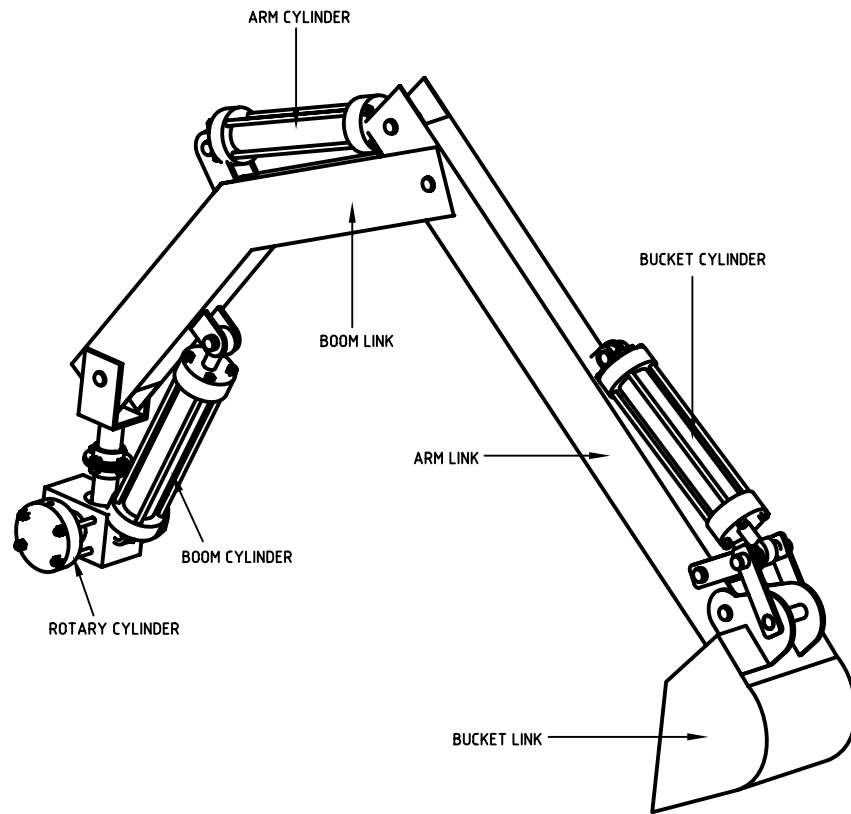


Figure 1.1: Schematic drawing of a part of assembled excavator

Assessment of dynamical performance of an engineering product is important prior to its manufacture in order to optimize and verify design. Currently, computer simulations of dynamic behavior of an engineering system is indispensable in the design of a new product and has replaced manufacturing of prototypes. In simulation of a systems dynamic behavior, a model which captures the essential dynamic aspects of the system is required. The product whose dynamic behavior will be simulated to assess some design aspects in this project is an excavator, which has a manipulator directly driven by hydraulic actuators. Since the hydraulic system controlling the manipulator has its own dynamics due to compressibility of hydraulic oil, and has highly nonlinear characteristics due to spool valve dynamics, it is necessary to

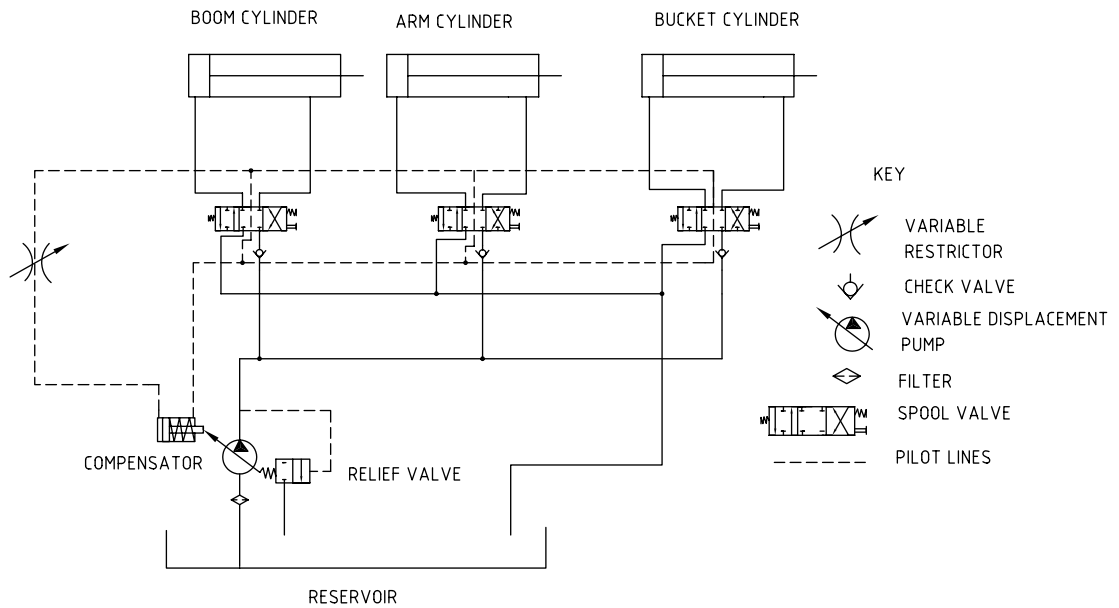


Figure 1.2: Schematic drawing of a part of hydraulic circuit of the excavator

consider its effect on the overall dynamic behavior of the excavator.

The dynamical behavior of 3-dimensional mechanical systems and which consist of hydraulic components are hard to predict since they are made of sub-systems from two different engineering domains, i.e., hydraulics and mechanics [3]. Therefore a modeling technique which takes into account the interaction of various engineering domains is of great help in the development of a model which is simple enough to understand, compute and analyze, and at the same time detailed enough to capture all essential dynamic aspects within a particular operating condition.

1.2 Problem Statement

A dynamic model which incorporates both the mechanical and hydraulic dynamics is essential for dynamic-related studies of an excavator. Therefore a simulation environment for an excavator in which not only the mechanical dynamics, but also the

hydraulic actuator dynamics can be considered, plays an essential role in studying the overall dynamic behavior of the excavator.

Most researchers in the area of modeling of the interacting hydraulic and mechanical dynamics of the excavators have utilized two different modeling techniques, one for mechanical dynamics and the other for hydraulic dynamics [4, 5]. The two models are then coupled to form a complete model for simulation. On introduction and development of bond graph modeling technique, the problem of modeling a multi-domain system has been solved, and now a model representing several sub-models from various engineering disciplines can be simulated using one simulation environment such as MATLAB/SIMULINK, 20-SIM, CAMP-G, etc.

The available literature shows that bond graph modeling of the excavator which is a highly nonlinear system has not been studied thoroughly. Several researchers [6, 7] have used bond graphs to model the dynamics of excavator due to the interacting mechanical and hydraulic dynamics, by putting emphasis on the boom motion. Therefore, there is need to simulate simultaneous motions of the swing, boom, arm and bucket so as to realize full excavating motion using bond graphs. Up to now no documented evidence is available to show that this has been achieved.

Moreover, the compressibility of the hydraulic fluid has been neglected in the previous works on bond graph modeling of the excavator dynamics. This has been done purposely to simplify the bond graph model of the excavator although the dynamic performance of the hydraulic system is not fully addressed.

In this research work, the mechanical and hydraulic dynamic models for the boom, arm and bucket motions will be developed using bond graphs, while at the same

time considering the compressibility of hydraulic fluid in the hydraulic cylinders.

1.3 Objectives

The principal objective of this research project is to develop dynamic models of an excavator, which will be used to size the hydraulic components and simulate the transient responses due to the interacting mechanical and hydraulic dynamics. In pursuing this principal objective, the following will be accomplished;

1. To develop first order bond graph model that includes the interactive mechanical and hydraulic dynamics by;
 - Modeling the mechanical dynamics of the manipulator linkage.
 - Modeling the hydraulic dynamics of the hydraulic system used to actuate the manipulator joints.
 - Integrating the two models using the appropriate manipulator jacobians.
2. To perform inverse dynamics on the model developed in 1 above in order to determine the optimal sizes of the pistons and spool valves for the hydraulic system actuating the manipulator links.
3. To perform forward dynamics on the model developed in 1 above in order to simulate the transient and steady state responses of the system.

1.4 Organization of the Thesis

A short description of the chapters following this introduction is presented below,

1. In Chapter 2, a brief review of the available literature on dynamic modeling

of excavators, modeling manipulator dynamics and modeling the bucket-soil interaction is presented.

2. The bond graph model representing the mechanical dynamics of the manipulator is developed in Chapter 3. The model is developed by representing the kinematic relationships between the joint variable time rates and the translational velocities of the links' centers of mass in bond-graphic form, while considering the links' momenta and weights as the bond graph elements. The validity of the developed model is verified in this chapter.
3. The bond graph model representing the hydraulic dynamics of the actuation system of the manipulator is presented in Chapter 4. The model is developed by modeling the pump, spool valves and hydraulic cylinders separately, and then assembling the sub models to complete models representing the dynamics of valve controlled cylinders. Validation of the developed model, and also a simplified model of the inter-actuator interaction are also presented in this chapter.
4. Chapter 5 presents the overall computational model of the excavator, which is obtained by coupling the mechanical and hydraulic models into a complete model using appropriate manipulator jacobians. The derivative causality resulting in the model is solved in order to obtain a model which can be solved numerically.
5. The hydraulic system design is analyzed in Chapter 6. Quintic polynomial trajectory is planned for the manipulator motion, and then by performing inverse dynamics on the developed model, the joint torques required to accomplish the

planned motion are determined. Actuator sizing and valve sizing methodologies are developed and used to obtain the optimal sizes of the pistons and spool valve ports respectively. Also the joints power requirements are presented and then used to determine the flow rate capacity of the hydraulic pump.

6. The transient and steady state open loop responses of the excavator model are simulated in Chapter 7 to check if the developed model captures the interactive dynamics of the excavator. The bond graph model is expanded into block diagrams which are simulated in MATLAB/SIMULINK.
7. Chapter 8 presents a summary of the main findings of this study as well as areas requiring future attention.

CHAPTER 2

LITERATURE REVIEW

2.1 Dynamic Modeling of Excavators.

Most of research work on excavator dynamics has primarily considered the manipulator dynamics [8–10]. Only a few researchers have considered the interactive hydraulics and mechanical dynamics of excavators [4, 5, 11]. The complication of coupled dynamics and the computational difficulty have prevented the progress of research in this field [12]. Koivo et al. [8] developed a dynamic model of an excavator using Newton-Euler equations to each link in succession, and used this model to design a proportional-differential controller that made the bucket to track a specified trajectory. The model only considered the mechanical dynamics of the manipulator but did not consider nonlinearities of the interacting hydraulic dynamics.

3-Dimensional mechanical systems consisting of hydraulic components like excavators, are difficult to simulate. Usually two different modeling techniques, one for mechanical dynamics and the other for the hydraulic dynamics, have been used and then coupled to a complete model which is then simulated using a single software. Cheol-Gyu et al. [4] presented a simulation environment for excavator dynamics by coupling the MSC.ADAMS mechanical dynamic model of the excavator and the Ordinary Differential Equation's hydraulic system model, and then simulating the overall model on SIMULINK. Beater et al. [5] demonstrated how to model the dynamics of an excavator by modeling the mechanical part using Modelica language, and modeling the dynamics of the hydraulic system using HYLIB language, then integrating the two models and simulating the output model using DYMOLA 2003 simulation software. Nguyen [11] modeled the mechanical dynamics of the excavator

using Newton-Euler method and the hydraulic dynamics using ordinary differential method.

The integration of models from different domains have proved to be a complex and time consuming task, because, although powerful simulation libraries exist, they are generally based on different modeling languages, almost invariably not compatible [3]. Also, the integration of two modeling techniques leads to unnecessary numerical problems and the resulting model may contain fragile interfaces which affect the simulation results.

The bond graph method was established as a new approach to model, analyze and control various dynamical systems by Professor Henry Paynter [13]. Through bond graph modeling technique, the problem of coupling several models from different engineering systems has been solved, and now a model representing several sub-models from various engineering disciplines can be simulated using one simulation environment such as MATLAB/SIMULINK, 20-SIM, CAMP-G, et cetera. Since Prof. Paynter introduced the basic concept of bond graph modeling, bond graphs have been a topic of research or are being used in research on modeling and simulation of dynamic behavior of physical systems.

Margolis et al. [14] contributed to the field of bond graphs by carrying out a comprehensive research, the outcomes of which are applicable to areas of robotics, cranes, excavators, wheel loaders, and space vehicles. The study investigated the dynamics of two arms, with articulated joints and actuated on the joint considering actuation unit dynamics, rigid body dynamics and bending vibrations all together.

Margolis et al. [7] used bond graph method to develop a complete pitch/plane model

of a backhoe considering the boom dynamics, the hydraulic dynamics of the boom cylinder and valve, the chassis/cab mountings and the control stick dynamics. Using the parameters of a medium size back hoe in simulating the bond graph model, the authors demonstrated the instability of the backhoe in consideration. Also Krishnaswamy [6] modeled the boom motion of an excavator to study the passivity of hydraulic systems. Therefore a lot of emphasis has been focused on the boom motion, but in this research work, three excavator motions, i.e, boom, arm, bucket motions were considered.

2.2 Manipulator Dynamics

In order to design, improve performance, simulate the behavior and finally control a system or plant, it is necessary to obtain it's dynamics. To develop the dynamics of a manipulator, a kinematic model of the manipulator is required first. The kinematic modeling is done first by attaching coordinate frames to every link. The usual convention applied to attach frames in the links of a manipulator is the Denavit-Hartenberg procedure [15]. The dynamics of a manipulator can be obtained in various ways namely; using Newton-Euler dynamic formulation, Lagrangian formulation, Kane's method, and others [16, 17].

2.2.1 Newton-Euler Method

The Newton-Euler method is based on Newton's second law of motion, with it's rotational analog called Euler's equation. It describes how forces and moments are related to the accelerations. In the iterative Newton-Euler algorithm, the position, velocity, and acceleration of the joints are calculated using forward recursion, that is, from the base to the end effector. With these as inputs and assuming that the

mass properties of the links and any externally acting forces are known, the joint torques required to cause this motion are calculated using backward recursion, that is, from the end effector towards the base. This algorithm is based on a method published in [18].

2.2.2 Lagrangian Method

The overall Newton-Euler method is based on a force-balance approach to dynamics. On the other hand, Lagrangian formulation is energy-based approach to dynamics. The classical Lagrangian formulation for manipulator dynamics is inefficient, although Lagrangian models seem to be the most prevalent in the literature because they provide the most intuitive insight into the dynamics of the system (energy), but at the expense of computational efficiency [9].

The computational inefficiency of Lagrangian method is due to the use of Lagrangian multipliers. The introduction of Udwadia-Kalaba (UK) formulation [19], has improved the method's numerical efficiency. A fundamental step of the Udwadia-Kalaba formulation is the computation of the Moore-Penrose generalized inverse or pseudoinverse matrix [20].

The efficiency of Newton-Euler method is due to two factors; the recursive structure of the computation, and the representation chosen for the rotational dynamics. Recursive Lagrangian dynamics for rigid manipulators has been discussed previously by Hollerbach [21] and for flexible manipulators by Book [22]. A general algorithm is developed to model the dynamic equation of both rigid and flexible arms [23], but the equation is generally larger than that for rigid links.

2.2.3 Kane's Method

This method arises directly from d'Alembert's principle expressed in Lagrangian form. It is applicable to systems subjected to holonomic and simple nonholonomic constraints. It has the advantages of Newton's mechanics formulation without the corresponding disadvantages. When used without Lagrange multipliers, it automatically eliminates non-working constraint forces, leading to a system of first-order differential equations of minimum dimension. It is also suitable for formulating the linearized equations of motion [24].

2.2.4 Bond Graph Method

The three methods; Newton-Euler, Lagrangian and Kane's methods described, tend to hide the physical interactions between the elements involved [25]. The relatively new bond graph modeling technique, has been proposed to successfully model the dynamics of manipulators and mechanisms. It is a pictorial representation of the dynamics of the system and clearly depicts the interaction between the elements along with their cause and effect relationship. Since bond graph method is based on the interaction of power between elements, it can be used to model multi-energy domains also, for example the actuator system of the manipulator which may be electrical, pneumatic, hydraulic or mechanical.

The concept of bond graphs was originated by Paynter [13]. The idea was further developed by Karnopp and Rosenberg in their textbooks [26–28], such that it could be used in practice. By means of the formulation by Breedveld [29] of a framework based on thermodynamics, bond graph model description evolved to a systems theory. More information about bond graphs can be found in [26–34] from which the

theory was obtained, reviewed and summarized in Appendix A.

For the modeling of mechanical manipulators and mechanisms, the bond graph model can be developed based on kinematic relationships between the time rates of joint variables and the generalized cartesian velocities (translational and angular velocities). It is not necessary to have higher order time rates of variables involved, that is translational and angular accelerations. This is due to the fact that when the kinematic relationships are represented in bond graph form, a dynamic model results since the bonds with the translational velocity also carry the force as the corresponding effort variable, while the bonds with the angular velocity also carry the torque as the effort variable.

The Bond Graph method can be used to obtain more intricate information such as the power required to drive each joint actuator, or the power interaction at the interface with the environment. Such information can also be used to study the stability of the manipulator system during contact interaction with the environment. Modifications and additions to the system can be easily incorporated by connecting suitable bond-graphic sub-systems to its existing bond graph.

2.3 Modeling Soil-tool Interaction in Excavators

An understanding of the soil characteristic properties, the resistance to soil cutting, and the effects of working conditions on the cutting force is required in order to model soil-tool interactions. The soil tool relationships suggest that the specification of an earthmoving process must include not only the magnitudes of the forces involved, but also how such forces are generated, on what parameters they depend, how they are applied to the earth, and how they may be estimated under dynamic conditions.

A larger literature exists on the estimation of resistive forces that act on a tool as it moves through the soil. A group of researchers has attempted to estimate cutting resistance based on empirical results for various types of earthmoving machines [35, 36]. Various indices are suggested based on the configuration of these machines and resistive forces can be roughly estimated by numerically integrating simple equations.

Another body of work, attempts to estimate cutting forces based on first principle mechanics. Motivated largely by the need to estimate the forces experienced by tools used to perform tillage, the ideas in this work come from the civil engineer's load-bearing equations for foundations [37]. These models were extended by several researchers [38, 39] who recognized the similarity to the case of a blade moving through soil. These researchers have added provisions to account for a variety of tool geometries and orientations. The resultant models use parameters of soil-soil friction, soil-tool friction, soil density, tool depth and tool orientation to obtain order of magnitude predictions of the resistive forces developed in the use of agricultural tools. Based on this work, detailed models of the bucket-soil interaction in excavators are covered in [10, 11]. Nguyen [11] developed a model and designed an adaptive observer to observe the disturbance force acting on the excavator due to the bucket-soil interaction. By using the force equilibrium and fundamental earth-moving equation (FEE) in soil mechanics as described in [38], Cannon [10] developed an analytical model to determine the force F exerted by the excavator bucket to the soil, by modifying the FEE for a flat blade moving horizontally as given in [40] to account for the material being retained in the bucket. The author went ahead to come up with an empirical model based on a linear combination of terms found

in the analytical model, and implemented a means of estimating the soil conditions for both model types. The models were found to estimate the resistive forces with good accuracy.

2.4 Summary

The available literature shows that a lot of emphasis on modeling the dynamics of excavators has been focused on the mechanical dynamics of the manipulator, with less attention to the interactive hydraulic and mechanical dynamics. This has been attributed to the computational difficulty and the complication of coupled dynamics which result when models from different modeling techniques one for mechanical and the other for hydraulic dynamics are integrated together for simulation. In this research, models of the hydraulic and mechanical dynamics of an excavator are developed using one modeling technique, that is, bond graphs, hence eliminating the problem of coupling models from different techniques.

The literature also shows that the mechanical dynamics of excavators have been modeled using analytical methods such as Newton-Euler, Lagrangian, Kane's methods, which tend to hide the physical interactions between the elements involved. In this research, bond graph method which clearly depicts the interaction between the elements along with their cause and effect relationships is employed to model the mechanical dynamics of the manipulator.

CHAPTER 3

MODELING THE MANIPULATOR DYNAMICS

3.1 Bond Graph Model Development

A bond graph model representing the mechanical dynamics of the excavating manipulator is developed based on the following assumptions.

- The dynamic model for the excavator is presented in digging mode, that is, the swing angle θ_1 of the first link is held constant such that $\dot{\theta}_1 = 0$, as shown in Figure 3.1. This means that the movement of the excavator mechanism occurs in a vertical plane, that is, the manipulator is considered as a planar mechanism.
- Inertial effects of moving parts, e.g., cylinders and pistons, of the hydraulic actuators are neglected. Masses and mass moments of inertia of the hydraulic actuators are much smaller than those of the boom, arm and bucket. Therefore, they can be reasonably neglected.
- Hydraulic cylinders can transmit axial forces only. There exist no radial force components.
- Passive revolute joints have no friction. The major sources of friction are the stiction and viscous friction between the inner wall and the piston in the hydraulic cylinder assembly. These frictional forces can be treated in the hydraulic system model.
- The base, boom, arm, bucket and the supports are all rigid.

3.1.1 Kinematic Analysis of the Excavator Manipulator

The kinematic analysis of the excavating manipulator is performed to relate the translational velocities of the center of masses of the links (v_{Gi}) to the time rates of the joint variables ($\dot{\theta}_i$), for $i = 2, 3, 4$. The choice of center of mass velocities for rigid bodies leads to a highly systematic approach for constructing bond graphs and is recommended [27]. This is based on the fact that the net force on a rigid body is the rate of change of the momentum which is the mass times the velocity of the center of mass. Also the torque about the center of mass is the rate of change of angular momentum which is given by the inertia tensor times the angular velocity vector at the center of mass.

Firstly a global coordinate system as shown in Figure 3.1 is defined to describe the position of the bucket tip. A fixed right-hand cartesian coordinate system $O(x_0y_0z_0)$ is chosen, and its origin is attached anywhere in the base. The local coordinate systems $A(x_1y_1z_1)$, $C(x_2y_2z_2)$, $D(x_3y_3z_3)$ and $N(x_4y_4z_4)$ are then assigned systematically by applying Denavit-Hartenberg procedure as described in [41], and noting that the Z_{i-1} axis lies along the axis of rotation of the i^{th} joint.

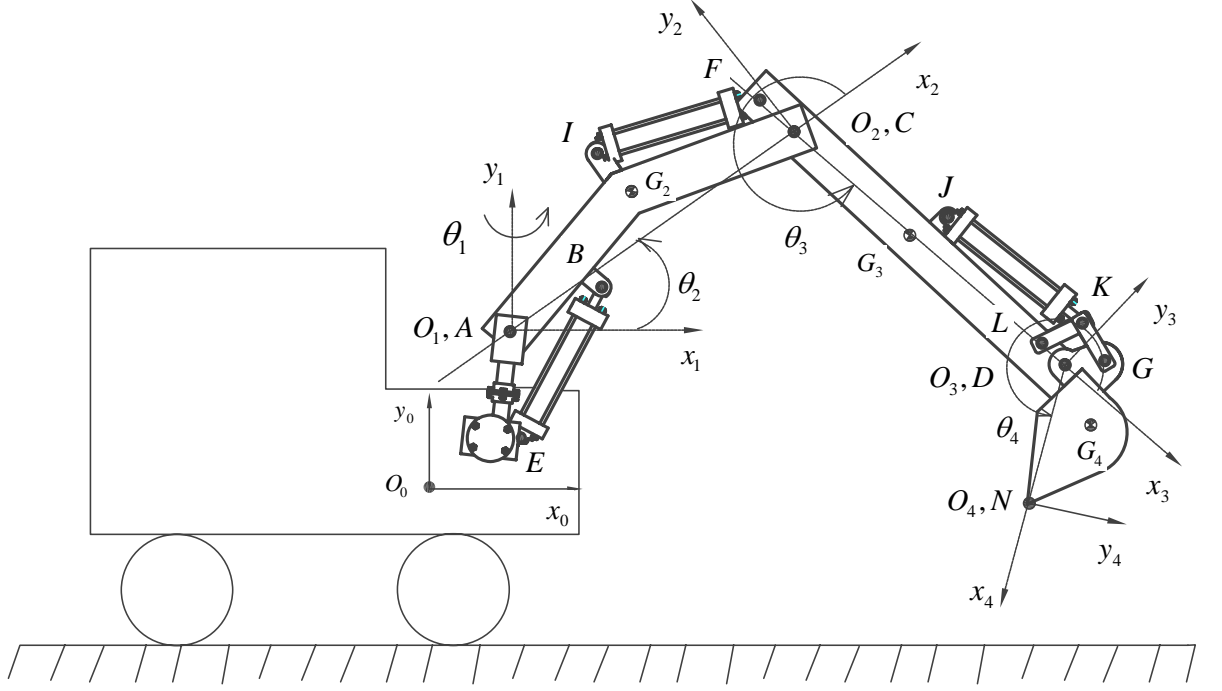


Figure 3.1: Coordinate System assignment for excavator

The homogeneous transformation matrix that relate two adjacent (i^{th} and $(i-1)^{th}$) reference frames can be written in the general form as described in [16, 17];

$$A_{i-1}^{(i)} = \begin{pmatrix} \cos \theta_i & -\cos \alpha_i \sin \theta_i & \sin \alpha_i \sin \theta_i & a_i \cos \theta_i \\ \sin \theta_i & \cos \alpha_i \cos \theta_i & -\sin \alpha_i \cos \theta_i & a_i \sin \theta_i \\ 0 & \sin \alpha_i & \cos \alpha_i & d_i \\ 0 & 0 & 0 & 1 \end{pmatrix} \quad (3.1)$$

Where d_i , a_i , α_i and θ_i are the structural kinematic parameters for the links $i = 1, 2, 3, 4$ defined as;

- θ_i is the joint angle from the X_{i-1} axis to the X_i axis about the Z_{i-1} axis.
- d_i is the distance from the origin of the $(i-1)^{th}$ coordinate frame to the intersection of the Z_{i-1} axis with the X_i axis along the Z_{i-1} axis.

- a_i is the offset distance from the intersection of the Z_{i-1} axis with the X_i axis to the origin of the i^{th} frame along the X^i axis.
- α_i is the offset angle from the Z_{i-1} axis to the Z_i axis about the X_i axis.

For a rotary joint, d_i , a_i , and α_i are the joint parameters and remain constant for a manipulator, while θ_i is the joint variable that changes when link i rotates. Therefore, in this research, joint variables refer to θ_i .

Table 3.1 shows the structural kinematic parameters of the excavating manipulator which when substituted into Equation 3.1 leads to the homogeneous transformation matrices for the arm as given in Equations 3.2 to 3.5.

Table 3.1: Structural kinematic parameters

Link joint i	α_i	a_i	d_i	θ_i
1	0	$a_1 = l_1$	0	θ_1
2	0	$a_2 = l_2$	0	θ_2
3	0	$a_3 = l_3$	0	θ_3
4	0	$a_4 = l_4$	0	θ_4

$$A_0^{(1)} = \begin{pmatrix} \cos \theta_1 & -\sin \theta_1 & 0 & a_1 \cos \theta_1 \\ \sin \theta_1 & \cos \theta_1 & 0 & a_1 \sin \theta_1 \\ 0 & 0 & 1 & 0 \\ 0 & 0 & 0 & 1 \end{pmatrix} \quad (3.2)$$

$$A_1^{(2)} = \begin{pmatrix} \cos \theta_2 & -\sin \theta_2 & 0 & a_2 \cos \theta_2 \\ \sin \theta_2 & \cos \theta_2 & 0 & a_2 \sin \theta_2 \\ 0 & 0 & 1 & 0 \\ 0 & 0 & 0 & 1 \end{pmatrix} \quad (3.3)$$

$$A_2^{(3)} = \begin{pmatrix} \cos \theta_3 & -\sin \theta_3 & 0 & a_3 \cos \theta_3 \\ \sin \theta_3 & \cos \theta_3 & 0 & a_3 \sin \theta_3 \\ 0 & 0 & 1 & 0 \\ 0 & 0 & 0 & 1 \end{pmatrix} \quad (3.4)$$

$$A_3^{(4)} = \begin{pmatrix} \cos \theta_4 & -\sin \theta_4 & 0 & a_4 \cos \theta_4 \\ \sin \theta_4 & \cos \theta_4 & 0 & a_4 \sin \theta_4 \\ 0 & 0 & 1 & 0 \\ 0 & 0 & 0 & 1 \end{pmatrix} \quad (3.5)$$

The dynamic model for the excavator is presented in digging mode, i.e., the swing angle θ_1 of the first link is held constant at zero (0^0) such that $\dot{\theta}_1 = 0$. Therefore the transformation matrix given in Equation 3.2 becomes;

$$A_0^{(1)} = \begin{pmatrix} 1 & 0 & 0 & a_1 \\ 0 & 1 & 0 & 0 \\ 0 & 0 & 1 & 0 \\ 0 & 0 & 0 & 1 \end{pmatrix} \quad (3.6)$$

It follows that the movements of the excavator mechanism during digging occur in a vertical plane.

3.1.2 Forward Recursive Equations

Luh et al. [18] proposed recursive way of determining equations of motion of links by referencing all the velocities, accelerations, forces, etc, to their own link coordinate system. In forward recursion, two rotation matrices obtained from the upper left 3×3 sub-matrix of the transformation matrix in Equation 3.1 and its inverse are normally applied to transform a vector with reference to coordinate frame $(X_i, Y_i, Z_i,)$ to the coordinate system $(X_{i-1}, Y_{i-1}, Z_{i-1},)$. These rotation matrices are given in Equations 3.7 and 3.8 below;

$$R_{i-1}^{(i)} = \begin{pmatrix} \cos \theta_i & -\cos \alpha_i \sin \theta_i & \sin \alpha_i \sin \theta_i \\ \sin \theta_i & \cos \alpha_i \cos \theta_i & -\sin \alpha_i \cos \theta_i \\ 0 & \sin \alpha_i & \cos \alpha_i \end{pmatrix} \quad (3.7)$$

and

$$[R_i^{(i-1)}] = [R_{i-1}^{(i)}]^{-1} = \begin{pmatrix} \cos \theta_i & \sin \theta_i & 0 \\ -\cos \alpha_i \sin \theta_i & \cos \alpha_i \cos \theta_i & \sin \alpha_i \\ \sin \alpha_i \sin \theta_i & -\sin \alpha_i \cos \theta_i & \cos \alpha_i \end{pmatrix} \quad (3.8)$$

3.1.2.1 Angular Velocity

The rotational velocity of link i as specified in the i^{th} coordinate frame, is described in recursive form as;

$$\omega_i^{(i)} = R_i^{(i-1)} \omega_{i-1}^{(i-1)} + \dot{Z}_0 \dot{q}_i \quad (3.9)$$

where

$$\dot{Z}_0 = \begin{pmatrix} 0 \\ 0 \\ 1 \end{pmatrix}$$

$\dot{q}_i = \dot{\theta}_i$ for revolute joints.

3.1.2.2 Translational Velocity of the Origin of Link Coordinate Frame

The translation velocity v_{0i}^i of the origin of the i^{th} link coordinate frame as specified in the i^{th} coordinate frame is given recursively as;

$$v_{0i}^{(i)} = R_i^{(i-1)} v_{0i-1}^{(i-1)} + \omega_i^{(i)} \times (P_{0i}^{(i)} - P_{0i-1}^{(i)}) \quad (3.10)$$

where

$P_{0i-1}^{(i)}$ is the vector from the origin of the base coordinate system to the origin of the $(i-1)^{th}$ coordinate system as expressed in the i^{th} coordinate system.

$P_{0i}^{(i)}$ is the vector from the origin of the base coordinate system to the origin of the i^{th} coordinate system as expressed in the i^{th} coordinate system.

$v_{0i-1}^{(i-1)}$ is the translation velocity of the origin of the $(i-1)^{th}$ link coordinate frame as expressed in the $(i-1)^{th}$ coordinate frame.

3.1.2.3 Translational Velocity of the Center of Mass of a Link

The translational velocity v_{Gi}^i of the center of mass of the i^{th} link as specified in the i^{th} coordinate frame is given recursively by;

$$v_{Gi}^{(i)} = v_{0i}^{(i)} + \omega_i^{(i)} \times (P_{Gi}^{(i)} - P_{0i}^{(i)}) \quad (3.11)$$

Where

$P_{Gi}^{(i)}$ is the vector from the origin of the base coordinate system to the center of mass of the i^{th} frame as expressed in the i^{th} coordinate system.

$P_{0i}^{(i)}$ is the vector from the origin of the base coordinate system to the origin of the i^{th} coordinate system as expressed in the i^{th} coordinate system.

Then applying the recursive Equations 3.9, 3.10, and 3.11 to the excavator links $i = 2, 3, 4$, the translational velocities of the links center of masses expressed in the respective frame can be developed. The last step is to determine the centroid velocities of the links with respect to the non moving base frame. This is done by rotating $v_{G_i}^i$ with the rotation matrix R_0^i which is given as;

$$R_0^{(i)} = R_0^{(1)} R_1^{(2)} \dots R_{i-1}^{(i)} \quad (3.12)$$

3.1.2.4 Applying the Recursive Equations to the Boom Link $i = 2$

Consider Figure 3.2.

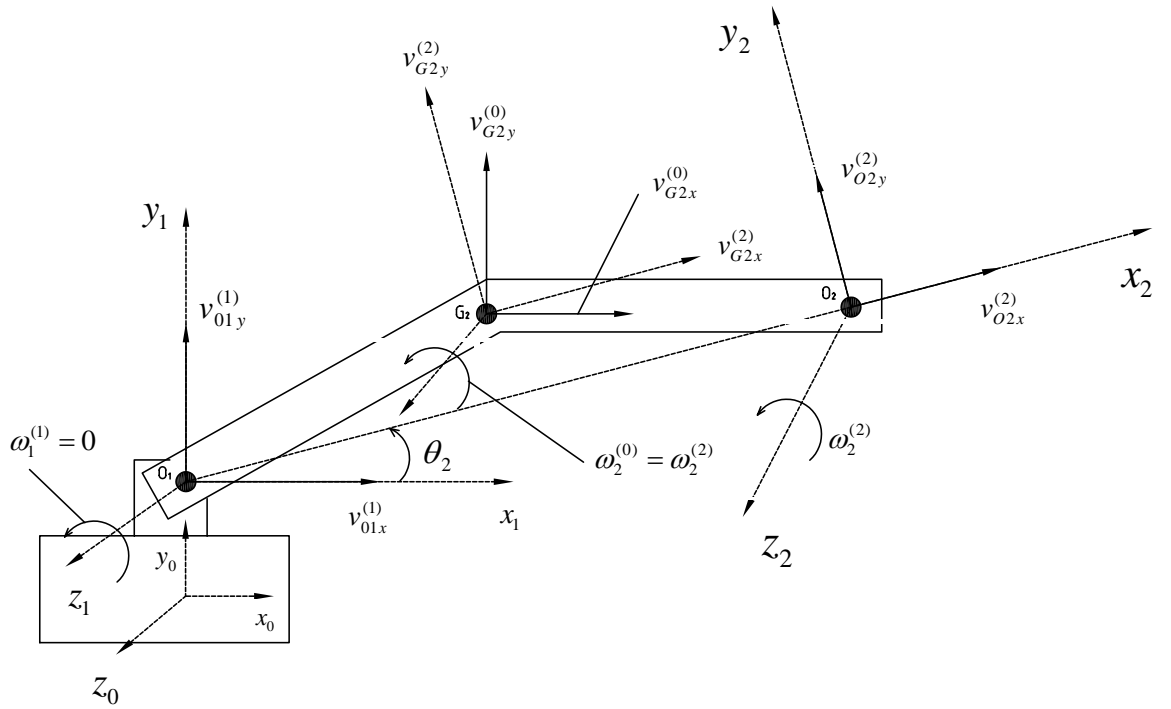


Figure 3.2: Kinematic analysis for the boom link

Since the base is taken to be stationary then $\omega_1^{(1)} = 0$ and $v_1^{(1)} = 0$. Therefore;

$$\begin{aligned}
\omega_2^{(2)} &= R_2^{(1)}\omega_1^{(1)} + \dot{Z}_0\dot{\theta}_2 \\
&= \begin{pmatrix} \cos\theta_2 & \sin\theta_2 & 0 \\ -\sin\theta_2 & \cos\theta_2 & 0 \\ 0 & 0 & 1 \end{pmatrix} \begin{pmatrix} 0 \\ 0 \\ 0 \end{pmatrix} + \begin{pmatrix} 0 \\ 0 \\ 1 \end{pmatrix} \dot{\theta}_2 \\
\omega_2^{(2)} &= \omega_2^{(0)} = \begin{pmatrix} 0 \\ 0 \\ \dot{\theta}_2 \end{pmatrix}
\end{aligned} \tag{3.13}$$

$$\begin{aligned}
v_{02}^{(2)} &= R_2^{(1)}v_{01}^{(1)} + \omega_2^{(2)} \times (P_{02}^{(2)} - P_{01}^{(2)}) \\
&= R_2^{(1)}v_{01}^{(1)} + \omega_2^{(2)} \times \bar{L}_{O_1O_2} \\
&= \begin{pmatrix} \cos\theta_2 & \sin\theta_2 & 0 \\ -\sin\theta_2 & \cos\theta_2 & 0 \\ 0 & 0 & 1 \end{pmatrix} \begin{pmatrix} 0 \\ 0 \\ 0 \end{pmatrix} + \begin{pmatrix} 0 \\ 0 \\ \dot{\theta}_2 \end{pmatrix} \times \begin{pmatrix} L_{O_1O_2} \\ 0 \\ 0 \end{pmatrix} \\
v_{02}^{(2)} &= \begin{pmatrix} 0 \\ L_{O_1O_2}\dot{\theta}_2 \\ 0 \end{pmatrix}
\end{aligned} \tag{3.14}$$

To determine the $v_{G_2}^{(2)}$, let $\angle G_2O_2O_1 = \sigma_1$ where G_2 is the position of the center of mass of link 2. Therefore,

$$\begin{aligned}
v_{G_2}^{(2)} &= v_{O_2}^{(2)} + \omega_2^{(2)} \times (P_{G_2}^{(2)} - P_{O_2}^{(2)}) \\
&= \begin{pmatrix} 0 \\ L_{O_1O_2}\dot{\theta}_2 \\ 0 \end{pmatrix} + \begin{pmatrix} 0 \\ 0 \\ \dot{\theta}_2 \end{pmatrix} \times \begin{pmatrix} -L_{G_2O_2} \cos \sigma_1 \\ L_{G_2O_2} \sin \sigma_1 \\ 0 \end{pmatrix} \\
&= \begin{pmatrix} 0 \\ L_{O_1O_2}\dot{\theta}_2 \\ 0 \end{pmatrix} + \begin{pmatrix} -L_{G_2O_2}\dot{\theta}_2 \sin \sigma_1 \\ -L_{G_2O_2}\dot{\theta}_2 \cos \sigma_1 \\ 0 \end{pmatrix} \\
v_{G_2}^{(2)} &= \begin{pmatrix} -L_{G_2O_2}\dot{\theta}_2 \sin \sigma_1 \\ -L_{G_2O_2}\dot{\theta}_2 \cos \sigma_1 + L_{O_1O_2}\dot{\theta}_2 \\ 0 \end{pmatrix} \tag{3.15}
\end{aligned}$$

To determine the translational velocity of the center of mass of the boom link as referenced to the base frame, $v_{G_2}^{(2)}$ is multiplied with a rotational matrix obtained from Equation 3.12 and given by;

$$\begin{aligned}
R_0^{(2)} &= R_0^{(1)} R_1^{(2)} \\
&= \begin{pmatrix} 1 & 0 & 0 \\ 0 & 1 & 0 \\ 0 & 0 & 1 \end{pmatrix} \begin{pmatrix} \cos \theta_2 & -\sin \theta_2 & 0 \\ \sin \theta_2 & \cos \theta_2 & 0 \\ 0 & 0 & 1 \end{pmatrix} \\
&= \begin{pmatrix} \cos \theta_2 & -\sin \theta_2 & 0 \\ \sin \theta_2 & \cos \theta_2 & 0 \\ 0 & 0 & 1 \end{pmatrix} \tag{3.16}
\end{aligned}$$

Therefore $v_{G_2}^{(0)}$ is obtained as;

$$\begin{aligned}
v_{G_2}^{(0)} &= \begin{pmatrix} \cos \theta_2 & -\sin \theta_2 & 0 \\ \sin \theta_2 & \cos \theta_2 & 0 \\ 0 & 0 & 1 \end{pmatrix} \begin{pmatrix} -L_{G_2O_2} \dot{\theta}_2 \sin \sigma_1 \\ -L_{G_2O_2} \dot{\theta}_2 \cos \sigma_1 + L_{O_1O_2} \dot{\theta}_2 \\ 0 \end{pmatrix} \\
&= \begin{pmatrix} -L_{G_2O_2} \dot{\theta}_2 \cos \theta_2 \sin \sigma_1 + L_{G_2O_2} \dot{\theta}_2 \sin \theta_2 \cos \sigma_1 - L_{O_1O_2} \dot{\theta}_2 \sin \theta_2 \\ -L_{G_2O_2} \dot{\theta}_2 \sin \theta_2 \sin \sigma_1 - L_{G_2O_2} \dot{\theta}_2 \cos \theta_2 \cos \sigma_1 + L_{O_1O_2} \dot{\theta}_2 \cos \theta_2 \\ 0 \end{pmatrix} \\
&= \begin{pmatrix} L_{G_2O_2} \dot{\theta}_2 \sin(\theta_2 - \sigma_1) - L_{O_1O_2} \dot{\theta}_2 \sin \theta_2 \\ -L_{G_2O_2} \dot{\theta}_2 \cos(\theta_2 - \sigma_1) + L_{O_1O_2} \dot{\theta}_2 \cos \theta_2 \\ 0 \end{pmatrix} \tag{3.17}
\end{aligned}$$

From which the horizontal and vertical velocity components of the boom's center of mass with respect to the base coordinate frame are obtained respectively as;

$$\begin{aligned}
v_{G_2x} &= \left[L_{G_2O_2} \sin(\theta_2 - \sigma_1) - L_{O_1O_2} \sin \theta_2 \right] \dot{\theta}_2 \\
&= r_1 \dot{\theta}_2 \tag{3.18}
\end{aligned}$$

$$\begin{aligned}
v_{G_2y} &= \left[-L_{G_2O_2} \cos(\theta_2 - \sigma_1) + L_{O_1O_2} \cos \theta_2 \right] \dot{\theta}_2 \\
&= r_2 \dot{\theta}_2 \tag{3.19}
\end{aligned}$$

Using Equations 3.18 and 3.19, a bond graph model of the boom link can be represented as shown in Figure 3.3.

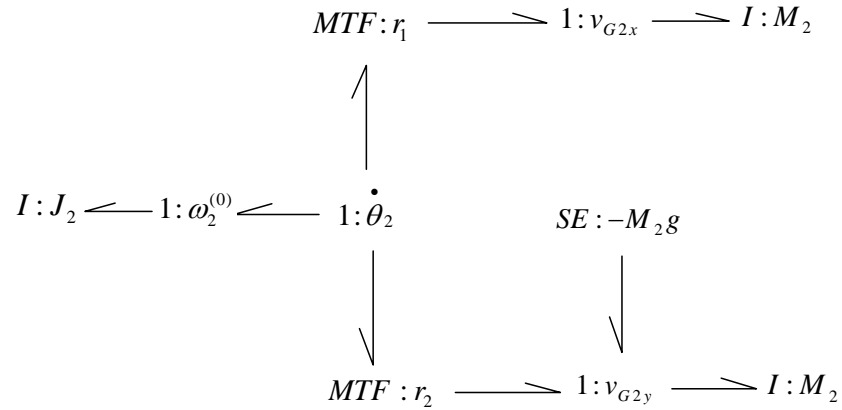


Figure 3.3: Bond graph representation of the boom's mechanical dynamics

where

M_2 is the mass of link 2 (boom),

$$r_1 = L_{G_2O_2} \sin(\theta_2 - \sigma_1) - L_{O_1O_2} \sin \theta_2,$$

$$r_2 = -L_{G_2O_2} \cos(\theta_2 - \sigma_1) + L_{O_1O_2} \cos \theta_2 \text{ and}$$

J_2 is the mass inertia of link 2 (boom) about the center of mass.

3.1.2.5 Applying the Recursive Equations to the Arm Link $i = 3$

Consider Figure 3.4.

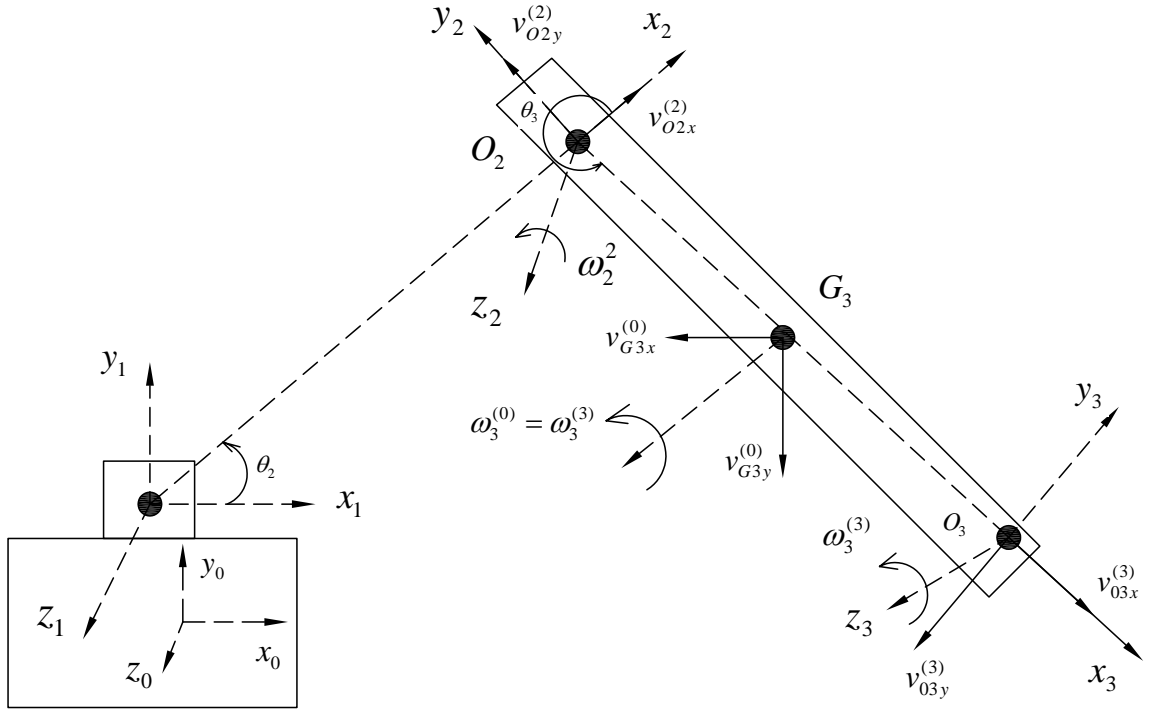


Figure 3.4: Kinematic analysis for the arm link

$$\begin{aligned}
 \omega_3^{(3)} &= R_3^{(2)} \omega_2^{(2)} + \dot{Z}_0 \dot{\theta}_3 \\
 &= \begin{pmatrix} \cos \theta_3 & \sin \theta_3 & 0 \\ -\sin \theta_3 & \cos \theta_3 & 0 \\ 0 & 0 & 1 \end{pmatrix} \begin{pmatrix} 0 \\ 0 \\ \dot{\theta}_2 \end{pmatrix} + \begin{pmatrix} 0 \\ 0 \\ 1 \end{pmatrix} \dot{\theta}_3 \\
 \omega_3^{(3)} &= \omega_3^{(0)} = \begin{pmatrix} 0 \\ 0 \\ \dot{\theta}_2 + \dot{\theta}_3 \end{pmatrix} \tag{3.20}
 \end{aligned}$$

$$\begin{aligned}
v_{03}^{(3)} &= R_3^{(2)} v_{02}^{(2)} + \omega_3^{(3)} \times (P_{03}^{(3)} - P_{02}^{(3)}) \\
&= R_3^{(2)} v_{02}^{(2)} + \omega_3^{(3)} \times \bar{L}_{O_2O_3} \\
&= \begin{pmatrix} \cos \theta_3 & \sin \theta_3 & 0 \\ -\sin \theta_3 & \cos \theta_3 & 0 \\ 0 & 0 & 1 \end{pmatrix} \begin{pmatrix} 0 \\ L_{O_1O_2} \dot{\theta}_2 \\ 0 \end{pmatrix} + \begin{pmatrix} 0 \\ 0 \\ \dot{\theta}_2 + \dot{\theta}_3 \end{pmatrix} \times \begin{pmatrix} L_{O_2O_3} \\ 0 \\ 0 \end{pmatrix} \\
&= \begin{pmatrix} L_{O_1O_2} \dot{\theta}_2 \sin \theta_3 \\ L_{O_1O_2} \dot{\theta}_2 \cos \theta_3 \\ 0 \end{pmatrix} + \begin{pmatrix} 0 \\ L_{O_2O_3} (\dot{\theta}_2 + \dot{\theta}_3) \\ 0 \end{pmatrix} \\
v_{03}^{(3)} &= \begin{pmatrix} L_{O_1O_2} \dot{\theta}_2 \sin \theta_3 \\ L_{O_1O_2} \dot{\theta}_2 \cos \theta_3 + L_{O_2O_3} (\dot{\theta}_2 + \dot{\theta}_3) \\ 0 \end{pmatrix} \tag{3.21}
\end{aligned}$$

To determine the $v_{G_3}^{(3)}$, let $\angle G_3O_3O_2 = \sigma_2$ where G_3 is the position of the center of mass of link 3. Therefore,

$$\begin{aligned}
v_{G3}^{(3)} &= v_{03}^{(3)} + \omega_3^{(3)} \times (P_{G3}^{(3)} - P_{03}^{(3)}) \\
&= \begin{pmatrix} L_{O_1O_2} \dot{\theta}_2 \sin \theta_3 \\ L_{O_1O_2} \dot{\theta}_2 \cos \theta_3 + L_{O_2O_3} (\dot{\theta}_2 + \dot{\theta}_3) \\ 0 \end{pmatrix} + \begin{pmatrix} 0 \\ 0 \\ \dot{\theta}_2 + \dot{\theta}_3 \end{pmatrix} \times \begin{pmatrix} -L_{G_3O_3} \cos \sigma_2 \\ L_{G_3O_3} \sin \sigma_2 \\ 0 \end{pmatrix} \\
&= \begin{pmatrix} L_{O_1O_2} \dot{\theta}_2 \sin \theta_3 \\ L_{O_1O_2} \dot{\theta}_2 \cos \theta_3 + L_{O_2O_3} (\dot{\theta}_2 + \dot{\theta}_3) \\ 0 \end{pmatrix} + \begin{pmatrix} -L_{G_3O_3} (\dot{\theta}_2 + \dot{\theta}_3) \sin \sigma_2 \\ -L_{G_3O_3} (\dot{\theta}_2 + \dot{\theta}_3) \cos \sigma_2 \\ 0 \end{pmatrix} \\
v_{G3}^{(3)} &= \begin{pmatrix} L_{O_1O_2} \dot{\theta}_2 \sin \theta_3 - L_{G_3O_3} (\dot{\theta}_2 + \dot{\theta}_3) \sin \sigma_2 \\ L_{O_1O_2} \dot{\theta}_2 \cos \theta_3 + L_{O_2O_3} (\dot{\theta}_2 + \dot{\theta}_3) - L_{G_3O_3} (\dot{\theta}_2 + \dot{\theta}_3) \cos \sigma_2 \\ 0 \end{pmatrix} \quad (3.22)
\end{aligned}$$

To determine the translational velocity of the center of mass of the arm link as referenced to the base frame, $v_{G3}^{(3)}$ is multiplied with a rotational matrix obtained from Equation 3.12 and given by;

$$\begin{aligned}
R_0^{(3)} &= R_0^{(1)} R_1^{(2)} R_2^{(3)} \\
&= \begin{pmatrix} 1 & 0 & 0 \\ 0 & 1 & 0 \\ 0 & 0 & 1 \end{pmatrix} \begin{pmatrix} \cos \theta_2 & -\sin \theta_2 & 0 \\ \sin \theta_2 & \cos \theta_2 & 0 \\ 0 & 0 & 1 \end{pmatrix} \begin{pmatrix} \cos \theta_3 & -\sin \theta_3 & 0 \\ \sin \theta_3 & \cos \theta_3 & 0 \\ 0 & 0 & 1 \end{pmatrix} \\
&= \begin{pmatrix} \cos(\theta_2 + \theta_3) & -\sin(\theta_2 + \theta_3) & 0 \\ \sin(\theta_2 + \theta_3) & \cos(\theta_2 + \theta_3) & 0 \\ 0 & 0 & 1 \end{pmatrix} \quad (3.23)
\end{aligned}$$

Let,

$$S_2 = \sin \theta_2,$$

$$S_3 = \sin \theta_3,$$

$$C_2 = \cos \theta_2,$$

$$C_3 = \cos \theta_3,$$

$$S_{23} = \sin(\theta_2 + \theta_3) \text{ and}$$

$$C_{23} = \cos(\theta_2 + \theta_3).$$

$v_{G_3}^{(0)}$ is obtained as;

$$\begin{aligned} v_{G_3}^{(0)} &= \begin{pmatrix} C_{23} & -S_{23} & 0 \\ S_{23} & C_{23} & 0 \\ 0 & 0 & 1 \end{pmatrix} \begin{pmatrix} L_{O_1O_2}\dot{\theta}_2S_3 - L_{G_3O_3}(\dot{\theta}_2 + \dot{\theta}_3) \sin \sigma_2 \\ L_{O_1O_2}\dot{\theta}_2C_3 + L_{O_2O_3}(\dot{\theta}_2 + \dot{\theta}_3) - L_{G_3O_3}(\dot{\theta}_2 + \dot{\theta}_3) \cos \sigma_2 \\ 0 \end{pmatrix} \\ &= \begin{pmatrix} -L_{O_1O_2}\dot{\theta}_2S_2 + L_{G_3O_3}(\dot{\theta}_2 + \dot{\theta}_3) \sin(\theta_2 + \theta_3 - \sigma_2) - L_{O_2O_3}(\dot{\theta}_2 + \dot{\theta}_3)S_{23} \\ L_{O_1O_2}\dot{\theta}_2C_2 - L_{G_3O_3}(\dot{\theta}_2 + \dot{\theta}_3) \cos(\theta_2 + \theta_3 - \sigma_2) + L_{O_2O_3}(\dot{\theta}_2 + \dot{\theta}_3)C_{23} \\ 0 \end{pmatrix} \end{aligned} \quad (3.24)$$

From which the horizontal and vertical velocity components are given as;

$$\begin{aligned} v_{G_{3x}} &= \left[-L_{O_1O_2} \sin \theta_2 + L_{G_3O_3} \sin(\theta_2 + \theta_3 - \sigma_2) - L_{O_2O_3} \sin(\theta_2 + \theta_3) \right] \dot{\theta}_2 \\ &\quad + \left[L_{G_3O_3} \sin(\theta_2 + \theta_3 - \sigma_2) - L_{O_2O_3} \sin(\theta_2 + \theta_3) \right] \dot{\theta}_3 \\ &= r_3\dot{\theta}_2 + r_4\dot{\theta}_3 \end{aligned} \quad (3.25)$$

$$\begin{aligned} v_{G_{3y}} &= \left[L_{O_1O_2} \cos \theta_2 - L_{G_3O_3} \cos(\theta_2 + \theta_3 - \sigma_2) + L_{O_2O_3} \cos(\theta_2 + \theta_3) \right] \dot{\theta}_2 \\ &\quad + \left[-L_{G_3O_3} \cos(\theta_2 + \theta_3 - \sigma_2) + L_{O_2O_3} \cos(\theta_2 + \theta_3) \right] \dot{\theta}_3 \\ &= r_5\dot{\theta}_2 + r_6\dot{\theta}_3 \end{aligned} \quad (3.26)$$

Using Equations 3.25 and 3.26, a bond graph model of the arm link can be represented as shown in Figure 3.5.

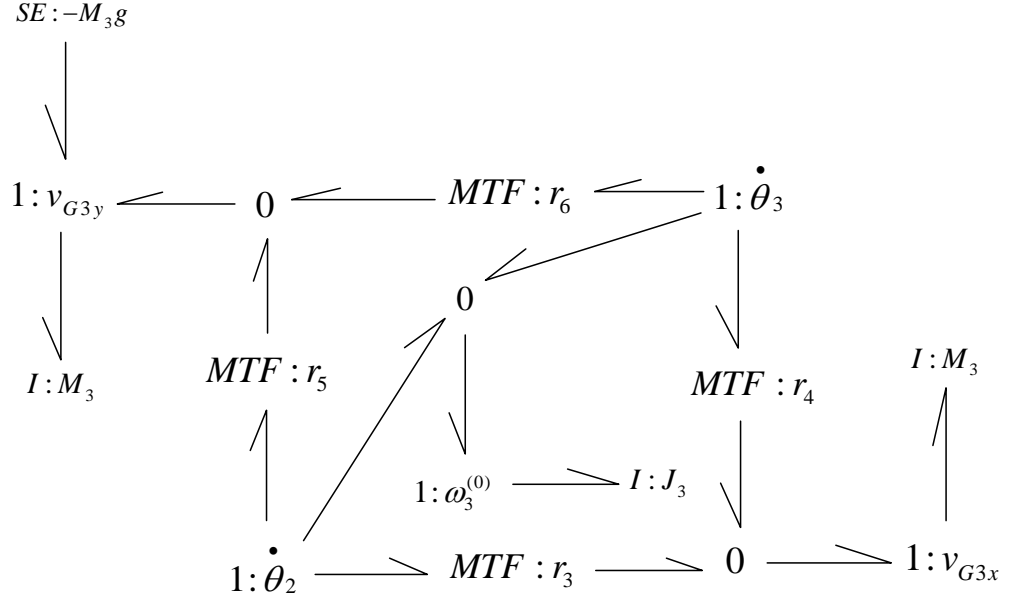


Figure 3.5: Bond graph representation of the arms's mechanical dynamics

where

M_3 is the mass of link 3 (arm),

$$r_3 = -L_{O_1O_2} \sin \theta_2 + L_{G_3O_3} \sin(\theta_2 + \theta_3 - \sigma_2) - L_{O_2O_3} \sin(\theta_2 + \theta_3),$$

$$r_4 = -L_{G_3O_3} \sin(\theta_2 + \theta_3 - \sigma_2) + L_{O_2O_3} \sin(\theta_2 + \theta_3),$$

$$r_5 = L_{O_1O_2} \cos \theta_2 - L_{G_3O_3} \cos(\theta_2 + \theta_3 - \sigma_2) + L_{O_2O_3} \cos(\theta_2 + \theta_3),$$

$$r_6 = -L_{G_3O_3} \cos(\theta_2 + \theta_3 - \sigma_2) + L_{O_2O_3} \cos(\theta_2 + \theta_3 \text{ and}$$

J_3 is the mass inertia of link 3 (arm) about the center of mass.

3.1.2.6 Applying the Recursive Equations to the Bucket Link $i = 4$

Consider Figure 3.6.

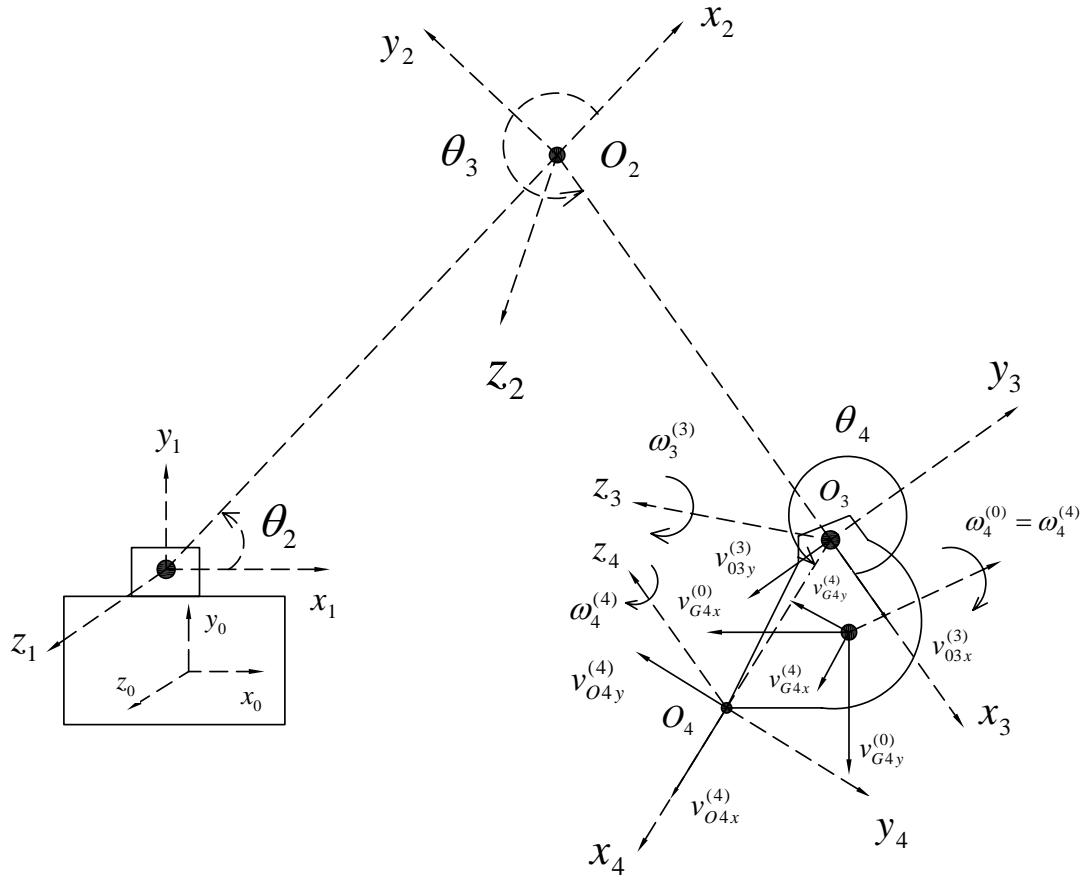


Figure 3.6: Kinematic analysis for the bucket link

$$\begin{aligned}
\omega_4^{(4)} &= R_4^{(3)}\omega_3^{(3)} + \dot{Z}_0\dot{\theta}_4 \\
&= \begin{pmatrix} \cos\theta_4 & \sin\theta_4 & 0 \\ -\sin\theta_4 & \cos\theta_4 & 0 \\ 0 & 0 & 1 \end{pmatrix} \begin{pmatrix} 0 \\ 0 \\ \dot{\theta}_2 + \dot{\theta}_3 \end{pmatrix} + \begin{pmatrix} 0 \\ 0 \\ 1 \end{pmatrix} \dot{\theta}_4 \\
\omega_4^{(4)} &= \omega_4^{(0)} = \begin{pmatrix} 0 \\ 0 \\ \dot{\theta}_2 + \dot{\theta}_3 + \dot{\theta}_4 \end{pmatrix} \tag{3.27}
\end{aligned}$$

$$\begin{aligned}
v_{04}^{(4)} &= R_4^{(3)}v_{03}^{(3)} + \omega_4^{(4)} \times (P_{04}^{(4)} - P_{03}^{(4)}) \\
&= R_4^{(3)}v_{03}^{(3)} + \omega_4^{(4)} \times (\bar{L}_{O_0O_4} - \bar{L}_{O_0O_3}) \\
&= R_4^{(3)}v_{03}^{(3)} + \omega_4^{(4)} \times \bar{L}_{O_3O_4} \\
&= \begin{pmatrix} \cos\theta_4 & \sin\theta_4 & 0 \\ -\sin\theta_4 & \cos\theta_4 & 0 \\ 0 & 0 & 1 \end{pmatrix} \begin{pmatrix} L_{O_1O_2}\dot{\theta}_2 \sin\theta_3 \\ L_{O_1O_2}\dot{\theta}_2 \cos\theta_3 + L_{O_2O_3}(\dot{\theta}_2 + \dot{\theta}_3) \\ 0 \end{pmatrix} + \begin{pmatrix} 0 \\ 0 \\ \dot{\theta}_2 + \dot{\theta}_3 + \dot{\theta}_4 \end{pmatrix} \\
&\quad \times \begin{pmatrix} L_{O_3O_4} \\ 0 \\ 0 \end{pmatrix} \\
&= \begin{pmatrix} L_{O_1O_2}\dot{\theta}_2 \sin(\theta_3 + \theta_4) + L_{O_2O_3}(\dot{\theta}_2 + \dot{\theta}_3) \sin\theta_4 \\ L_{O_1O_2}\dot{\theta}_2 \cos(\theta_3 + \theta_4) + L_{O_2O_3}(\dot{\theta}_2 + \dot{\theta}_3) \cos\theta_4 \\ 0 \end{pmatrix} + \begin{pmatrix} 0 \\ L_{O_3O_4}(\dot{\theta}_2 + \dot{\theta}_3 + \dot{\theta}_4) \\ 0 \end{pmatrix} \\
v_{04}^{(4)} &= \begin{pmatrix} L_{O_1O_2}\dot{\theta}_2 \sin(\theta_3 + \theta_4) + L_{O_2O_3}(\dot{\theta}_2 + \dot{\theta}_3) \sin\theta_4 \\ L_{O_1O_2}\dot{\theta}_2 \cos(\theta_3 + \theta_4) + L_{O_2O_3}(\dot{\theta}_2 + \dot{\theta}_3) \cos\theta_4 + L_{O_3O_4}(\dot{\theta}_2 + \dot{\theta}_3 + \dot{\theta}_4) \\ 0 \end{pmatrix} \tag{3.28}
\end{aligned}$$

To determine the $v_{G_4}^{(4)}$, let $\angle G_4 O_4 O_3 = \sigma_3$ where G_4 is the position of the center of mass of link 4. Therefore,

$$\begin{aligned}
v_{G_4}^{(4)} &= v_{O_4}^{(4)} + \omega_4^{(4)} \times (P_{G_4}^{(4)} - P_{O_3}^{(4)}) \\
&= \begin{pmatrix} L_{O_1 O_2} \dot{\theta}_2 S_{34} + L_{O_2 O_3} \dot{\varphi}_{23} \sin \theta_4 \\ L_{O_1 O_2} \dot{\theta}_2 C_{34} + L_{O_2 O_3} \dot{\varphi}_{23} \cos \theta_4 + L_{O_3 O_4} \dot{\varphi}_{234} \\ 0 \end{pmatrix} \\
&\quad + \begin{pmatrix} 0 \\ 0 \\ \dot{\theta}_2 + \dot{\theta}_3 + \dot{\theta}_4 \end{pmatrix} \times \begin{pmatrix} -L_{G_4 O_4} \cos \sigma_3 \\ L_{G_4 O_4} \sin \sigma_3 \\ 0 \end{pmatrix} \\
&= \begin{pmatrix} L_{O_1 O_2} \dot{\theta}_2 S_{34} + L_{O_2 O_3} \dot{\varphi}_{23} \sin \theta_4 \\ L_{O_1 O_2} \dot{\theta}_2 S_{34} + L_{O_2 O_3} \dot{\varphi}_{23} \cos \theta_4 + L_{O_3 O_4} \dot{\varphi}_{234} \\ 0 \end{pmatrix} + \begin{pmatrix} -L_{G_4 O_4} \dot{\varphi}_{234} \sin \sigma_3 \\ -L_{G_4 O_4} \dot{\varphi}_{234} \cos \sigma_3 \\ 0 \end{pmatrix} \\
v_{G_4}^{(4)} &= \begin{pmatrix} L_{O_1 O_2} \dot{\theta}_2 S_{34} + L_{O_2 O_3} \dot{\varphi}_{23} S_4 - L_{G_4 O_4} \dot{\varphi}_{234} \sin \sigma_3 \\ L_{O_1 O_2} \dot{\theta}_2 C_{34} + L_{O_2 O_3} \dot{\varphi}_{23} C_4 + L_{O_3 O_4} \dot{\varphi}_{234} - L_{G_4 O_4} \dot{\varphi}_{234} \cos \sigma_3 \\ 0 \end{pmatrix} \quad (3.29)
\end{aligned}$$

To determine the translational velocity of the center of mass of the bucket link as referenced to the base frame, $v_{G_4}^{(4)}$ is multiplied with a rotational matrix obtained

from Equation 3.12 and given by;

$$\begin{aligned}
R_0^{(4)} &= R_0^{(1)} R_1^{(2)} R_2^{(3)} R_3^{(4)} \\
&= \begin{pmatrix} 1 & 0 & 0 \\ 0 & 1 & 0 \\ 0 & 0 & 1 \end{pmatrix} \begin{pmatrix} \cos \theta_2 & -\sin \theta_2 & 0 \\ \sin \theta_2 & \cos \theta_2 & 0 \\ 0 & 0 & 1 \end{pmatrix} \begin{pmatrix} \cos \theta_3 & -\sin \theta_3 & 0 \\ \sin \theta_3 & \cos \theta_3 & 0 \\ 0 & 0 & 1 \end{pmatrix} \begin{pmatrix} \cos \theta_4 & -\sin \theta_4 & 0 \\ \sin \theta_4 & \cos \theta_4 & 0 \\ 0 & 0 & 1 \end{pmatrix} \\
&= \begin{pmatrix} \cos(\theta_2 + \theta_3 + \theta_4) & -\sin(\theta_2 + \theta_3 + \theta_4) & 0 \\ \sin(\theta_2 + \theta_3 + \theta_4) & \cos(\theta_2 + \theta_3 + \theta_4) & 0 \\ 0 & 0 & 1 \end{pmatrix} \tag{3.30}
\end{aligned}$$

$v_{G4}^{(0)}$ is obtained as;

$$\begin{aligned}
v_{G4}^{(0)} &= \begin{pmatrix} C_{234} & -S_{234} & 0 \\ S_{234} & C_{234} & 0 \\ 0 & 0 & 1 \end{pmatrix} \begin{pmatrix} L_{O_1O_2} \dot{\theta}_2 S_{34} + L_{O_2O_3} \dot{\varphi}_{23} S_4 - L_{G_4O_4} \dot{\varphi}_{234} \sin \sigma_3 \\ L_{O_1O_2} \dot{\theta}_2 C_{34} + L_{O_2O_3} \dot{\varphi}_{23} C_4 + L_{O_3O_4} \dot{\varphi}_{234} - L_{G_4O_4} \dot{\varphi}_{234} \cos \sigma_3 \\ 0 \end{pmatrix} \\
&= \begin{pmatrix} -L_{O_1O_2} S_2 \dot{\theta}_2 - L_{O_2O_3} S_{23} \dot{\varphi}_{23} - L_{O_3O_4} S_{234} \dot{\varphi}_{234} + L_{G_4O_4} S_{234\sigma_3} \dot{\varphi}_{234} \\ L_{O_1O_2} C_2 \dot{\theta}_2 - L_{O_2O_3} C_{23} \dot{\varphi}_{23} - L_{O_3O_4} C_{234} \dot{\varphi}_{234} - L_{G_4O_4} C_{234\sigma_3} \dot{\varphi}_{234} \\ 0 \end{pmatrix} \tag{3.31}
\end{aligned}$$

where

$$\dot{\varphi}_{23} = \dot{\theta}_2 + \dot{\theta}_3,$$

$$\dot{\varphi}_{234} = \dot{\theta}_2 + \dot{\theta}_3 + \dot{\theta}_4,$$

$$S_{234\sigma_3} = \sin(\theta_2 + \theta_3 + \theta_4 - \sigma_3),$$

$$C_{234\sigma_3} = \cos(\theta_2 + \theta_3 + \theta_4 - \sigma_3),$$

$$S_{234} = \sin(\theta_2 + \theta_3 + \theta_4) \text{ and}$$

$$C_{234} = \cos(\theta_2 + \theta_3 + \theta_4).$$

From which the horizontal and vertical velocity components are given as;

$$\begin{aligned} v_{G_4x} &= \left[-L_{O_1O_2} \sin \theta_2 - L_{O_2O_3} \sin(\theta_2 + \theta_3) - L_{O_3O_4} \sin(\theta_2 + \theta_3 + \theta_4) \right. \\ &\quad \left. + L_{G_4O_4} \sin(\theta_2 + \theta_3 + \theta_4 - \sigma_3) \right] \dot{\theta}_2 + \left[-L_{O_2O_3} \sin(\theta_2 + \theta_3) \right. \\ &\quad \left. - L_{O_3O_4} \sin(\theta_2 + \theta_3 + \theta_4) + L_{G_4O_4} \sin(\theta_2 + \theta_3 + \theta_4 - \sigma_3) \right] \dot{\theta}_3 + \\ &\quad \left[-L_{O_3O_4} \sin(\theta_2 + \theta_3 + \theta_4) + L_{G_4O_4} \sin(\theta_2 + \theta_3 + \theta_4 - \sigma_3) \right] \dot{\theta}_4 \\ &= r_7 \dot{\theta}_2 + r_8 \dot{\theta}_3 + r_9 \dot{\theta}_4 \end{aligned} \quad (3.32)$$

$$\begin{aligned} v_{G_4y} &= \left[L_{O_1O_2} \cos \theta_2 + L_{O_2O_3} \cos(\theta_2 + \theta_3) + L_{O_3O_4} \cos(\theta_2 + \theta_3 + \theta_4) \right. \\ &\quad \left. - L_{G_4O_4} \cos(\theta_2 + \theta_3 + \theta_4 - \sigma_3) \right] \dot{\theta}_2 + \left[L_{O_2O_3} \cos(\theta_2 + \theta_3) \right. \\ &\quad \left. + L_{O_3O_4} \cos(\theta_2 + \theta_3 + \theta_4) - L_{G_4O_4} \cos(\theta_2 + \theta_3 + \theta_4 - \sigma_3) \right] \dot{\theta}_3 + \\ &\quad \left[L_{O_3O_4} \cos(\theta_2 + \theta_3 + \theta_4) - L_{G_4O_4} \cos(\theta_2 + \theta_3 + \theta_4 - \sigma_3) \right] \dot{\theta}_4 \\ &= r_{10} \dot{\theta}_2 + r_{11} \dot{\theta}_3 + r_{12} \dot{\theta}_4 \end{aligned} \quad (3.33)$$

Using Equations 3.32 and 3.33, a bond graph model of the bucket link can be represented as shown in Figure 3.7.

where

M_4 is the mass of link 4 (bucket),

$$r_7 = -L_{O_1O_2} \sin \theta_2 - L_{O_2O_3} \sin(\theta_2 + \theta_3) - L_{O_3O_4} \sin(\theta_2 + \theta_3 + \theta_4) + L_{G_4O_4} \sin(\theta_2 + \theta_3 + \theta_4 - \sigma_3),$$

$$r_8 = -L_{O_2O_3} \sin(\theta_2 + \theta_3) - L_{O_3O_4} \sin(\theta_2 + \theta_3 + \theta_4) + L_{G_4O_4} \sin(\theta_2 + \theta_3 + \theta_4 - \sigma_3),$$

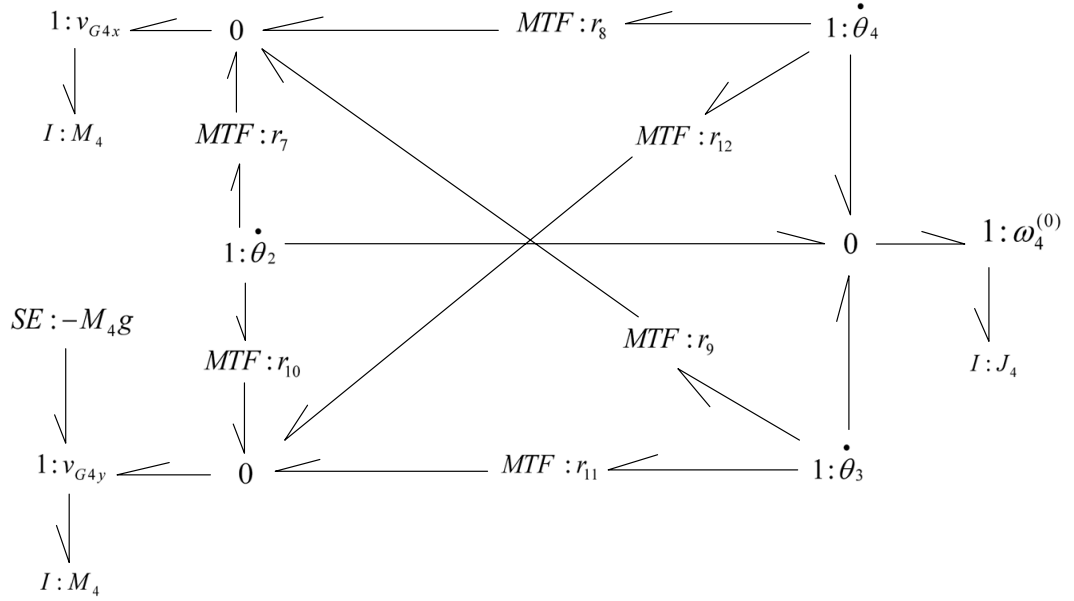


Figure 3.7: Bond graph representation of the buckets' mechanical dynamics

$$r_9 = -L_{O_3O_4} \sin(\theta_2 + \theta_3 + \theta_4) + L_{G_4O_4} \sin(\theta_2 + \theta_3 + \theta_4 - \sigma_3),$$

$$r_{10} = L_{O_1O_2} \cos \theta_2 + L_{O_2O_3} \cos(\theta_2 + \theta_3) + L_{O_3O_4} \cos(\theta_2 + \theta_3 + \theta_4) - L_{G_4O_4} \cos(\theta_2 + \theta_3 + \theta_4 - \sigma_3),$$

$$r_{11} = L_{O_2O_3} \cos(\theta_2 + \theta_3) + L_{O_3O_4} \cos(\theta_2 + \theta_3 + \theta_4) - L_{G_4O_4} \cos(\theta_2 + \theta_3 + \theta_4 - \sigma_3),$$

$$r_{12} = L_{O_3O_4} \cos(\theta_2 + \theta_3 + \theta_4) - L_{G_4O_4} \cos(\theta_2 + \theta_3 + \theta_4 - \sigma_3) \text{ and}$$

J_4 is the mass inertia of link 4 (bucket) about the center of mass.

3.1.3 Modeling the Bucket Digging Force

A model that accounts for the material being retained in the bucket, which was developed by Cannon [10] using force equilibrium and fundamental earthmoving Equation in soil mechanics was applied in this study to determine the force F exerted by the excavator bucket to the soil. Force F exerted by the excavator bucket to the

soil can be obtained from Figure 3.8 as shown in Equation 3.34.

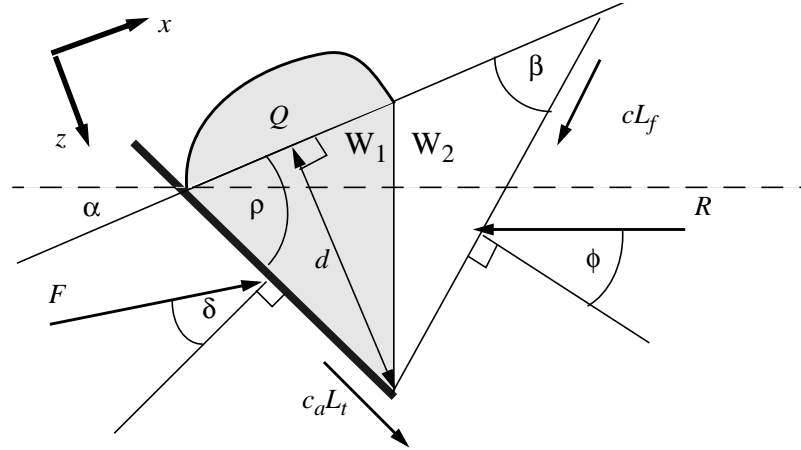


Figure 3.8: Wedge model that accounts for the material being retained in the bucket

$$F = d^2 w \gamma g N_w + c w d N_c + V_s \gamma g N_q \quad (3.34)$$

The material in the shaded region corresponds to the swept volume V_s , Q is the surcharge, W_1 is the weight of the material above the bucket, W_2 is the weight of the rest of material in the wedge, L_t is the length of the tool, L_f is the length of the failure surface, R is the force of the soil resisting the moving of the wedge, F is the force exerted by the tool on the wedge, c_a is the adhesion between the soil and the blade, c is the cohesiveness of the soil media, β is the failure surface angle, also called the slip angle, α is the surface terrain slope, also called the cutting angle, ϕ is the soil-soil friction angle, ρ is the rake angle of the tool relative to the soil surface, σ is the soil-tool friction angle, d is the depth of the bucket tool perpendicular to the soil surface, w is the width of the bucket, γ is the bulk density of the soil media and g is the gravitational acceleration.

N_w , N_c N_q are N-factors which depend on: the soil's frictional strength, the bucket

tool geometry and soil-to-tool strength properties, and are given by the Equations 3.35, 3.36 and 3.37 respectively.

$$N_w = \frac{(\cot \beta - \tan \alpha) (\cos \alpha + \sin \alpha \cot(\beta + \phi))}{2(\cos(\rho + \sigma) + \sin(\rho + \sigma) \cot(\beta + \phi))} \quad (3.35)$$

$$N_c = \frac{1 + \cot \beta \cot(\beta + \phi)}{\cos(\rho + \sigma) + \sin(\rho + \sigma) \cot(\beta + \phi)} \quad (3.36)$$

$$N_q = \frac{\cos \alpha + \sin \alpha \cot(\beta + \phi)}{\cos(\rho + \sigma) + \sin(\rho + \sigma) \cot(\beta + \phi)} \quad (3.37)$$

Equations 3.34 to 3.37 show that the magnitude of the digging force depends on many factors such as the cutting angle, specific resistance to cutting, volume of the bucket, amount of the the material ripped into the bucket and the volume of the material surcharged. These factors are always varying during the bucket digging operation and indicate complicated interactions of the bucket and the soil, hence making modeling of the bucket digging force throughout the digging process a complex and bulk process.

In this study, a simplified model is presented by considering the situation of critical force, and then assuming the force to remain constant throughout the digging process. The critical value of the cutting angle is given by [11],

$$\alpha_c = \frac{1}{2} \left(\pi - \sigma - \sin^{-1}(\sin \sigma \sin \rho) \right) \quad (3.38)$$

For noncohesive soils such as sandy-loam, the angle of friction between the steel blade with soil (σ) is 20° , the rake angle of the tool relative to the soil surface (ρ) is 45° and the soil-soil friction angle (ϕ) is 23° [11]. Therefore using Equation 3.38 the critical cutting angle (α_c) was found to be 73° .

Since the soil frictional properties alone determine the failure zones in soil cutting, the most likely slip angle β is that which causes N_w in Equation 3.35 to be minimum. In effect, this identifies path of least resistance for the soil to fail. When different values of β (between 0° and 90° degrees) are tried, N_w varies and the most likely value of β is found at the minimum value of N_w , and is then used to calculate the other terms [42]. Therefore a curve of N_w factor versus the β is plotted to determine the appropriate value of β and N_w , as shown in Figure 3.9. From the curve $\beta = 38^\circ$ and $N_w = 0.6875$.

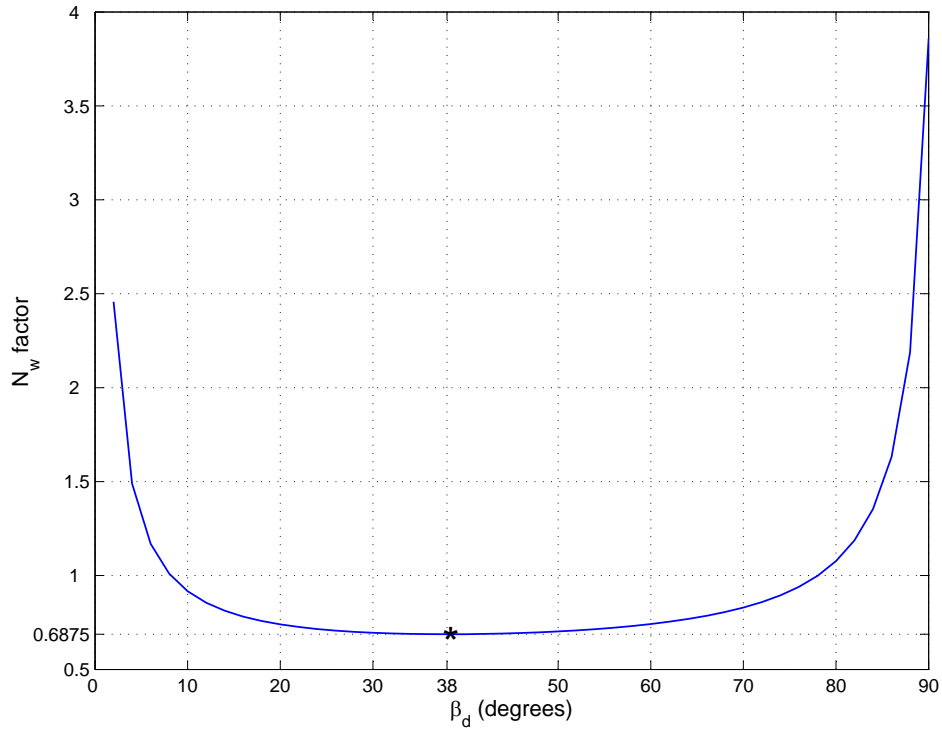


Figure 3.9: The variation of N_w factor with the slip angle β_d

The other factors can therefore be calculated from Equations 3.36 and 3.37 as $N_c = 1.8481$ and $N_q = 0.8860$. Using Equation 3.34 and noting that; the width of the bucket (w) is $274mm$, the depth (d) of the bucket tool perpendicular to the soil

surface at the critical instant is 212.13mm , the cohesiveness (c) and the bulk density (γ) of the sandy-loam soil media are 20kPa and 1200kg/m^3 [11] respectively, we get the critical force applied to the soil by the bucket to be $F = 4.5\text{kN}$.

The soil-tool force F is assumed to be applied at the cutting edge of the bucket. From the Newton's third law of motion, the soil applies an opposite and equal reaction force at the bucket, which can be resolved to a normal and tangential force components as shown in Figure 3.10

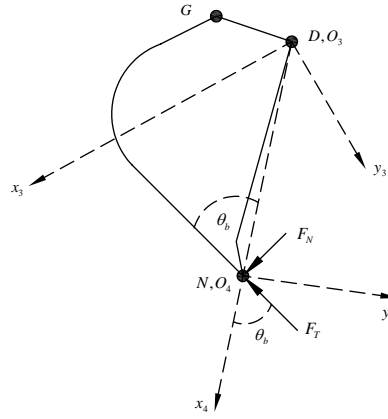


Figure 3.10: Bucket digging force at the tip

F_T and F_N are the tangential and normal reaction forces at the bucket tip as given in Equations 3.39 and 3.40 respectively.

$$F_T = F \sin \sigma \quad (3.39)$$

$$F_N = F \cos \sigma \quad (3.40)$$

Resolving the normal and tangential forces about the fourth local coordinate system

$(x_4y_4z_4)$ we get;

$$F_{b4}^{(4)} = \begin{pmatrix} -F_T \cos \theta_b + F_N \sin \theta_b \\ -F_T \sin \theta_b - F_N \cos \theta_b \\ 0 \end{pmatrix} \quad (3.41)$$

The bucket force should be referenced to the base coordinate frame by multiplying Equation 3.41 by the rotation matrix in Equation 3.30 to get;

$$F_{b4}^{(0)} = \begin{pmatrix} -(F_T \cos \theta_b - F_N \sin \theta_b)C_{234} + (F_T \sin \theta_b + F_N \cos \theta_b)S_{234} \\ -(F_T \cos \theta_b - F_N \sin \theta_b)S_{234} - (F_T \sin \theta_b + F_N \cos \theta_b)C_{234} \\ 0 \end{pmatrix} \quad (3.42)$$

From which, the horizontal and vertical components of the bucket reaction force are given as;

$$F_x = -(F_T \cos \theta_b - F_N \sin \theta_b) \cos(\theta_2 + \theta_3 + \theta_4) + (F_T \sin \theta_b + F_N \cos \theta_b) \sin(\theta_2 + \theta_3 + \theta_4) \quad (3.43)$$

$$F_y = -(F_T \cos \theta_b - F_N \sin \theta_b) \sin(\theta_2 + \theta_3 + \theta_4) - (F_T \sin \theta_b + F_N \cos \theta_b) \cos(\theta_2 + \theta_3 + \theta_4) \quad (3.44)$$

These forces are included at the translational velocity of the origin of the 4th link coordinate frame given by Equation 3.28, but referenced to the base coordinate

frame, that is;

$$\begin{aligned}
v_{O_4}^{(0)} &= R_0^{(4)} v_{04}^{(4)} \\
&= \begin{pmatrix} C_{234} & -S_{234} & 0 \\ S_{234} & C_{234} & 0 \\ 0 & 0 & 1 \end{pmatrix} \begin{pmatrix} L_{O_1O_2} \dot{\theta}_2 S_{34} + L_{O_2O_3} \dot{\varphi}_{23} S_4 \\ L_{O_1O_2} \dot{\theta}_2 C_{34} + L_{O_2O_3} \dot{\varphi}_{23} C_4 + L_{O_3O_4} \dot{\varphi}_{234} \\ 0 \end{pmatrix} \\
&= \begin{pmatrix} -L_{O_1O_2} S_2 \dot{\theta}_2 - L_{O_2O_3} S_{23} \dot{\varphi}_{23} - L_{O_3O_4} S_{234} \dot{\varphi}_{234} \\ L_{O_1O_2} C_2 \dot{\theta}_2 + L_{O_2O_3} C_{23} \dot{\varphi}_{23} + L_{O_3O_4} C_{234} \dot{\varphi}_{234} \\ 0 \end{pmatrix} \quad (3.45)
\end{aligned}$$

From which the horizontal and vertical velocity components are given as;

$$\begin{aligned}
v_{O_{4x}} &= \left[-L_{O_1O_2} \sin \theta_2 - L_{O_2O_3} \sin(\theta_2 + \theta_3) - L_{O_3O_4} \sin(\theta_2 + \theta_3 + \theta_4) \right] \dot{\theta}_2 + \\
&\quad \left[-L_{O_2O_3} \sin(\theta_2 + \theta_3) - L_{O_3O_4} \sin(\theta_2 + \theta_3 + \theta_4) \right] \dot{\theta}_3 + \left[-L_{O_3O_4} \sin(\theta_2 + \theta_3 + \theta_4) \right] \dot{\theta}_4 \\
&= r_{13} \dot{\theta}_2 + r_{14} \dot{\theta}_3 + r_{15} \dot{\theta}_4 \quad (3.46)
\end{aligned}$$

and

$$\begin{aligned}
v_{O_{4y}} &= \left[L_{O_1O_2} \cos \theta_2 + L_{O_2O_3} \cos(\theta_2 + \theta_3) + L_{O_3O_4} \cos(\theta_2 + \theta_3 + \theta_4) \right] \dot{\theta}_2 + \\
&\quad \left[L_{O_2O_3} \cos(\theta_2 + \theta_3) + L_{O_3O_4} \cos(\theta_2 + \theta_3 + \theta_4) \right] \dot{\theta}_3 + \left[L_{O_3O_4} \cos(\theta_2 + \theta_3 + \theta_4) \right] \dot{\theta}_4 \\
&= r_{16} \dot{\theta}_2 + r_{17} \dot{\theta}_3 + r_{18} \dot{\theta}_4 \quad (3.47)
\end{aligned}$$

Using Equations 3.46 and 3.47, a bond graph model representing the soil-bucket interaction can be represented as shown in Figure 3.11.

where

F_x and F_y are the horizontal and vertical components of the bucket digging force as given in Equations 3.43 and 3.44 respectively,

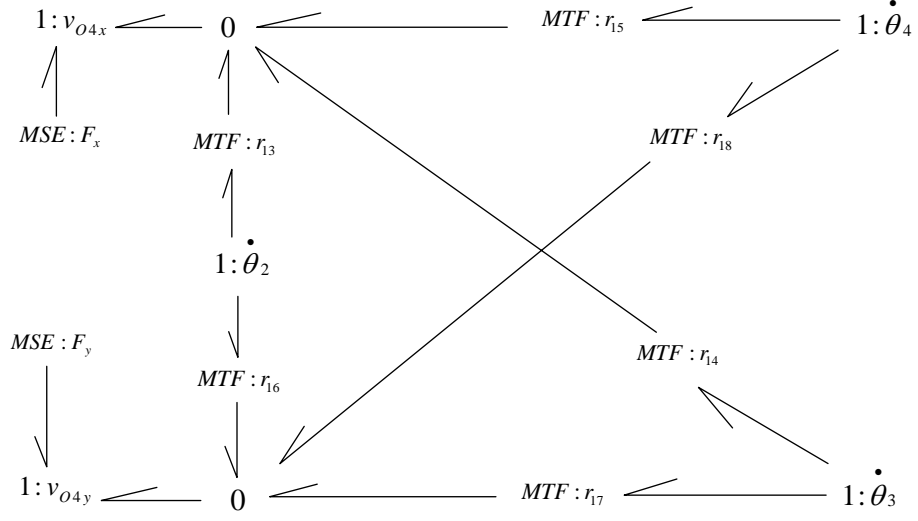


Figure 3.11: Bond graph representation of velocity of the buckets's tip

$$r_{13} = -L_{O_1O_2} \sin \theta_2 - L_{O_2O_3} \sin(\theta_2 + \theta_3) - L_{O_3O_4} \sin(\theta_2 + \theta_3 + \theta_4),$$

$$r_{14} = -L_{O_2O_3} \sin(\theta_2 + \theta_3) - L_{O_3O_4} \sin(\theta_2 + \theta_3 + \theta_4),$$

$$r_{15} = -L_{O_3O_4} \sin(\theta_2 + \theta_3 + \theta_4)$$

$$r_{16} = L_{O_1O_2} \cos \theta_2 + L_{O_2O_3} \cos(\theta_2 + \theta_3) + L_{O_3O_4} \cos(\theta_2 + \theta_3 + \theta_4),$$

$$r_{17} = L_{O_2O_3} \cos(\theta_2 + \theta_3) + L_{O_3O_4} \cos(\theta_2 + \theta_3 + \theta_4) \text{ and}$$

$$r_{18} = L_{O_3O_4} \cos(\theta_2 + \theta_3 + \theta_4).$$

3.1.4 A Non Causal Bond Graph Model of the Manipulator's Dynamics

Figure 3.12 shows the overall non causal bond graph model of the excavating manipulator obtained by combining all sub models of the links and the soil-tool interaction already developed.

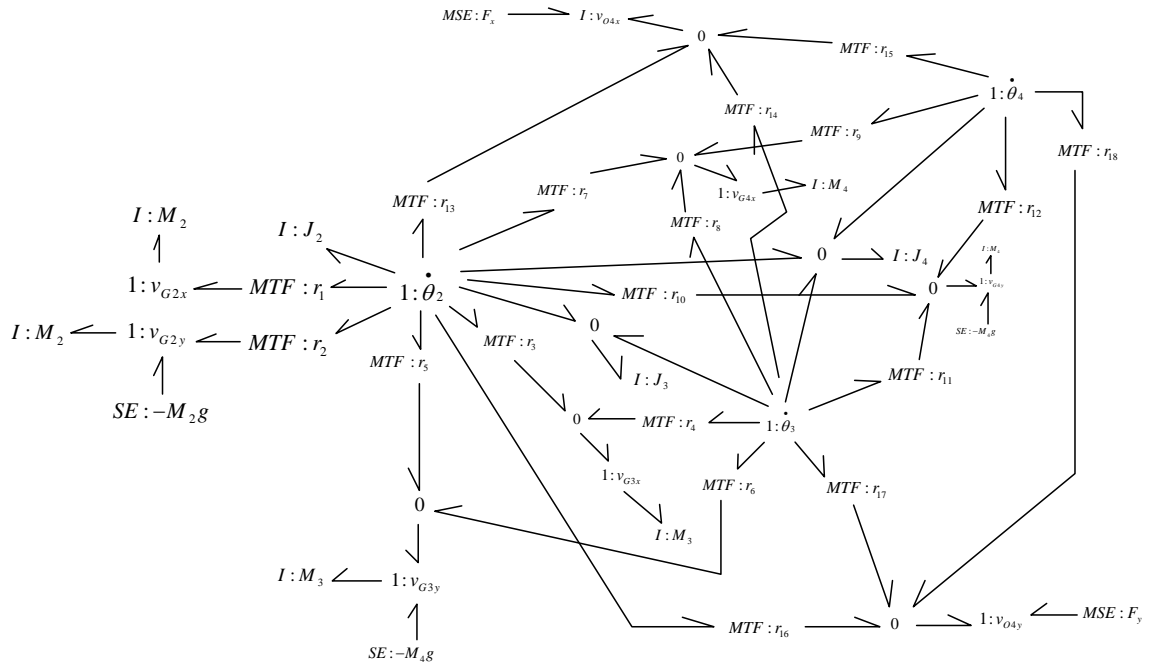


Figure 3.12: A non causal bond graph model representing the mechanical dynamics of the manipulator

No causality is assigned to the bond graph and such a bond graph is referred to as non causal bond graph.

3.2 Checking the Model

One way to check the bond graph model developed as shown in Figure 3.12, is to compare results with those available in the literature. A two link manipulator shown in Figure 3.13, moving in a free space, and whose links are uniform and of equal lengths was considered. Such a problem is studied using Newton-Euler, Lagrangian, and d'Alembert's methods in the standard robotic textbooks [16, 17].

All the rotation axes at the joints are along the z -axis normal to the paper surface.

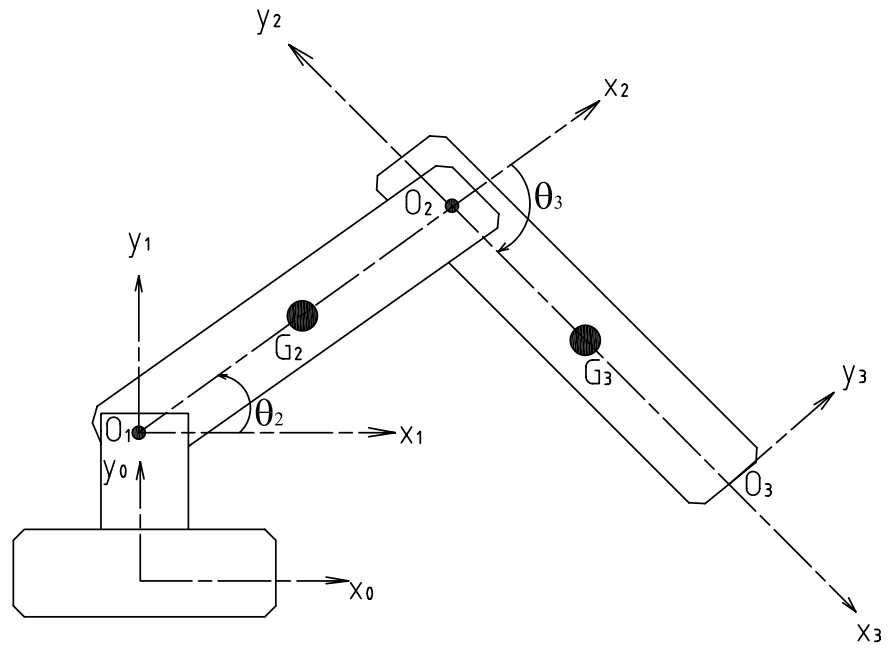


Figure 3.13: A two link planar manipulator

Let;

$$L_{O_1O_2} = L_{O_2O_3} = l,$$

$$L_{G_2O_2} = L_{G_3O_3} = \frac{l}{2},$$

$$\sigma_1 = \sigma_2 = 0.$$

Substituting these values in the equations for the mass center translational velocities given by Equations 3.18, 3.19, 3.25, and 3.26, leads to,

$$v_{G2_x} = \left(-\frac{l}{2} \sin \theta_2\right) \dot{\theta}_2 = r_1 \dot{\theta}_2 \quad (3.48)$$

$$v_{G2_y} = \left(\frac{l}{2} \cos \theta_2\right) \dot{\theta}_2 = r_2 \dot{\theta}_2 \quad (3.49)$$

$$\begin{aligned} v_{G3_x} &= \left[-l \sin \theta_2 - \frac{l}{2} \sin(\theta_2 + \theta_3)\right] \dot{\theta}_2 + \left[-\frac{l}{2} \sin(\theta_2 + \theta_3)\right] \dot{\theta}_3 \\ &= r_3 \dot{\theta}_2 + r_4 \dot{\theta}_3 \end{aligned} \quad (3.50)$$

$$\begin{aligned} v_{G3_y} &= \left[l \cos \theta_2 + \frac{l}{2} \cos(\theta_2 + \theta_3)\right] \dot{\theta}_2 + \left[\frac{l}{2} \cos(\theta_2 + \theta_3)\right] \dot{\theta}_3 \\ &= r_5 \dot{\theta}_2 + r_6 \dot{\theta}_3 \end{aligned} \quad (3.51)$$

The translational velocity of the origin of third local coordinate frame referenced about the base coordinate frame is given as;

$$\begin{aligned} v_{O3}^0 &= R_0^3 v_{O3}^3 \\ &= \begin{pmatrix} \cos(\theta_2 + \sin \theta_3) & -\sin(\theta_2 + \sin \theta_3) & 0 \\ \sin(\theta_2 + \sin \theta_3) & \cos(\theta_2 + \sin \theta_3) & 0 \\ 0 & 0 & 1 \end{pmatrix} \begin{pmatrix} l \dot{\theta}_2 \sin \theta_3 \\ l \dot{\theta}_2 \cos \theta_3 + l(\dot{\theta}_2 + \dot{\theta}_3) \\ 0 \end{pmatrix} \\ &= \begin{pmatrix} -l \dot{\theta}_2 \sin \theta_2 - l(\dot{\theta}_2 + \dot{\theta}_3) \sin(\theta_2 + \sin \theta_3) \\ l \dot{\theta}_2 \cos \theta_2 + l(\dot{\theta}_2 + \dot{\theta}_3) \cos(\theta_2 + \sin \theta_3) \\ 0 \end{pmatrix} \end{aligned} \quad (3.52)$$

From which the horizontal and vertical components can be obtained to be;

$$\begin{aligned} v_{O3_x} &= \left[-l \sin \theta_2 - l \sin(\theta_2 + \theta_3)\right] \dot{\theta}_2 + \left[-l \sin(\theta_2 + \theta_3)\right] \dot{\theta}_3 \\ &= r_7 \dot{\theta}_2 + r_8 \dot{\theta}_3 \end{aligned} \quad (3.53)$$

$$\begin{aligned} v_{O3_y} &= \left[l \cos \theta_2 + l \cos(\theta_2 + \theta_3)\right] \dot{\theta}_2 + \left[l \cos(\theta_2 + \theta_3)\right] \dot{\theta}_3 \\ &= r_9 \dot{\theta}_2 + r_{10} \dot{\theta}_3 \end{aligned} \quad (3.54)$$

A bond graph model for the two link manipulator is represented as shown in Figure 3.14.

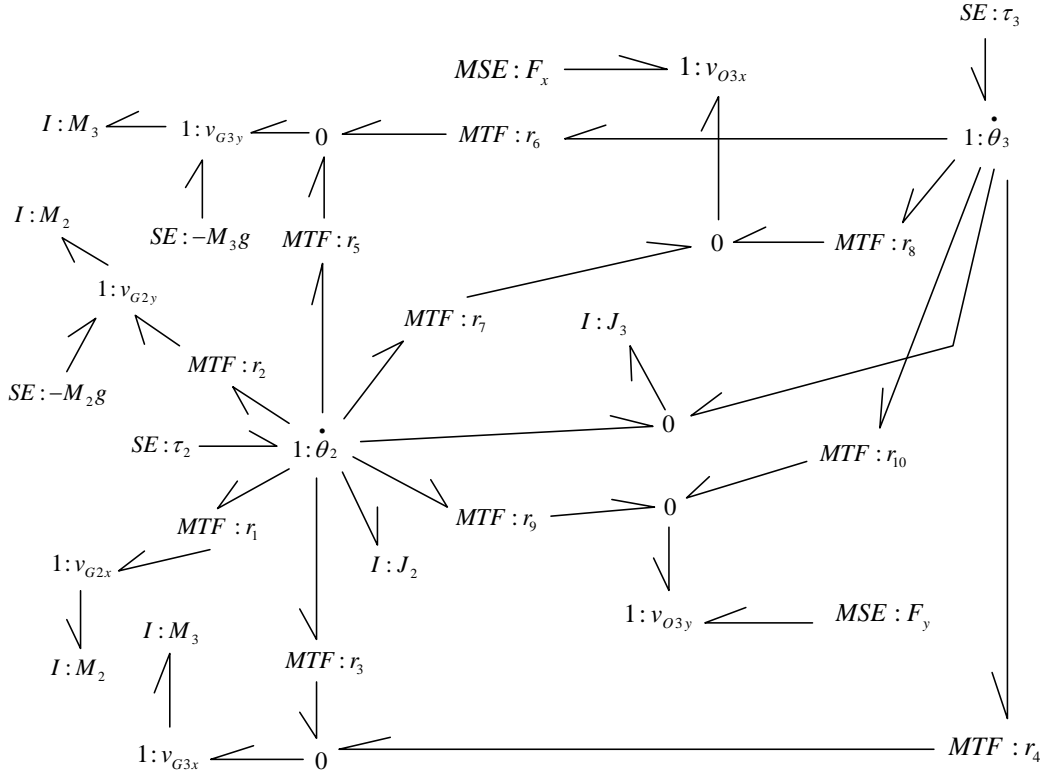


Figure 3.14: A non causal bond graph model representing the mechanical dynamics of a 2-link manipulator

The joint torques applied to each of the joint by the respective actuator can be obtained systematically from the bond graph using the constitutive relations, and noting that $F_x = F_y = 0$ since the manipulator is moving in free space. The external torque applied to move link 3 can be obtained from the bond graph as;

$$\begin{aligned}
 \tau_3 &= e_{16} = e_{14} + e_{15} + e_{17} + e_{30} + e_{36} \\
 &= \frac{1}{3}m_3l^2\ddot{\theta}_2 + \frac{1}{3}m_3l^2\ddot{\theta}_3 + \frac{1}{2}m_3l^2\ddot{\theta}_2 \cos \theta_3 + \frac{1}{2}m_3l^2\dot{\theta}_2^2 \sin \theta_3 \\
 &\quad + \frac{1}{2}m_3gl \cos(\theta_2 + \theta_3)
 \end{aligned} \tag{3.55}$$

The external torque applied to move link 2 can be obtained from the bond graph as;

$$\begin{aligned}
\tau_2 &= e_1 = e_2 + e_3 + e_6 + e_{10} + e_{19} + e_{25} + e_{31} + e_{37} \\
&= \frac{1}{3}m_2l^2\ddot{\theta}_2 + \frac{4}{3}m_3l^2\ddot{\theta}_2 + \frac{1}{3}m_3l^2\ddot{\theta}_3 + m_3l^2\ddot{\theta}_2 \cos \theta_3 + \frac{1}{2}m_3l^2\ddot{\theta}_3 \cos \theta_3 - m_3l^2\dot{\theta}_2\dot{\theta}_3 \sin \theta_3 \\
&\quad - \frac{1}{2}m_3l^2\dot{\theta}_2^2 \sin \theta_3 + \frac{1}{2}m_2gl \cos \theta_2 + m_3gl \cos \theta_2 + \frac{1}{2}m_3g \cos(\theta_2 + \theta_3) \quad (3.56)
\end{aligned}$$

The equations of external torque given in Equations 3.55 and 3.56 correspond to those obtained using Newton-Euler and Lagrangian methods for the same planar manipulator, as illustrated in [16, 17]. This indicates that, the model developed captures the essential aspects of rigid body dynamics of the manipulator.

CHAPTER 4

MODELING THE DYNAMICS OF HYDRAULIC ACTUATION OF THE EXCAVATOR

4.1 Bond Graph Model Development

The hydraulic system is driven by one axial piston pump which takes low-pressure oil from the a reservoir tank (at atmospheric pressure) and outputs high pressure oil. The high-pressure oil flows to the cylinders, which in turn actuate the different joints. The flow from the pump to the cylinders is controlled through spool valves which meters out the oil through variable orifices.

The hydraulic dynamics to be modeled are the actuator dynamics, which herein refer to the dynamics of the hydraulic pump, spool valves and the hydraulic cylinders responsible for moving the joints of the excavating manipulator. Since all the links are actuated by hydraulic cylinders, one model (with variable parameters) representing the dynamics of a valve-controlled linear cylinder shown in Figure 4.1 was developed.

The following is a summary of the assumptions that were made when developing the bond graph dynamic model of an hydraulic cylinder;

- The hydraulic pump delivers a constant supply pressure, irrespective of the oil flow demand. This implies that P_S is constant.
- The reservoir (tank) pressure is constant and at atmospheric pressure. Since gauge pressures are considered then $P_r = 0$.
- The flows through the valves are turbulent.

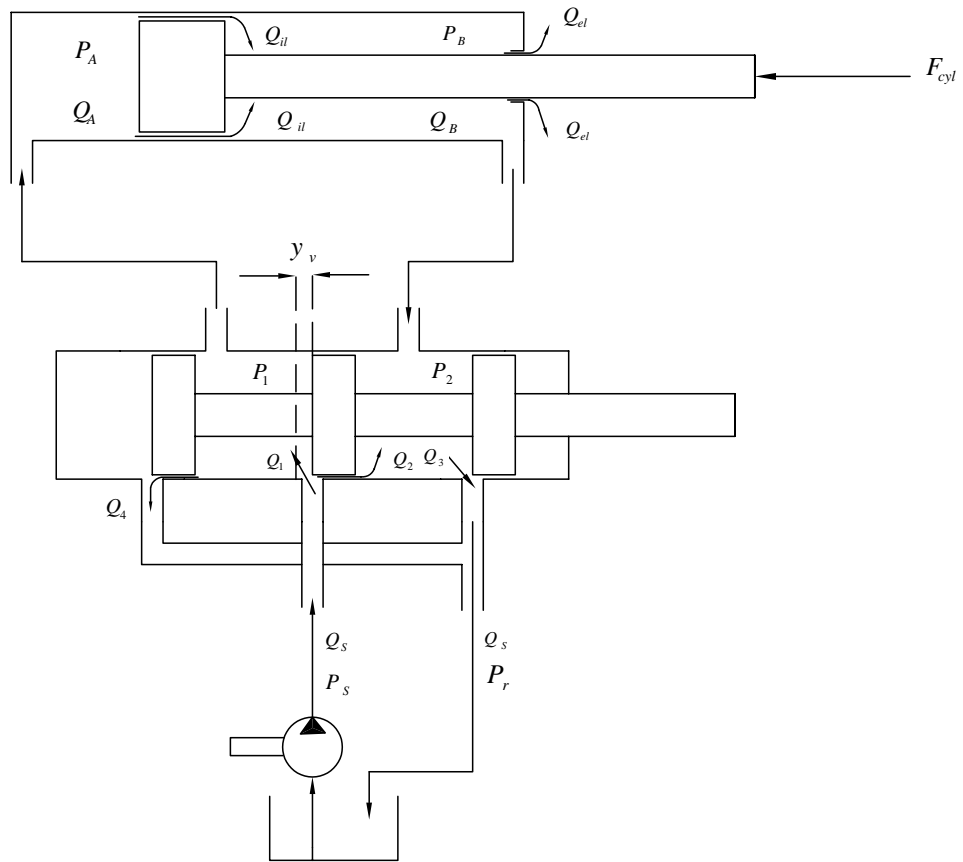


Figure 4.1: Schematic diagram of a valve controlled hydraulic cylinder

- The leakage flow through the clearance between the cylinder and the piston is laminar.
- Possible dynamical behavior of the pressure in the transmission lines between valves and actuators are assumed to be negligible. This means that $P_A = P_1$, and $P_B = P_2$.
- The spool valve is matched and symmetrical. Its band-width is much higher than the band-width of the cylinder, so that the valve dynamics due to inertia can be neglected [11].

- External leakage Q_{el} between the piston rod and the external seals is neglected. This is because external leakage on the cylinder must be avoided by use of improved sealing technology.
- Inefficient volumes, i.e., the volume of the fluid in the hoses between the valve and the actuator, and the volume of oil existing in the cylinder, are neglected.

4.1.1 Pump

The pump is assumed to be an ideal source of power capable of supplying constant pressure at any flow required. Therefore the pump can be modeled in bond graph form as an effort source, as shown in Figure 4.2.

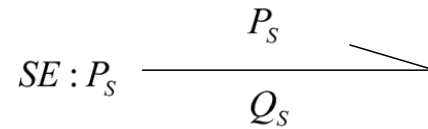


Figure 4.2: Constant pressure pump bond graph model

4.1.2 Spool Valves

One of the criteria in selecting valves is to consider their response time. If the resonant frequency of the spool valve is very high, its dynamic behavior is negligible compared to the relatively low resonant frequency of the system [43]. A typical industrial manipulator has a natural frequency in the range of $1 - 5Hz$, while the cut-off frequency of the selected valves when operating under maximum command must be in the range of $10 - 15Hz$ [44]. Thus only the resistive effect of the valve is considered.

To model the dynamics of the spool valve due to its resistive effect to the fluid flow,

the following two assumptions are made for analysis;

- The hydraulic fluid is ideal, non-viscous and incompressible. This assumption is close to reality under most conditions and is also justified as far as phenomena inside the valve are considered.
- Valve geometry is ideal. This implies that the edges of the metering orifices are sharp and that the working clearances are zero, hence no-internal leakage condition is assumed [45–47].

The orifice flow equation governing flow and pressure drop across an orifice (for turbulent flow) is known to be [46],

$$Q = C_d A_O \sqrt{\frac{2}{\rho} \Delta P} \quad (4.1)$$

Where;

Q is the flow rate through the orifice.

ΔP is the pressure drop across the orifice.

C_d is the discharge coefficient.

ρ is the fluid density.

A_O is the area of the orifice opening.

Equation 4.1 shows that the relative flow rates are dependent on the pressure drops across the valves, which in turn are dependent on the forces acting on the actuator.

Let the spool be given a positive displacement from the neutral position, i.e, $y_v = 0$ which is chosen to be the symmetrical position of the spool in its sleeve. Using Equation 4.1, the flow rates through the metering orifices are,

$$Q_1 = C_d A_{O1} \sqrt{\frac{2}{\rho} (P_S - P_1)} \quad (4.2)$$

$$Q_2 = C_d A_{O2} \sqrt{\frac{2}{\rho} (P_S - P_2)} \quad (4.3)$$

$$Q_3 = C_d A_{O3} \sqrt{\frac{2}{\rho} (P_2 - P_r)} \quad (4.4)$$

and

$$Q_4 = C_d A_{O4} \sqrt{\frac{2}{\rho} (P_1 - P_r)} \quad (4.5)$$

The return pressure $P_r = 0$, since the tank pressure is taken to be at atmospheric. Since the geometry of the valve is assumed ideal and the valving orifices are matched and symmetrical then $Q_2 = Q_4 = 0$, and $A_{O1} = A_{O3} = A_O(y_v)$.

Note that from Figure 4.1, the total supply flow (Q_S) is given as;

$$Q_S = Q_1 + Q_2 = Q_1 \quad (4.6)$$

and also as;

$$Q_S = Q_3 + Q_4 = Q_3 \quad (4.7)$$

From Figure 4.1, flow to the chamber A of cylinder and flow out of chamber B of the cylinder are given as;

$$\begin{aligned} Q_A &= Q_1 - Q_4 \\ &= Q_1 \\ &= C_d A_O(y_v) \sqrt{\frac{2}{\rho} (P_s - P_A)} \end{aligned} \quad (4.8)$$

and

$$\begin{aligned}
 Q_B &= Q_3 - Q_2 \\
 &= Q_3 \\
 &= C_d A_O(y_v) \sqrt{\frac{2}{\rho} (P_B - P_r)} \quad (4.9)
 \end{aligned}$$

The area of the valve orifice opening is dependent on the valve spool displacement (y_v) as shown in Figure 4.3. If the port is of radius r , the uncovered area of the orifice where the fluid passes is presented next.

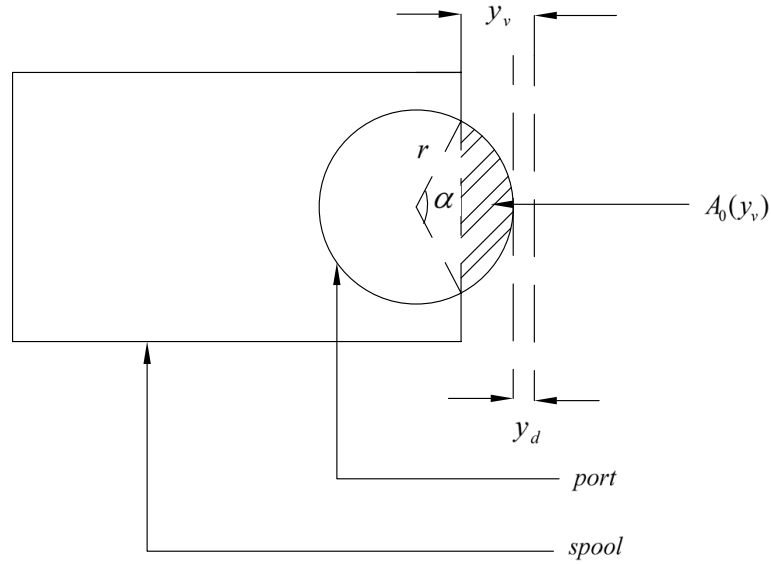


Figure 4.3: Variation of valve orifice area with spool movement

$$\begin{aligned}
 A_O(y_v) &= \frac{\alpha}{2\pi} \pi r^2 - \frac{1}{2} (2r \sin \frac{\alpha}{2}) r \cos \frac{\alpha}{2} \\
 &= \frac{r^2}{2} (\alpha - \sin \alpha) \quad (4.10)
 \end{aligned}$$

Where α varies with the valve displacement as shown below;

$$\begin{aligned}\cos \frac{\alpha}{2} &= \frac{r - (y_v - y_d)}{r} \\ \alpha &= 2 \cos^{-1} \left(\frac{r - (y_v - y_d)}{r} \right)\end{aligned}\quad (4.11)$$

Equations 4.8 and 4.9 show that the flow that is transferred from the pump to the cylinder is determined by the flow coefficient, the area of the valve orifice and the pressure difference.

Equations 4.8 and 4.9, are appropriate expressions for the constitutive relations of orifice resistances to the flow rate to and from the cylinder and can be represented as;

$$P_s - P_A = \Delta P_A = \frac{\rho}{2C_d^2(A_O(y_v))^2} Q_A |Q_A| = R_1 Q_A |Q_A| \quad (4.12)$$

and

$$P_B - P_r = \Delta P_B = \frac{\rho}{2C_d^2(A_O(y_v))^2} Q_B |Q_B| = R_2 Q_B |Q_B| \quad (4.13)$$

The absolute value sign has been used to correct the sign in the pressure drop for negative flow rate.

Equations 4.12 and 4.13 show that the valve resistances are equal, i.e.,

$$R_1 = R_2 = \frac{\rho}{2C_d^2(A_O(y_v))^2} \quad (4.14)$$

Hence the valve resistances R_1 and R_2 given in Equation 4.14 depend on the position of the valve (y_v). The bond graph representation of the valve resistance effects to the fluid flow to and from the cylinder are shown in Figures 4.4 and 4.5.

An active bond has been used to indicate that the valve resistances depend on the valve displacements. An active bond is just like a signal in a block diagram, and is

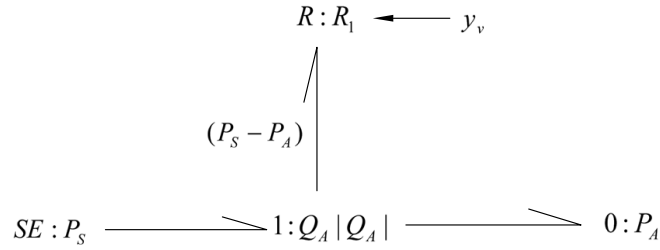


Figure 4.4: Bond graph representation of valve resistance to forward flow

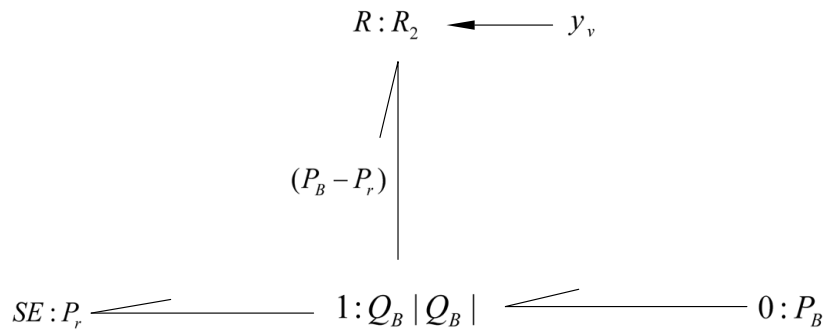


Figure 4.5: Bond graph representation of valve resistance to return flow

shown with a full arrow. The active bond implies that no feedback effect is considered, i.e., an effort or flow signal is transmitted in one direction, the complimentary signal does not flow in the opposite direction as in a normal bond [28].

4.1.3 Linear Cylinders

Three single-ended type of hydraulic cylinders will be used to actuate the boom, arm, and bucket links of the excavating manipulator. The following two assumptions are made before deriving the bond graph model of the cylinder;

- The cylinder chambers are assumed to be rigid, i.e., no compliance in the walls. The stiffness of the cylinder chambers is more than five times higher than that of the hydraulic oil. Therefore when operating at the same pressure

range, the compliance effect from cylinder walls is negligible compared to the oil compliance.

- Viscous friction effects in the piston seals are assumed to be dominant compared to the coulomb friction effects. Hydraulic oil lubricates the sliding passages in the cylinder and this greatly reduces the effects of coulomb friction.

Figure 4.6 shows a schematic diagram of a hydraulic cylinder. The cylinder piston has diameter D_p , area A_p and the rod has diameter D_r and area A_r .

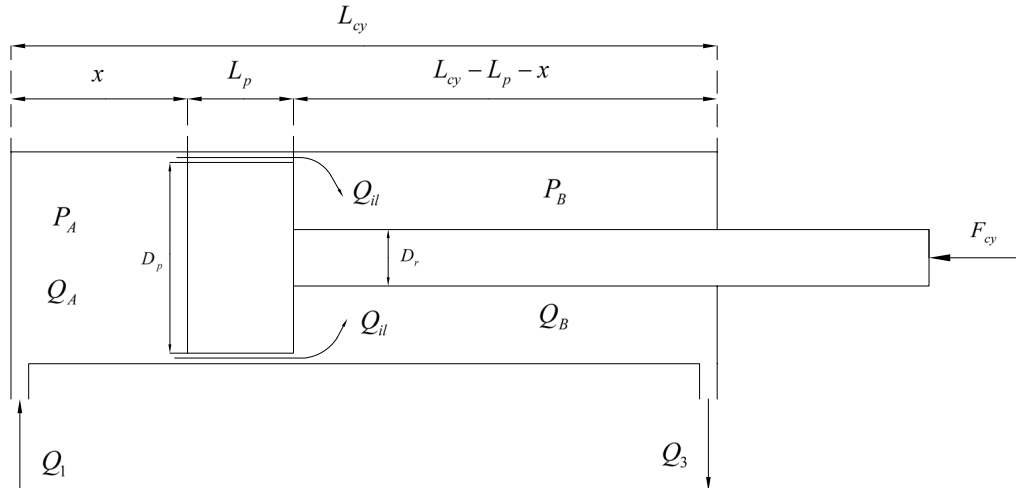


Figure 4.6: Schematic diagram of the linear actuator

The chamber at the head side has a pressure P_A and flow rate Q_A , and are positive into the cylinder. The chamber at the rod side has pressure P_B and flow rate Q_B , and are positive out of the cylinder.

Hydraulic cylinders transform hydraulic energy into mechanical energy, i.e., the pressure difference at the two cylinder chambers provide mechanical force which

drives the piston. Bond graph method identifies this transformation in terms of transformer elements, which can be represented as shown in Figure 4.7.

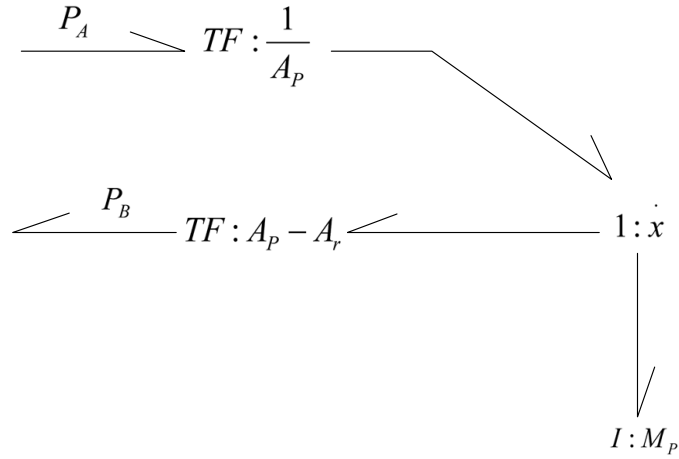


Figure 4.7: Bond graph representation of the pressure difference in cylinder chambers

The piston and rod mass of the cylinder, is modeled as a I –element which is attached to the 1–junction with the piston velocity (\dot{x}) as the common variable.

4.1.3.1 Modeling Compressibility of Oil in a Hydraulic Cylinder

The influence of the finite oil stiffness on the dynamics of hydraulic system is similar to that of a spring compressibility in mechanical systems. A measure of oil compressibility is the bulk modulus, which relates the variation of pressure and volume of oil in a closed vessel as shown below [46],

$$\Delta p = \beta \left(\frac{-\Delta V}{V} \right) \quad (4.15)$$

where

β is the Bulk Modulus of the fluid

ΔV is the decrease in volume of the fluid due to pressure

V is the volume itself.

Equation 4.15 is usually considered the constitutive law of a linear one port C -element of compliance $C = \frac{V}{\beta}$, attached to the zero junction representing the hydrostatic pressure [48], as shown in Figure 4.8

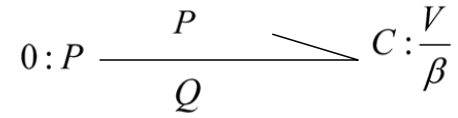


Figure 4.8: C -element representing fluid compressibility

Application of Equation 4.15 to the chambers of a hydraulic cylinder however reveals a problem with respect to a correct bond graph representation, since the chamber volume depends on the displacement x of the piston. Therefore,

$$\Delta p = \beta \frac{-\Delta V}{V_o + A_p x_p} \quad (4.16)$$

where

V_o is the volume of chamber at start position $x = x_o$

A_p is the area of the piston.

The compliance $\frac{V_o + A_p x}{\beta}$ can be considered as a displacement dependent compliance ($C(x)$), i.e.,

$$C(x) = \frac{V_o + A_p x}{\beta} \quad (4.17)$$

Equation 4.17 can be depicted in the bond graph by means of a modulation signal as shown in Figure 4.9

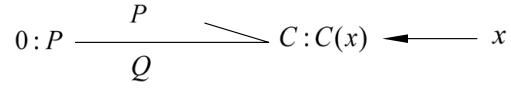


Figure 4.9: Displacement Modulated C element

The displacement dependent compliance in Equation 4.17 has been taken into account without expressing the modulation in the bond graph [49], but this means that the bond graph does not properly correspond to the mathematical model in use.

Each chamber therefore has displacement dependent compliance C_A and C_B given as;

$$C_A = \frac{V_A}{\beta} = \frac{A_p x}{\beta} \quad (4.18)$$

and

$$C_B = \frac{V_B}{\beta} = \frac{(A_p - A_r)(L_{cy} - L_p - x)}{\beta} \quad (4.19)$$

Which can be represented in bond graph form as in Figures 4.10 and 4.11,

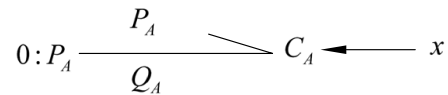


Figure 4.10: Displacement Modulated C element of cylinder chamber A

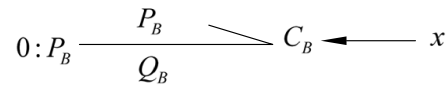


Figure 4.11: Displacement Modulated C element of cylinder chamber B

4.1.3.2 Modeling the Leakage Flows

There is always some clearance between the cylinder and the piston to allow relative motion. Even though these clearances are small in comparison with the normal cross-sectional area of the oil flow in a circuit, they act as leakage paths when pressure drops are imposed [11]. Internal leakage occurs in hydraulic cylinders as result of a pressure difference existing between the two chamber.

The fluid flow rate in the clearance can be obtained from Hagen-Poiseuille equation as;

$$Q_{il} = \frac{\pi D_p c^3}{12\mu L_p} (P_A - P_B) \quad (4.20)$$

Equation 4.20 can be depicted in bond graph form as shown in Figure 4.12 below;

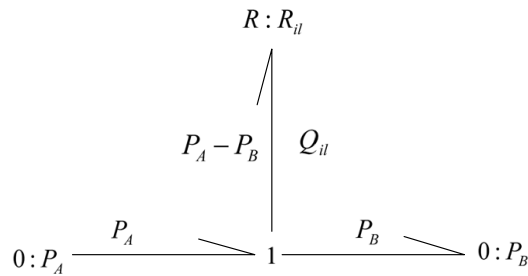


Figure 4.12: Bond graph model representing the leakage in piston and cylinder wall clearance

Where

$$R_{il} = \frac{12\mu L_p}{\pi D_p c^3} \quad (4.21)$$

4.1.3.3 Modeling the Viscous Friction

Another object in developing a correct bond graph model of a double acting hydraulic cylinder is the viscous friction which generally oppose the piston movements.

This viscous friction has been considered by few authors, e.g. in [48, 50], often it is simply neglected.

Viscous friction due to piston movement is described by Newton's law as [46],

$$F_N = \mu \frac{A}{c} \frac{\partial x}{\partial t} = \mu \frac{\pi D_p L_p}{c} \dot{x} \quad (4.22)$$

This viscous friction due to the piston movement is modeled as a R -element attached to the 1-junction with the piston velocity (\dot{x}) as the common variable. This is shown in Figure 4.13,

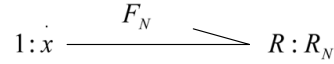


Figure 4.13: Bond graph model representing the viscous friction due to piston movement

Where

$$R_N = \frac{\mu \pi D_p L_p}{c} \quad (4.23)$$

4.1.4 Bond Graph Model of a Valve Controlled Cylinder

Figure 4.14 shows the overall bond graph model of a valve-controlled hydraulic cylinder with causality assigned using Sequential Causality Assignment Procedure (SCAP) as clearly illustrated in [29, 31, 34]. The model is obtained by assembling the sub models of the hydraulic components which have been already developed. The bonds are numbered for easier analysis purposes.

4.2 Checking the Bond Graph Model

The bond graph model of the hydraulic dynamics of the actuator was validated first before coupling it to the model representing mechanical dynamics of the excavating

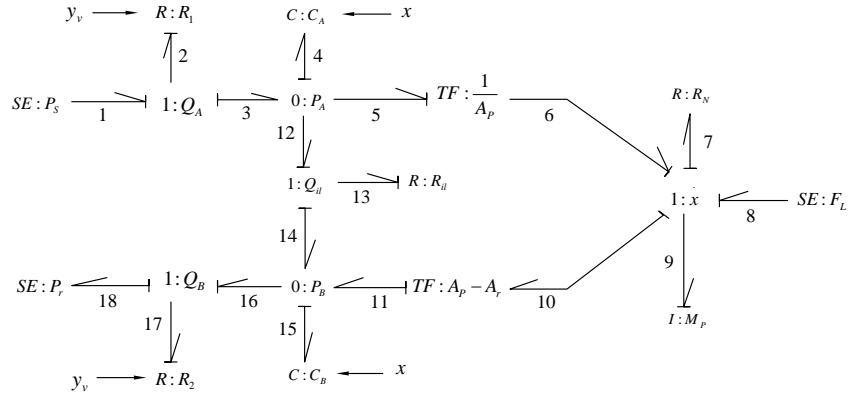


Figure 4.14: A causal bond graph model for the cylinder during extension

manipulator. The validation was done by comparing the open loop state responses of the cylinder obtained from simulating the bond graph model, to those obtained by simulating the Ordinary Differential Equation (ODE) model of a cylinder developed by Nguyen [11] based on the same assumptions. The designed arm cylinder parameters as shown in Table 4.1 together with hydraulic parameters in Table 4.2 were used in simulating the two models.

Table 4.1: Hydraulic cylinder parameters

Parameter description		Units	Boom	Arm	Bucket
Length of cylinder barrel	L_{cy}	<i>mm</i>	480	320	395
Length of rod,	L_r	<i>mm</i>	450	290	365
Length of stroke,	L_s	<i>mm</i>	430	270	345
Length of piston,	L_p	<i>mm</i>	50	50	50
Diameter of piston,	D_p	<i>mm</i>	63.5	63.5	63.5
Diameter of rod,	D_r	<i>mm</i>	28.5	28.5	28.5
Length of end cap1 ,	L_{e1}	<i>mm</i>	30	30	30
Length of end cap2,	L_{e2}	<i>mm</i>	40	40	40
Length of bracket1,	L_1	<i>mm</i>	50	50	50
Length of bracket2,	L_2	<i>mm</i>	20	20	20

Table 4.2: Pump, valve and hydraulic parameters

Pump parameters		
Maximum operating pressure (P_{\max})	17.0×10^6	<i>Pa</i>
Maximum flow rate (Q_{\max})	65	<i>lit / min</i>
Maximum speed (N_{\max})	2500	<i>rpm</i>
Supply pressure (P_s)	14.5×10^6	<i>Pa</i>
Directional control valve parameters		
Discharge coefficient (C_d)	0.61	
Diameter of ports (d)	9.525	<i>mm</i>
Maximum flow rate (Q_{\max})	40	<i>lit / min</i>
Maximum operating pressure (P_{\max})	35.0×10^6	<i>Pa</i>
Hydraulic fluid parameters		
Bulk modulus (β)	1.6×10^9	<i>Pa</i>
Fluid density (ρ)	850	<i>Kg / m³</i>
Fluid absolute viscosity (μ) at 25 ^o C	7.9×10^{-4}	<i>m² / s</i>

To simulate the state responses of the hydraulic cylinder from bond graph model, the causal bond graph model of the hydraulic cylinder shown in Figure 4.14 under no load $F_L = 0$, was first converted into block diagram using the Fakri method [32]. The block diagram representing the bond graph was then simulated on SIMULINK to obtain the state responses of the hydraulic cylinder on extension/retraction and under no load.

The ODE model of a hydraulic cylinder developed by Nguyen [11] based on first principles of the basic laws of mass continuity (continuity Equation) and the Equation of motion for mechanical moving parts (Newton's second law), has the following state space representation;

$$\dot{y}_1 = y_2 \quad (4.24)$$

$$\dot{y}_2 = \frac{1}{M_p} \left[y_3 A_p - y_4 (A_p - A_r) - \frac{\mu \pi D_p L_p}{c} y_2 - F_L \right] \quad (4.25)$$

$$\dot{y}_3 = \frac{\beta}{A_p y_1} \left[C_d A_O(y_v) \sqrt{\frac{2}{\rho} (P_S - y_3)} - A_p y_2 - C_{ip} (y_3 - y_4) \right] \quad (4.26)$$

$$\dot{y}_4 = \frac{\beta}{(A_p - A_r)(L_{cy} - L_p - y_1)} \left[-C_d A_O(y_v) \sqrt{\frac{2}{\rho} y_4} + (A_p - A_r) y_2 - C_{ip} (y_3 - y_4) \right] \quad (4.27)$$

where a state vector was defined as;

$$\begin{pmatrix} y_1 \\ y_2 \\ y_3 \\ y_4 \end{pmatrix} = \begin{pmatrix} x \\ \dot{x} \\ P_A \\ P_B \end{pmatrix} \quad (4.28)$$

Equations 4.24 to 4.27 can be solved using MATLAB ODE-solvers, and then the state responses simulated. The open loop state responses of the cylinder on extension and retraction are shown in Figures 4.15, and 4.16 respectively.

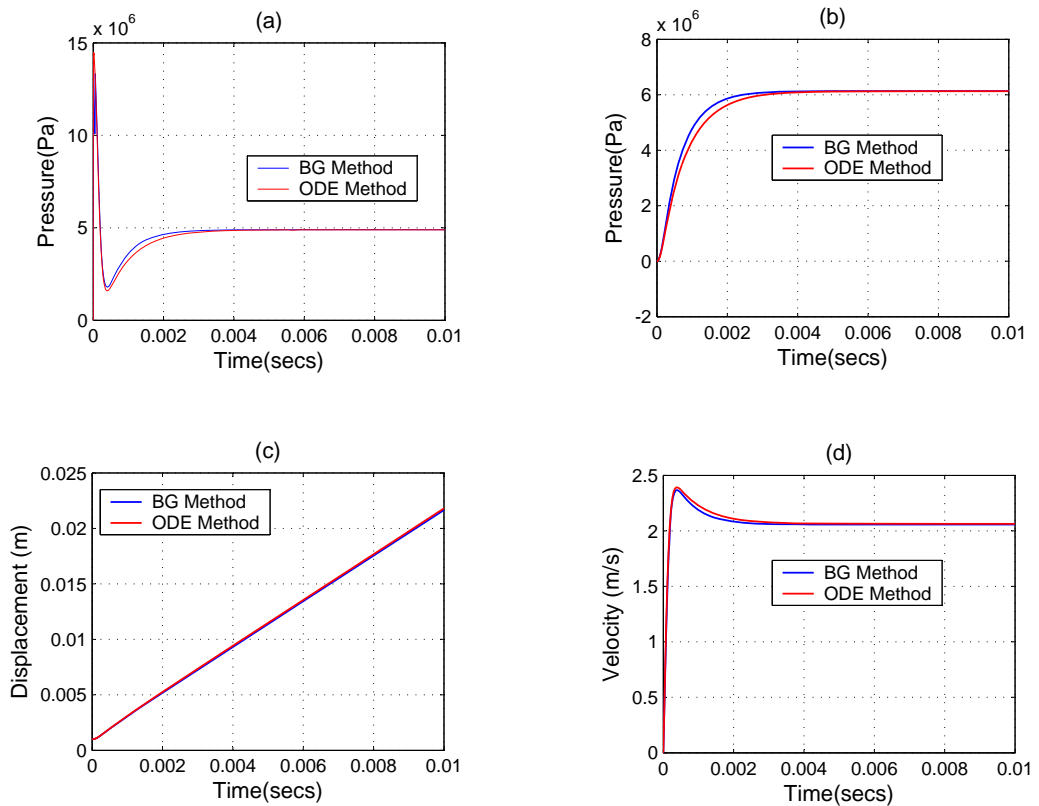


Figure 4.15: Simulated open loop responses of the arm cylinder for extension case;
(a) Head side chamber pressure **(b)** Rod side chamber pressure **(c)**
Piston displacement **(d)** Piston velocity

Such a fast response of approximately 0.002 seconds for the cylinder states can be explained by the fact that the cylinder is moving no load and the spool valve is assumed to be completely open at the start of the simulation. Further interpretation of the state responses is not done simply because the idea of simulating the models at this stage was to compare the simulation results of the bond graph model to those of the ODE model. The results are seen to compare favorably, and now the hydraulic model can be confidently integrated to the manipulator's mechanical model.

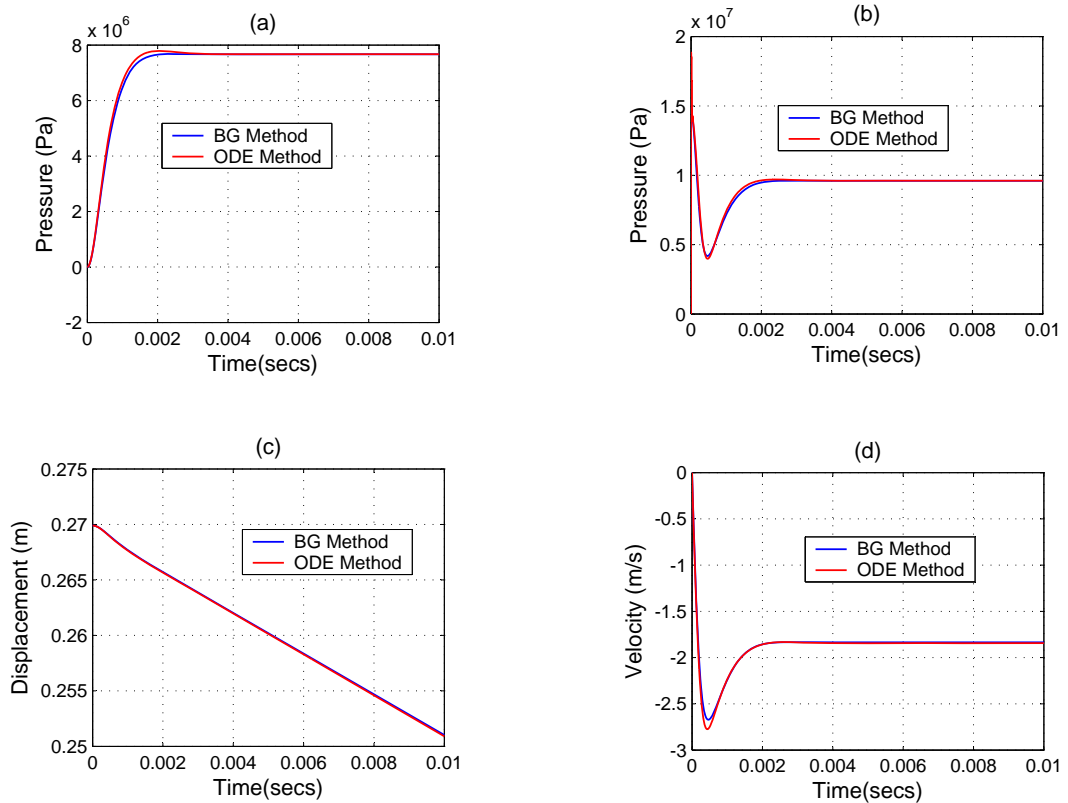


Figure 4.16: Simulated open loop responses of the arm cylinder for retraction case; **(a)** Head side chamber pressure **(b)** Rod side chamber pressure **(c)** Piston displacement **(d)** Piston velocity

4.3 Inter-Actuator Interaction

Among the characteristics which must be captured by the dynamic model of a mobile hydro-mechanical system with an articulated arm are the actuator interactions which are important since they significantly affect the overall response of the system [51]. The interaction between the different actuators occurs due to the fact that they are powered by a single power engine. When multiple actuators request flow simultaneously, the power demand may exceed the capacity of the engine. The hydraulic system is forced to reduce the flow to the cylinders to keep the engine

from stalling. Therefore the actuator interaction is an important part of system dynamics and must be modeled.

Singh et al. [52] used a simple approach to handle the flow distribution between multiple hydraulic actuators. The authors assumed a fixed pump flow (even though pumps vary their output), and assumed that the circuit with a valve closest to the pump gets all the flow it requires, and that the remaining flow is distributed among the rest. This approach is valid when the cylinders have similar force loads, but not when the cylinders have very different force loads. There is no literature available on how to model the flow distribution of multiple cylinders without resorting to detailed model. The following approach addresses this shortcoming.

The hydraulic actuators driving the manipulator links are powered by one pump. Since the pump is modeled as a constant pressure supply, it supplies a constant pressure to all cylinders regardless of the flow demand across each actuator. Therefore an Effort Source with constant pressure as the source (that is, $SE : P_S$), is connected to the zero junction from which the cylinders are supplied with constant pressure.

To demonstrate the inter-actuator interaction, two cylinders being driven by one hydraulic pump as shown in Figure 4.17 are considered. The bond graph model representing the actuators is shown in Figure 4.18.

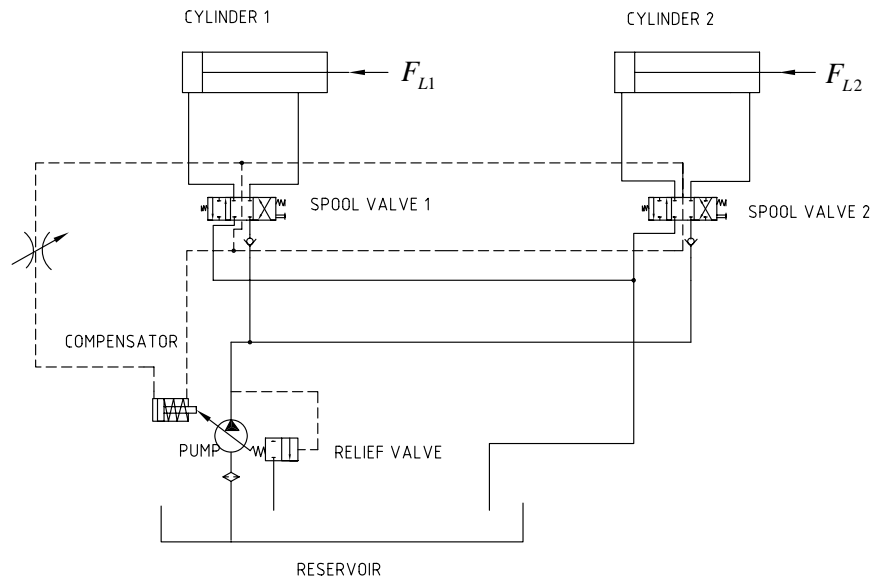


Figure 4.17: Hydraulic circuit for two cylinders powered by one pump

Using the parameters of the boom and arm cylinders as given in Table 4.1 together with hydraulic parameters in Table 4.2, the open loop responses of the hydraulic actuators under step inputs are simulated for four cases, that is,

Case 1 When the two cylinders are moving no load and their directional control valves are equally displaced.

Case 2 When the two cylinders are moving no load and one directional control valve, i.e., for cylinder 1 is closed.

Case 3 When the cylinders are moving no load and the step inputs to the cylinders are different.

Case 4 When the two cylinders are moving different loads.

Four open loop state responses of the cylinders, that is, chamber pressures, fluid flow rates, piston velocities, and piston displacements (the integral of piston velocities),

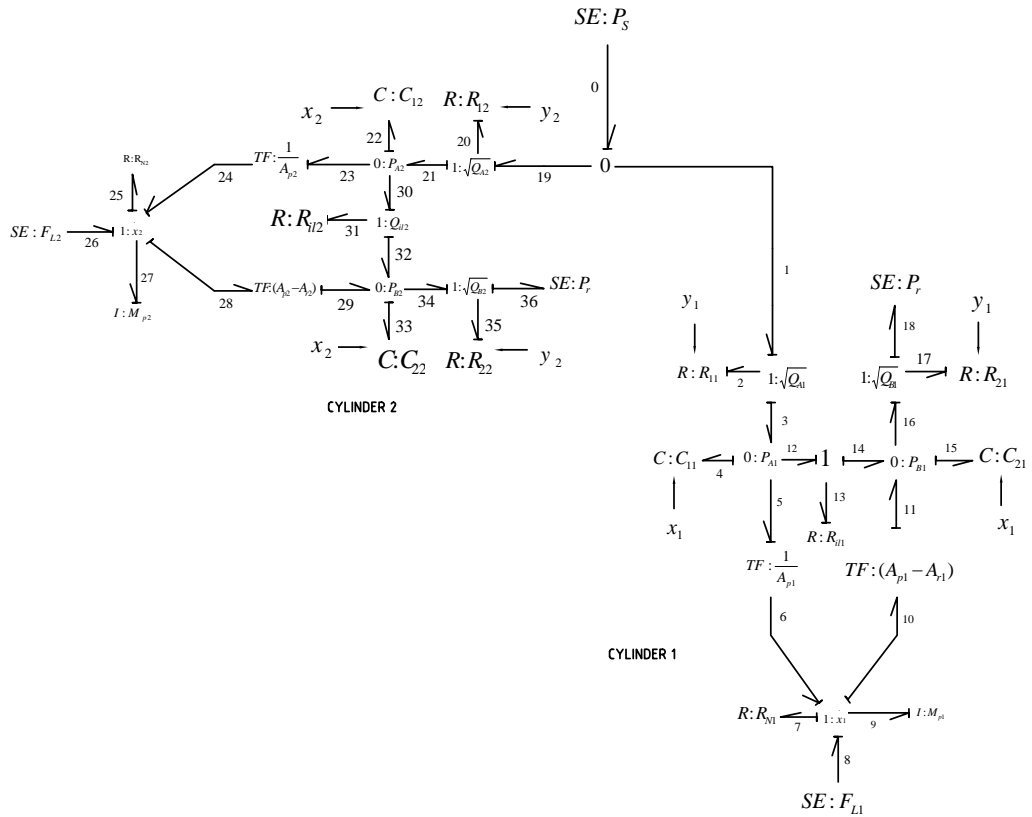


Figure 4.18: Bond graph models of two hydraulic cylinders powered by one pump were simulated to show how the dynamics of the two cylinders interacted during the hydraulic system performance under the above conditions.

Case 1

In this case the two cylinders were given equal step inputs equivalent to the maximum spool valve displacements, and their open loop responses simulated when the cylinders were assumed to move no load.

As seen in Figure 4.19, the only difference between the response curves of the two cylinders is the speed of response. Cylinder 2 which has a smaller piston and rod mass, has a fast response compared to cylinder 1 which has a relatively larger piston

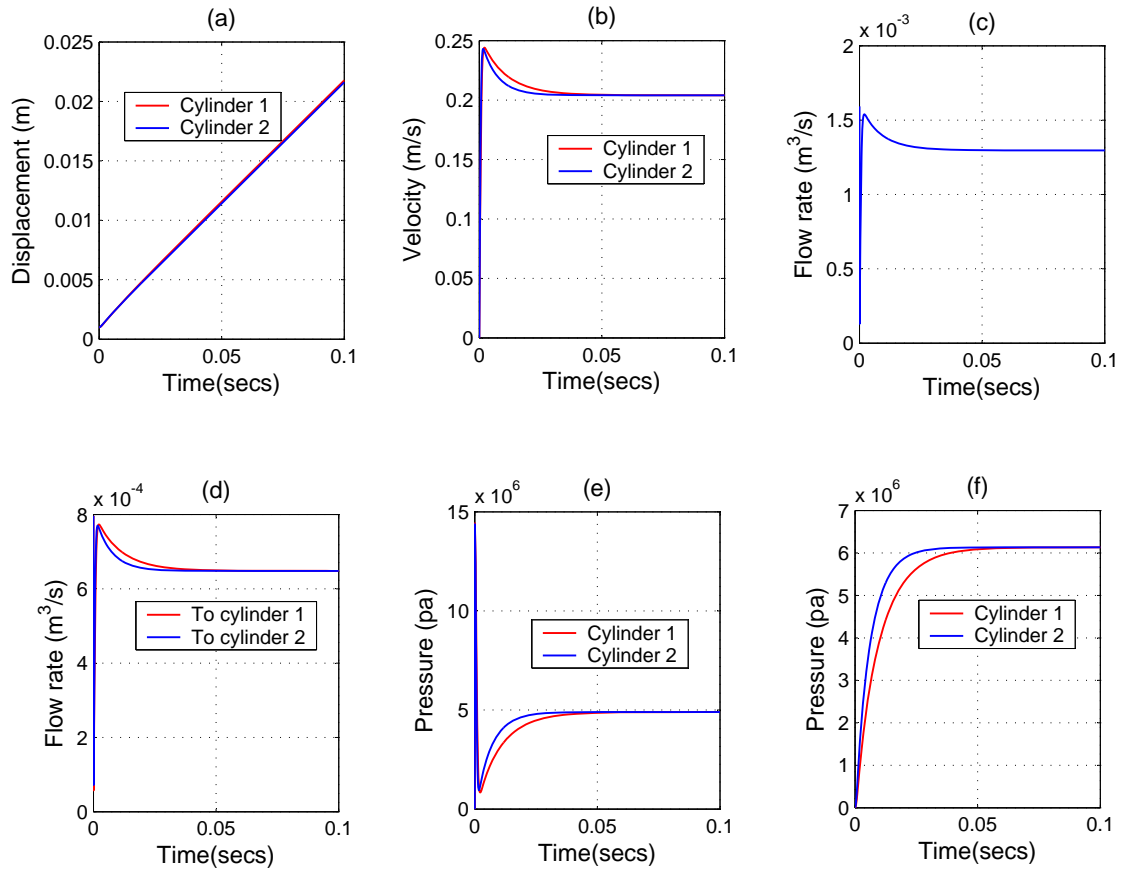


Figure 4.19: Simulated open loop responses for case 1; **(a)** Piston displacements **(b)** Piston velocities **(c)** Pump flow rate **(d)** Flow rate to cylinders **(e)** Head sides chamber pressures **(f)** Rod side chamber pressures

and rod mass. This is what is expected practically since a body with a large mass has a consequent large inertia which slows down the response speed to movements.

Case 2

In this case, the spool valve controlling cylinder 1 remained closed while cylinder 2 was given a step input equivalent to the maximum spool valve displacement. Also the two cylinders were assumed to move no load.

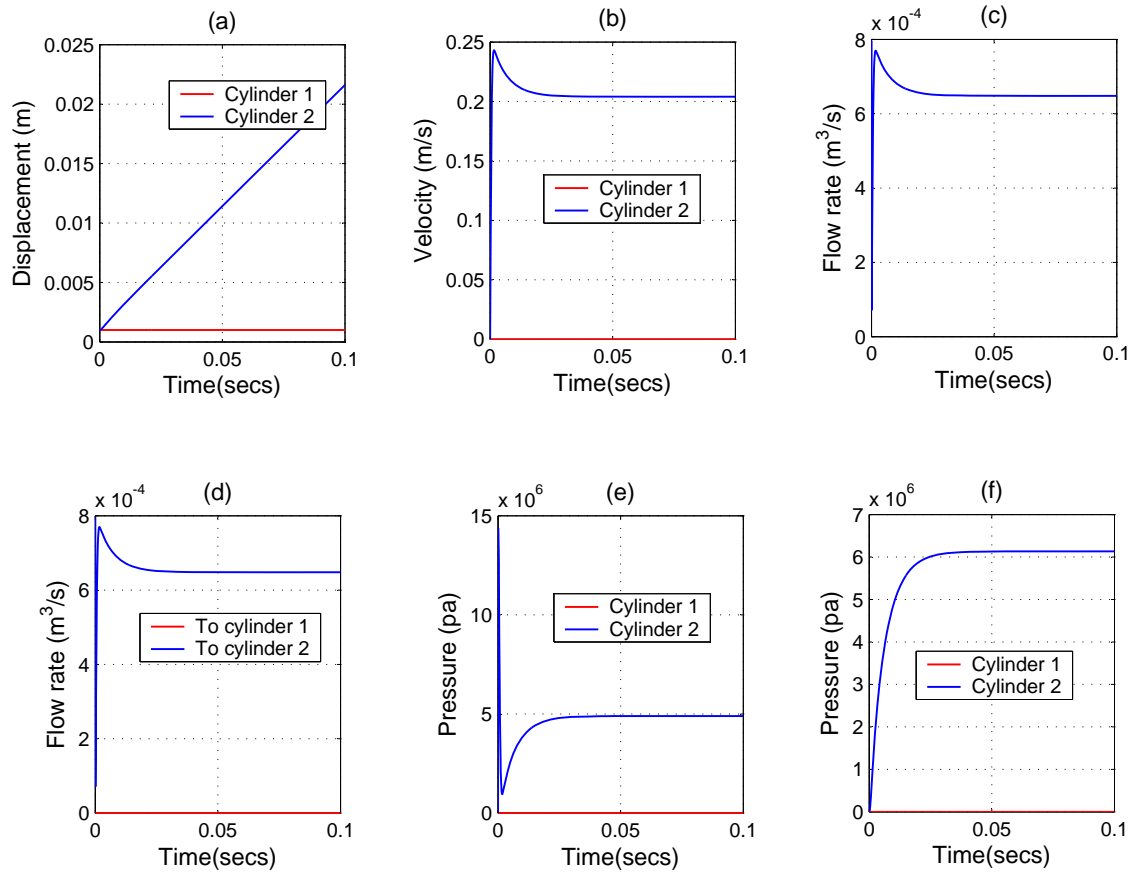


Figure 4.20: Simulated open loop responses for case 2; **(a)** Piston displacements
(b) Piston velocities **(c)** Pump flow rate **(d)** Flow rate to cylinders
(e) Head sides chamber pressures **(f)** Rod side chamber pressures

As seen in Figure 4.20(d), there is no fluid flow to cylinder 1 since the spool valve controlling this cylinder is closed. Due to this, there is no hydraulic pressures generated in cylinder 1 chambers as shown in Figures 4.20(e) and (f), and subsequently the piston of cylinder 1 remains stationary as illustrated in Figure 4.20(a) and (b). The pump produces only the flow required to operate cylinder 2. This flow creates a pressure drop across cylinder 1 which moves the piston of the cylinder. This is what is expected practically, since a hydraulic cylinder whose spool valve is completely closed, has no flow into it and subsequently no motion results, hence no response.

Case 3

In this case, cylinder 2 was given a step input equivalent to the maximum spool displacement, while cylinder 1 was given a step input equivalent to half of the maximum spool displacement. This implies that, the spool valve controlling cylinder 2 had a wider orifice opening than the one controlling cylinder 1.

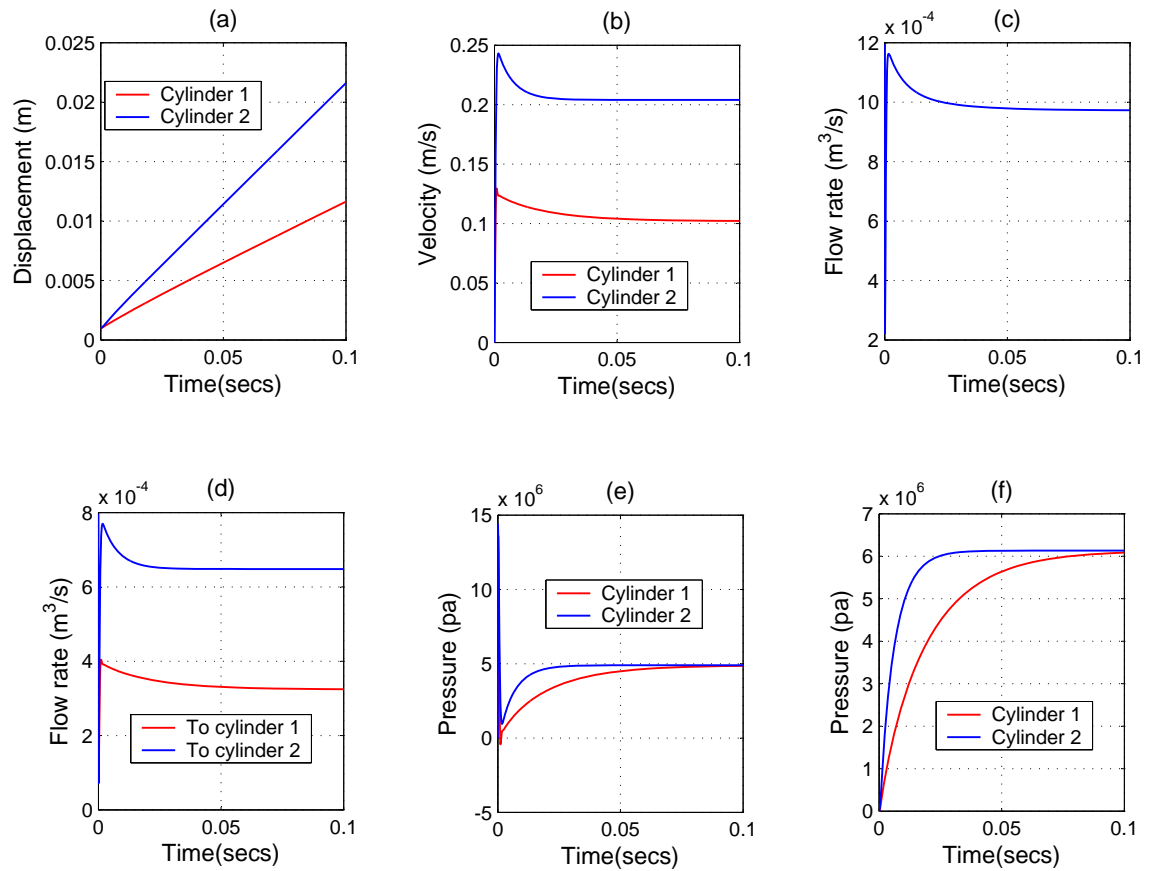


Figure 4.21: Simulated open loop responses for case 3; (a) Piston displacements (b) Piston velocities (c) Pump flow rate (d) Flow rate to cylinders (e) Head sides chamber pressures (f) Rod side chamber pressures

As seen in Figure 4.21(d), cylinder 2 whose directional control valve has a wider orifice opening area receives much fluid flow from the pump as compared to cylinder

1. This is because the larger the area of the orifice, the smaller the valve resistance to fluid flow, and since the flow rate through the valve is inversely proportional to the valve resistance as evident in Equation 4.12, then it follows that, flow rate through the valve is higher for large orifice openings. This larger flow to cylinder 2 results in faster pressure accumulation in the cylinder chambers as shown in Figures 4.21(e) and (f), and this subsequently leads to high piston speeds as evident in Figure 4.21(b).

Case 4

In this case, both cylinders were given similar step inputs equivalent to maximum spool displacements, while the cylinder rods moved different external and translational loads.

Cylinder 1 moves a half of the force moved by cylinder 2. A large pressure drop is required by cylinder 2 so as to produce a force big enough to move the large external load. This large pressure drop for cylinder 2 is evident in Figures 4.22(e) and (f) as compared to a relatively smaller pressure drop required to move a lighter load by cylinder 1. Since the external force to be moved offers a resistance to fluid flow to the actuators, then it follows that the larger the load to be moved, the smaller the fluid flow to the cylinder. This is the reason why fluid flow to cylinder 2 is relatively small compared to the flow to cylinder 1 as shown in Figure 4.22(d). This difference in fluid flow rates to the cylinders results in different cylinder piston speeds as shown in Figures 4.22(b) with a large piston velocity produced by the cylinder moving the smaller load.

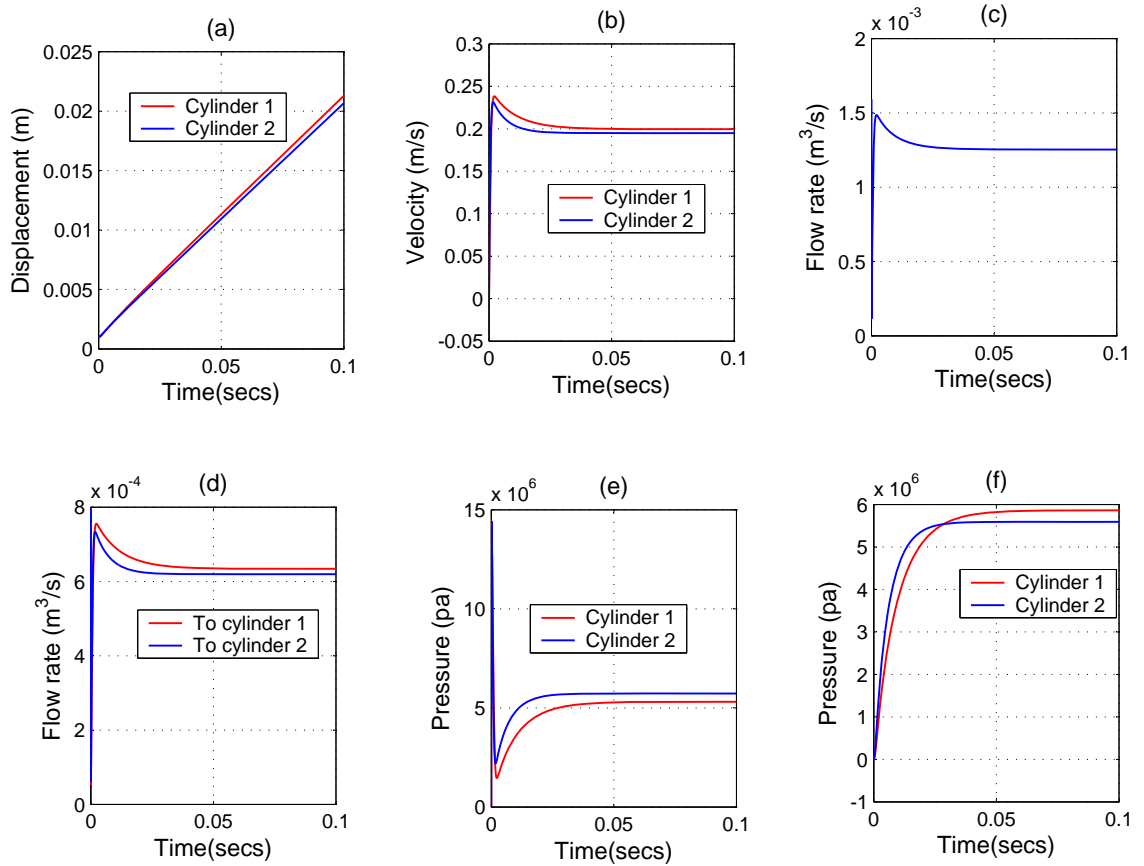


Figure 4.22: Simulated open loop responses for case 4; **(a)** Piston displacements **(b)** Piston velocities **(c)** Pump flow rate **(d)** Flow rate to cylinders **(e)** Head sides chamber pressures **(f)** Rod side chamber pressures

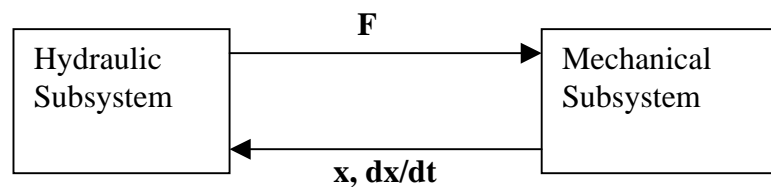
In conclusion, it is seen from the above analysis that, representing the multi-cylinder hydraulic system bond graph models as shown in Figure 4.18, can predict what is practically expected regarding the inter-actuator interaction. Although such assumption is expected to give an error in state responses, since for several cylinders operating simultaneously, each one of them has its own requirement for supply pressure depending on the load and speed required from it, but for simplicity it was assumed that the supply pressure for all the cylinders are equal and constant.

CHAPTER 5

DYNAMIC COUPLING OF THE MECHANICAL AND HYDRAULIC MODELS OF THE EXCAVATOR

5.1 Introduction

The objective of modeling the excavator is to predict the dynamic behavior of the excavating mechanism by combining actuator and manipulator dynamics. Hydraulic cylinders are used to actuate the manipulator joints. They generate forces necessary for boom, arm and bucket motion. These forces are determined by the pressures of the chambers in each actuator, and these pressures, in turn, are determined by the velocity and displacement of the actuator which are calculated from the mechanical dynamics of the excavator [5]. Therefore, it is in these actuators where the dynamic coupling between the mechanical and hydraulic system model of the excavator takes place. Figure 5.1 shows this relationship schematically.



F: Hydraulic cylinder force.
x, dx/dt: Displacement and velocity of the cylinder.

Figure 5.1: Dynamic coupling between the mechanical and hydraulic systems of an excavator

The dynamic models of the manipulator linkage and hydraulic systems of the excavator have been developed in Chapters 3 and 4. From the knowledge of manipulator

dynamics, we have the following well known relations.

$$\dot{X} = J\dot{q} \quad (5.1)$$

$$\tau = J^T F \quad (5.2)$$

Where X is the vector of piston displacements, \dot{X} is the vector of piston velocities, q is the vector of manipulator joint angles, F includes the forces generated by actuators, and τ is the vector of corresponding torques at the manipulator joints. Since boom, arm, and the bucket links are independently actuated, the jacobian matrix J is a diagonal matrix, hence Equation 5.1 can be written as;

$$\begin{pmatrix} \dot{x}_{bo} \\ \dot{x}_a \\ \dot{x}_{bu} \end{pmatrix} = \begin{pmatrix} r_{19} & 0 & 0 \\ 0 & r_{20} & 0 \\ 0 & 0 & r_{21} \end{pmatrix} \begin{pmatrix} \dot{\theta}_2 \\ \dot{\theta}_3 \\ \dot{\theta}_4 \end{pmatrix} \quad (5.3)$$

Where \dot{x}_{bo} , \dot{x}_a and \dot{x}_{bu} are the velocities of the pistons of the boom, arm, and bucket cylinders respectively.

5.2 Deriving the Jacobi Expressions for the Manipulator

The diagonal elements of the Jacobi matrix in Equation 5.3 can be treated as modulated transformer elements in bond graph method since they relate the input and output flow variables in a junction, that is, they transform the angular velocity to the linear velocity of the pistons, and their magnitudes depend on the angular positions of the links.

The length of an hydraulic actuator can be specified by a line segment between the attachment points as shown in Figure 3.1. Therefore;

L_{BE} is the instantaneous length of the boom cylinder

L_{FI} is the instantaneous length of the arm cylinder and

L_{JK} is the instantaneous length of the bucket cylinder.

5.2.1 Boom Link

This is actuated by the boom cylinder which moves joint 2. The equation relating the length of the hydraulic cylinder L_{BE} , to the joint variable θ_2 is presented next.

Consider Figure 5.2 which is obtained from Figure 3.1.

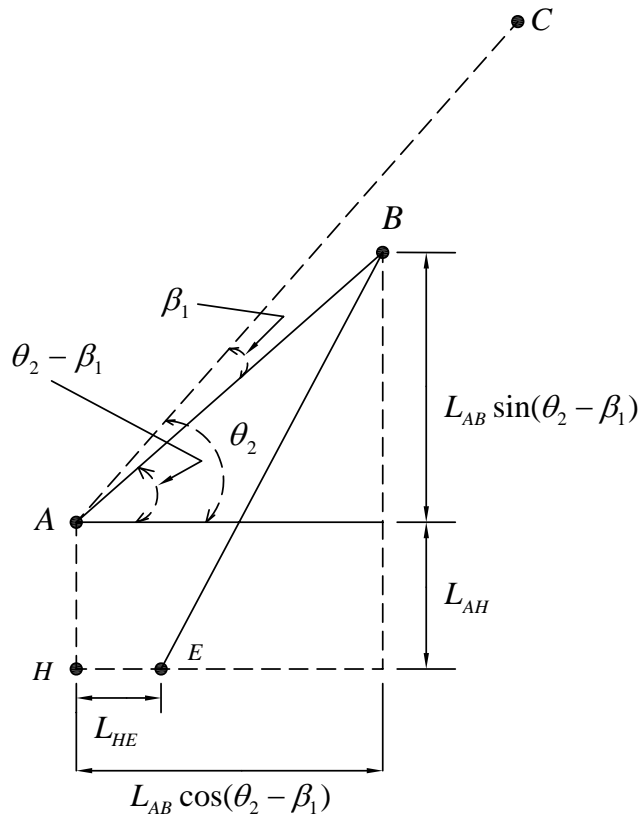


Figure 5.2: Boom cylinder length

Equation 5.4 shows how the length of actuator L_{BE} is related to the joint angle θ_2 ;

$$L_{BE}^2 = [L_{AB} \sin(\theta_2 - \beta_1) + L_{AH}]^2 + [L_{AB} \cos(\theta_2 - \beta_1) - L_{HE}]^2 \quad (5.4)$$

from which L_{BE} is obtained as,

$$L_{BE} = \left[L_{AB}^2 \sin^2(\theta_2 - \beta_1) + 2L_{AB}L_{AH} \sin(\theta_2 - \beta_1) + L_{AH}^2 + L_{AB}^2 \cos^2(\theta_2 - \beta_1) - 2L_{AB}L_{HE} \cos(\theta_2 - \beta_1) + L_{HE}^2 \right]^{\frac{1}{2}} \quad (5.5)$$

where

β_1 is a constant angle $< BAC$

L_{AB} , L_{AH} and L_{HE} have constant values obtained from the manipulator's geometry.

To determine the relationship between the joint angular velocity ($\dot{\theta}_2$) to the rate in which the boom cylinder length is changing (\dot{L}_{BE}), Equation 5.5 is differentiated with respect to time to get;

$$\dot{L}_{BE} = \dot{\theta}_2 \frac{L_{AB}L_{AH} \cos(\theta_2 - \beta_1) + L_{AB}L_{HE} \sin(\theta_2 - \beta_1)}{\sqrt{[L_{AB} \sin(\theta_2 - \beta_1) + L_{AH}]^2 + [L_{AB} \cos(\theta_2 - \beta_1) - L_{HE}]^2}} \quad (5.6)$$

The rate in which the boom cylinder is changing (\dot{L}_{BE}) is equal to the piston velocity of the boom cylinder (\dot{x}_{bo}). Therefore;

$$\dot{x}_{bo} = r_{19} \dot{\theta}_2 \quad (5.7)$$

where

$$r_{19} = \frac{L_{AB}L_{AH} \cos(\theta_2 - \beta_1) + L_{AB}L_{HE} \sin(\theta_2 - \beta_1)}{\sqrt{[L_{AB} \sin(\theta_2 - \beta_1) + L_{AH}]^2 + [L_{AB} \cos(\theta_2 - \beta_1) - L_{HE}]^2}} \quad (5.8)$$

Equation 5.7 is the kinematic equation illustrating how the hydro-mechanical dynamics of the boom link are coupled. This can be represented in bond graph form as shown in Figure 5.3.

$$1:\dot{x}_{bo} \xrightarrow{F_{cy}} MTF : \frac{1}{r_{19}} \xrightarrow{\tau_2} 1:\dot{\theta}_2$$

Figure 5.3: Coupling the hydro-mechanical dynamics of the boom link

5.2.2 Arm Link

This is actuated by the arm cylinder which moves joint 3. The equation relating the length of the hydraulic cylinder L_{FI} , to the joint variable θ_3 is presented next.

Consider Figure 5.4 which is obtained from Figure 3.1.

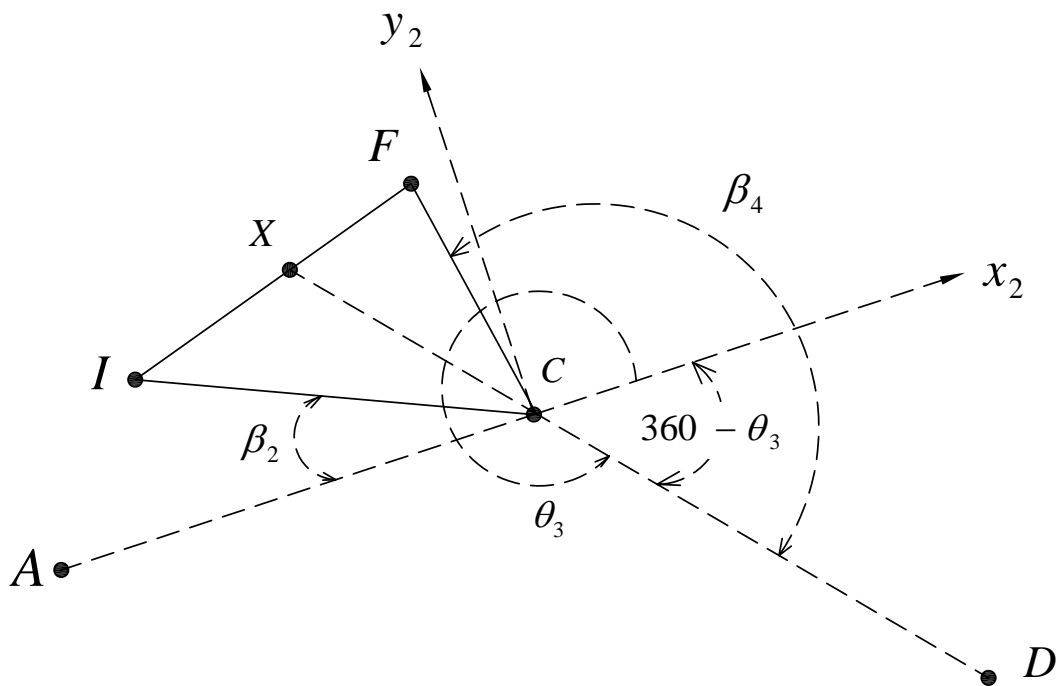


Figure 5.4: Arm cylinder length

Let $\widehat{ACI} = \beta_2$ and $\widehat{FCD} = \beta_4$, therefore;

$$\begin{aligned} \widehat{FCI} &= \widehat{XCF} + \widehat{XCI} = (180 - \beta_4) + (360 - \theta_3 - \beta_2) \\ &= 540 - \theta_3 - \beta_2 - \beta_4 \end{aligned} \quad (5.9)$$

Using cosine rule on triangle FCI we get;

$$L_{FI}^2 = L_{FC}^2 + L_{CI}^2 - 2L_{FC}L_{CI} \cos(540 - \theta_3 - \beta_2 - \beta_4) \quad (5.10)$$

from which L_{FI} is obtained as

$$L_{FI} = L_{FC} \sqrt{1 + \frac{L_{CI}^2}{L_{FC}^2} - 2 \frac{L_{CI}}{L_{FC}} \cos \left((540 - \beta_2 - \beta_4) - \theta_3 \right)} \quad (5.11)$$

To determine the relationship between the joint angular velocity ($\dot{\theta}_3$) to the rate in which the arm cylinder length is changing (\dot{L}_{FI}), Equation 5.11 is differentiated with respect to time to get;

$$\dot{L}_{FI} = \dot{\theta}_3 \frac{-L_{CI} \sin \left((540 - \beta_2 - \beta_4) - \theta_3 \right)}{\sqrt{1 + \frac{L_{CI}^2}{L_{FC}^2} - 2 \frac{L_{CI}}{L_{FC}} \cos \left((540 - \beta_2 - \beta_4) - \theta_3 \right)}} \quad (5.12)$$

The rate in which the length of arm cylinder is changing (\dot{L}_{FI}) is equal to the piston velocity of the arm cylinder (\dot{x}_a). Therefore;

$$\dot{x}_a = r_{20} \dot{\theta}_3 \quad (5.13)$$

Where

$$r_{20} = \frac{-L_{CI} \sin \left((540 - \beta_2 - \beta_4) - \theta_3 \right)}{\sqrt{1 + \frac{L_{CI}^2}{L_{FC}^2} - 2 \frac{L_{CI}}{L_{FC}} \cos \left((540 - \beta_2 - \beta_4) - \theta_3 \right)}} \quad (5.14)$$

Equation 5.13 is the kinematic equation illustrating how the hydro-mechanical dynamics of the arm link are coupled. This can be represented in bond graph form as shown in Figure 5.5.

$$1:\dot{x}_a \xrightarrow{F_{cy}} MTF : \frac{1}{r_{20}} \xrightarrow{\tau_3} 1:\dot{\theta}_3$$

Figure 5.5: Coupling the hydro-mechanical dynamics of the arm link

5.2.3 Bucket Link

This is actuated by the bucket cylinder which moves joint 4. The equation relating the length of the hydraulic cylinder L_{JK} , to the joint variable θ_4 is presented next.

Consider Figure 5.6 which is obtained from Figure 3.1.

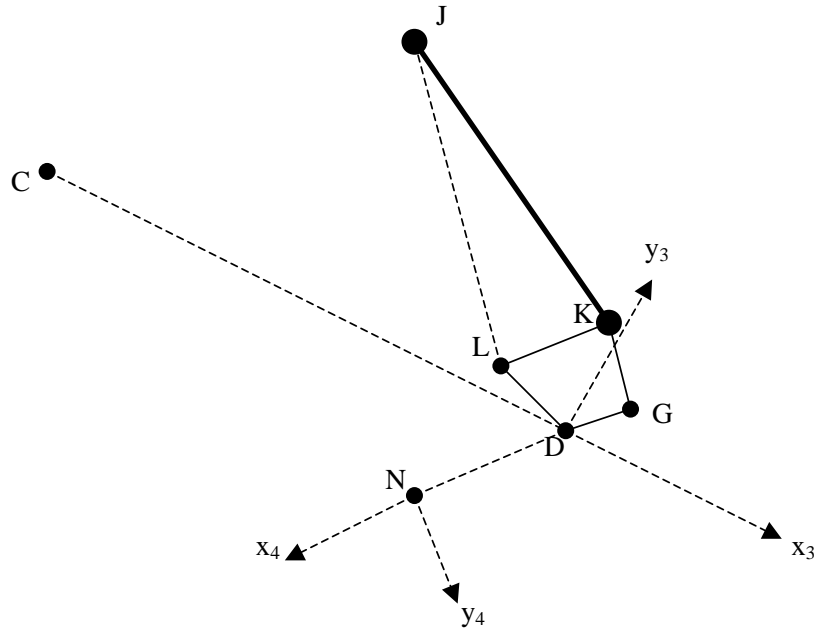


Figure 5.6: Bucket cylinder length

Applying cosine rule in triangle JKL , we get;

$$L_{JK}^2 = L_{JL}^2 + L_{KL}^2 - 2L_{JL}L_{KL} \cos(\nu_1 - \varepsilon_1) \quad (5.15)$$

where;

$\nu_1 = \angle JLD$ have constant value and can be obtained from manipulator's geometry

$\varepsilon_1 = \angle KLD$.

Summing angles along axis 4, we get;

$$\begin{aligned}\angle LDG &= \pi - \angle x_3DN - \angle CDL - \angle GDN \\ &= \pi - \theta_4 - \nu_2 - \nu_3\end{aligned}\quad (5.16)$$

Summing angles in the quadrangle $KLDG$ gives;

$$2\pi = \angle KLD + \angle KGD + \angle LDG + \angle LKG$$

By defining $\varepsilon_2 = \angle KGD$ and $\varepsilon_3 = \angle LKG$, a relation between ε_1 and θ_4 is obtained as;

$$\begin{aligned}2\pi &= \varepsilon_1 + \varepsilon_2 + (-\theta_4 + \pi - \nu_2 - \nu_3) + \varepsilon_3 \\ \theta_4 &= -\pi - \nu_2 - \nu_3 + \varepsilon_1 + \varepsilon_2 + \varepsilon_3\end{aligned}\quad (5.17)$$

From Equation 5.17, ε_1 is expressed in terms of θ_4 as;

$$\varepsilon_1 = \theta_4 + \pi + \nu_2 + \nu_3 - \varepsilon_2 - \varepsilon_3\quad (5.18)$$

Substituting Equation 5.18 in Equation 5.15 we get;

$$L_{JK}^2 = L_{JL}^2 + L_{KL}^2 - 2L_{JL}L_{KL} \cos(\nu_1 - \nu_2 - \nu_3 - \pi + \varepsilon_2 + \varepsilon_3 - \theta_4)\quad (5.19)$$

from which L_{JK} is obtained as;

$$L_{JK} = L_{JL} \left[1 + \frac{L_{KL}^2}{L_{JL}^2} - 2 \frac{L_{KL}}{L_{JL}} \cos(\nu_1 - \nu_2 - \nu_3 - \pi + \varepsilon_2 + \varepsilon_3 - \theta_4) \right]^{\frac{1}{2}}\quad (5.20)$$

To determine the relationship between the joint angular velocity ($\dot{\theta}_4$) to the rate in which the cylinder piston is changing (\dot{L}_{JK}), Equation 5.20 is differentiated with respect to time to get;

$$\dot{L}_{JK} = \dot{\theta}_4 \frac{-L_{KL} \sin(\nu_1 - \nu_2 - \nu_3 - \pi + \varepsilon_2 + \varepsilon_3 - \theta_4)}{\sqrt{1 + \frac{L_{KL}^2}{L_{JL}^2} - 2\frac{L_{KL}}{L_{JL}} \cos(\nu_1 - \nu_2 - \nu_3 - \pi + \varepsilon_2 + \varepsilon_3 - \theta_4)}} \quad (5.21)$$

The rate in which the length of bucket cylinder is changing (\dot{L}_{JK}) is to the piston velocity of the bucket cylinder (\dot{x}_{bu}). Therefore;

$$\dot{x}_{bu} = r_{21} \dot{\theta}_4 \quad (5.22)$$

Where

$$r_{21} = \frac{-L_{KL} \sin(\nu_1 - \nu_2 - \nu_3 - \pi + \varepsilon_2 + \varepsilon_3 - \theta_4)}{\sqrt{1 + \frac{L_{KL}^2}{L_{JL}^2} - 2\frac{L_{KL}}{L_{JL}} \cos(\nu_1 - \nu_2 - \nu_3 - \pi + \varepsilon_2 + \varepsilon_3 - \theta_4)}} \quad (5.23)$$

Equation 5.22 is the kinematic equation illustrating how the hydro-mechanical dynamics of the bucket link are coupled. This can be represented in bond graph form as shown in Figure 5.7.

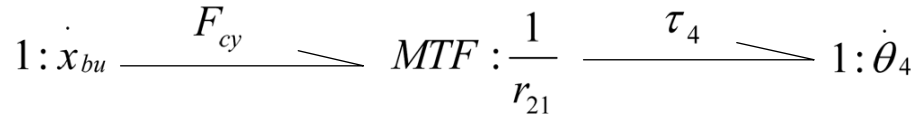


Figure 5.7: Coupling the hydro-mechanical dynamics of the bucket link

5.3 Overall Bond Graph Model of the Hydraulic and Mechanical Dynamics

Figure 5.8 shows the overall non-causal bond graph model representing the interaction of mechanical and hydraulic dynamics of the excavator.

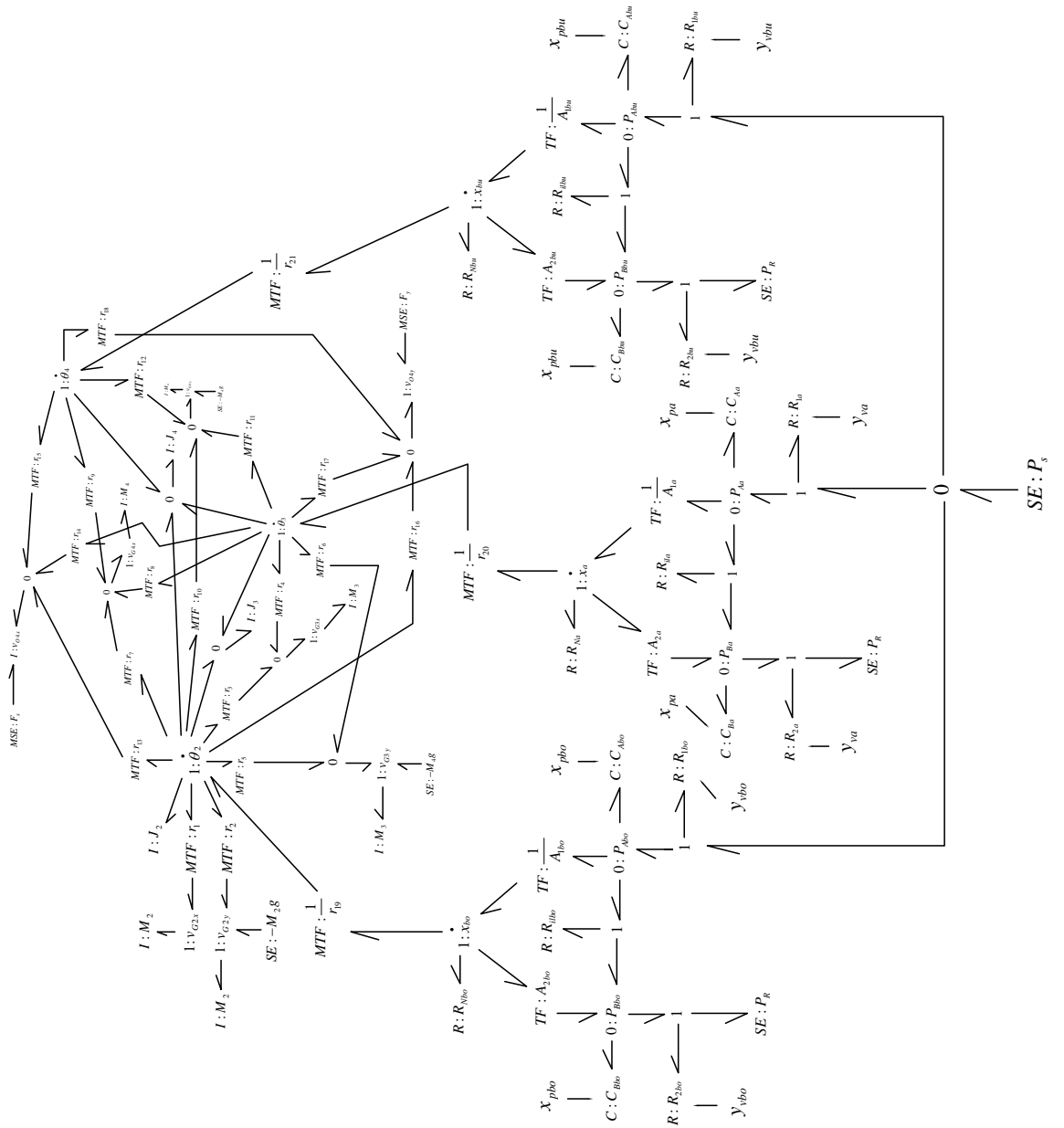


Figure 5.8: Non-causal bond graph model of the excavating mechanism

Assigning causality to the non causal bond graph model shown in Figure 5.8, led to derivative causality for both the vertical and horizontal momenta of the boom, arm and bucket links. This means that the assumptions made in constructing this model have led to a model that will not compute easily with a computer. This is not

a fault of bond graphs, but would be true regardless of one's approach to modeling subject to the same assumptions.

To fix this derivative causality problem easily, the 'Karnopp-Margolis' method [26] of appending very stiff springs and dampers at the pin joints of the manipulator links was used. These are pointed out in Figure 5.9. This allowed a causal bond graph to result with straight-forward simulation properties, that is, integral causality in all the capacitive and inertial elements of the bond graph model. In practice, these additional elements are selected to produce frequencies well outside the range of interest. In this case, elements were chosen to produce $200Hz$ frequencies since we are interested in frequencies no higher than $20Hz$ and no modal dynamics have been included for any of the mechanical or fluid parts of the system.

At this point, we have a causal bond graph model of the excavating manipulator given in Figure 5.9. This model would predict the motion-time history of the system for any inputs y to the cylinder valves actuating the manipulator links.

CHAPTER 6

SYSTEM ANALYSIS AND DESIGN USING INVERSE DYNAMICS

6.1 Introduction

In inverse dynamics, the generalized joint torques are computed given the desired joint trajectories. The desired joint trajectories are obtained through the trajectory planning schemes which generally interpolate or approximate the desired manipulator path by a class of polynomial functions and generates a sequence of time-based set-points for the manipulator from the initial position and orientation to its destination [16]. Two cases are considered, that is, when the manipulator is moving in a free space, and when the bucket is digging a sandy-loam soil. As described in [10], all the cylinders are considered to be extending during the digging operation.

6.2 Parameter Identification

In the previous chapters, a dynamic bond graph model representing the hydro-mechanical dynamics of the system was developed. However good mathematical models depend not only on the structure of the equations, but also on the values of physical parameters involved. Therefore parameter identification can be considered as part of the process of constructing valid mathematical and graphical models for dynamic systems.

Parameters like lengths, masses and angles were found from design drawings and trigonometric calculations. But parameters like the location of a center of mass, link moments of inertia, products of inertia of a link could not be estimated from blueprints. Fortunately, solid modeling techniques can be used to determine the location of mass centers, moments and products of inertia very accurately. Auto CAD

with Advanced Modeling Extension Package was used to estimate mass properties of all the links and the locations of center of masses.

The cylinder and hydraulic initial design parameters are given given in Tables 4.1 and 4.2 respectively. The initial design parameters for the boom, bucket and arm links are given in Tables 6.1, 6.2 and 6.3 respectively.

6.2.1 Boom Link Parameters

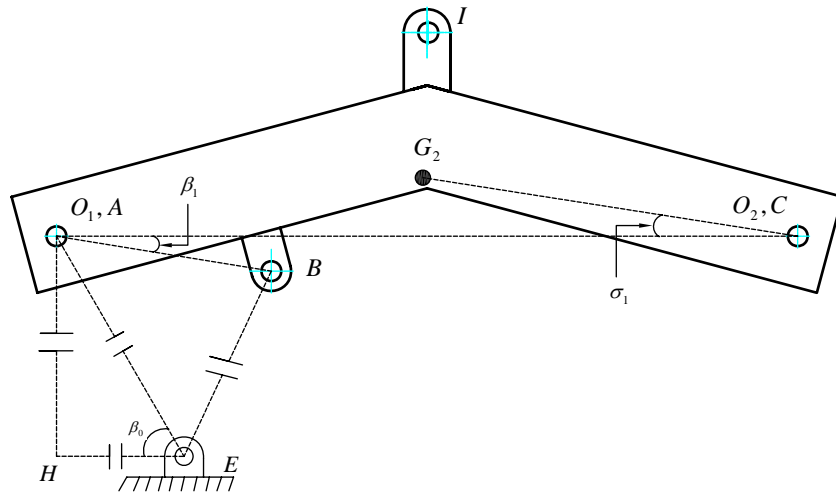


Figure 6.1: Schematic diagram of the boom link

Table 6.1: Boom link geometric parameters

Parameter description		Units	Value
Length from O_1 to O_2 ,	$L_{O_1O_2}$	mm	1160
Length from G_2 to O_2 ,	$L_{G_2O_2}$	mm	566.5
Length from H to E ,	L_{HE}	mm	75
Length from A to B ,	L_{AB}	mm	328.97
Length from A to H ,	L_{AH}	mm	823.3
Length from A to E ,	L_{AE}	mm	856.7
Angle $\angle AEH$,	β_0	deg($^\circ$)	84.8
Angle $\angle BAC$,	β_1	deg($^\circ$)	9.23
Angle $\angle G_2O_2O_1$,	σ_1	deg($^\circ$)	8.87
Mass of the link,	M_2	Kg	14.66
Mass inertia about the centroid,	J_2	Kg/m ²	1.55

6.2.2 Bucket Link Parameters

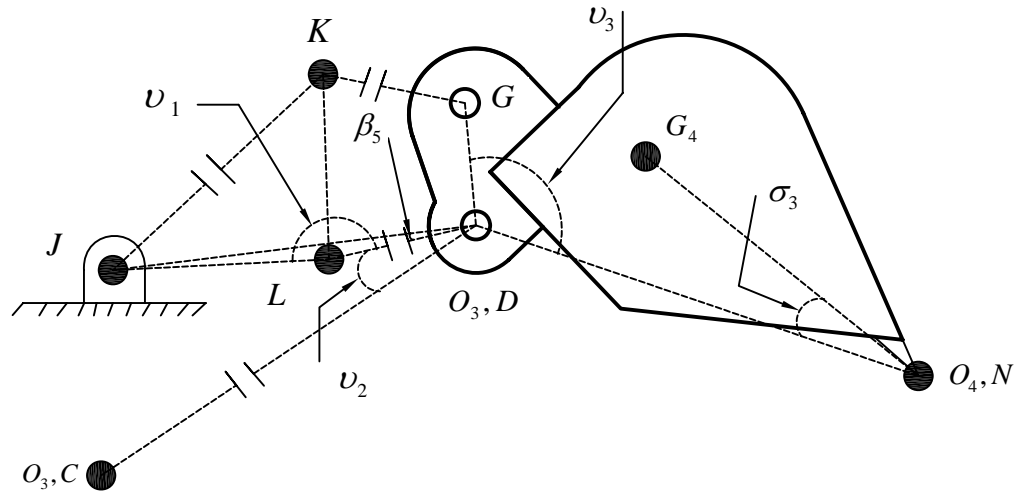


Figure 6.2: Schematic diagram of the bucket link

Table 6.2: Bucket link geometric parameters

Parameter description		Units	Value
Length from O_3 to O_4 ,	$L_{O_3O_4}$	mm	570
Length from G_4 to O_4 ,	$L_{G_4O_4}$	mm	475.68
Length from K to G ,	L_{KG}	mm	141
Length from D to L ,	L_{DL}	mm	100
Length from G to D ,	L_{GD}	mm	130
Length from K to L ,	L_{KL}	mm	147
Length from J to L ,	L_{JL}	mm	683.06
Angle $\angle JLD$,	ν_1	deg($^\circ$)	176.22
Angle $\angle CDL$,	ν_2	deg($^\circ$)	5.71
Angle $\angle GDN$,	ν_3	deg($^\circ$)	47.67
Angle $\angle JDL$,	β_5	deg($^\circ$)	3.295
Angle $\angle G_4O_4O_3$,	σ_3	deg($^\circ$)	17.69
Mass of the link,	M_4	Kg	15.37
Mass inertia about the centroid,	J_4	Kg / m 2	1.43

6.2.3 Arm Link Parameters

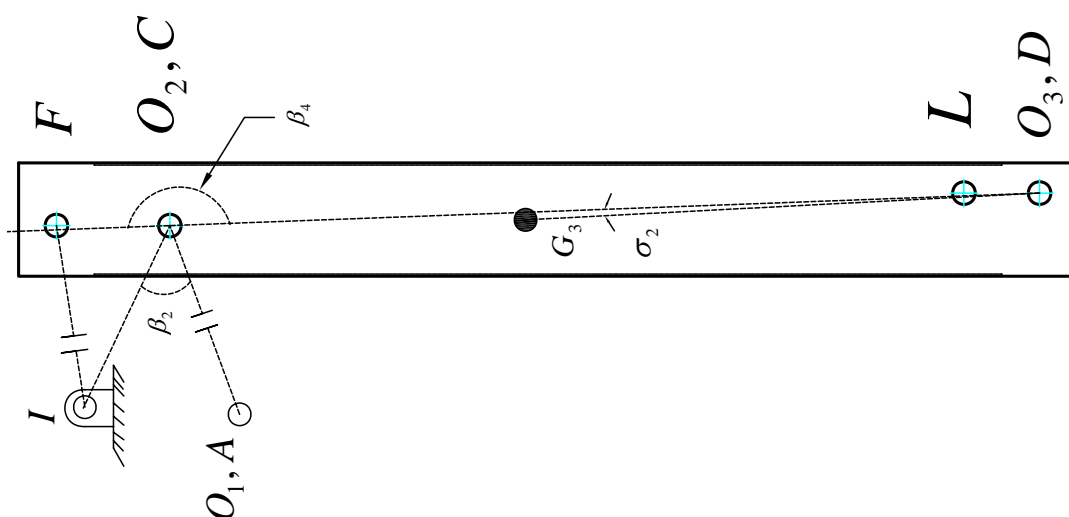


Figure 6.3: Schematic diagram of the arm link

Table 6.3: Arm link geometric parameters

Parameter description		Units	Value
Length from O_2 to O_3 ,	$L_{O_2O_3}$	<i>mm</i>	1102.55
Length from G_3 to O_3 ,	$L_{G_3O_3}$	<i>mm</i>	654.43
Length from F to C ,	L_{FC}	<i>mm</i>	200
Length from C to I ,	L_{CI}	<i>mm</i>	637.53
Angle $\angle ACI$,	β_2	deg($^\circ$)	28.86
Angle $\angle FCD$,	β_4	deg($^\circ$)	174.29
Angle $\angle G_3O_3O_2$,	σ_2	deg($^\circ$)	2.68
Mass of the link,	M_3	<i>Kg</i>	13.92
Mass inertia about the centroid,	J_3	<i>Kg / m²</i>	1.0109

6.3 Trajectory Planning

In a typical trajectory, all joints move simultaneously. For the typical trajectory selected here, the boom, arm, and bucket links move from their minimum to maximum positions and all joints start and finish moving at the same time, although different time limits can be programmed.

Three common trajectories namely, trapezoidal trajectory, cubic polynomial trajectory, and quintic polynomial trajectory have been previously applied in trajectory planning for hydraulic manipulators. Sarkar [44] used the three trajectories to size the valves and power requirement for an articulated forestry machine. Among the three methods, the quintic polynomial trajectory has advantage in that;

- the velocity trajectory is smooth unlike in trapezoidal trajectory whose velocity profile has discontinuities where the link motion starts to settle at a constant velocity, and where the link starts to decelerate.

- the acceleration profile has values equal to zero at starting and finishing times of the trajectory, unlike in the other trajectories where the acceleration values at the start and final times have non zero values.

Therefore the trajectory to be adopted in this work is the quintic polynomial trajectory which is given by;

$$x(t) = a_0 + a_1t + a_2t^2 + a_3t^3 + a_4t^4 + a_5t^5 \quad (6.1)$$

The desired boundary conditions are;

$$x_{t=0} = x_{min} \quad (6.2)$$

$$x_{t=t_f} = x_{max} \quad (6.3)$$

$$\dot{x}_{t=0} = 0 \quad (6.4)$$

$$\dot{x}_{t=t_f} = 0 \quad (6.5)$$

$$\ddot{x}_{t=0} = 0 \quad (6.6)$$

$$\ddot{x}_{t=t_f} = 0 \quad (6.7)$$

By taking the first and second derivatives of Equation 6.1 and satisfying the boundary conditions the coefficients of the polynomial are obtained as;

$$a_1 = 0 \quad (6.8)$$

$$a_2 = 0 \quad (6.9)$$

$$a_3 = \frac{10(x_{max} - x_{min})}{t_f^3} \quad (6.10)$$

$$a_4 = \frac{15(x_{min} - x_{max})}{t_f^4} \quad (6.11)$$

$$a_5 = \frac{6(x_{max} - x_{min})}{t_f^5} \quad (6.12)$$

Substituting the coefficients in the polynomial Equation 6.1 and its first and second time derivative, we get the required displacement, velocity and acceleration trajectories as;

$$x(t) = x_{min} + \frac{10(x_{max} - x_{min})}{t_f^3}t^3 + \frac{15(x_{min} - x_{max})}{t_f^4}t^4 + \frac{6(x_{max} - x_{min})}{t_f^5}t^5 \quad (6.13)$$

$$\dot{x}(t) = \frac{30(x_{max} - x_{min})}{t_f^3}t^2 + \frac{60(x_{min} - x_{max})}{t_f^4}t^3 + \frac{30(x_{max} - x_{min})}{t_f^5}t^4 \quad (6.14)$$

$$\ddot{x}(t) = \frac{60(x_{max} - x_{min})}{t_f^3}t + \frac{180(x_{min} - x_{max})}{t_f^4}t^2 + \frac{120(x_{max} - x_{min})}{t_f^5}t^3 \quad (6.15)$$

Equations 6.13, 6.14 and 6.15 can be applied to the boom, arm and bucket links to obtain their displacement, velocity and acceleration quintic polynomial trajectories as shown in Figures 6.4, 6.5 and 6.6 respectively for case ERR as illustrated in section 6.5.

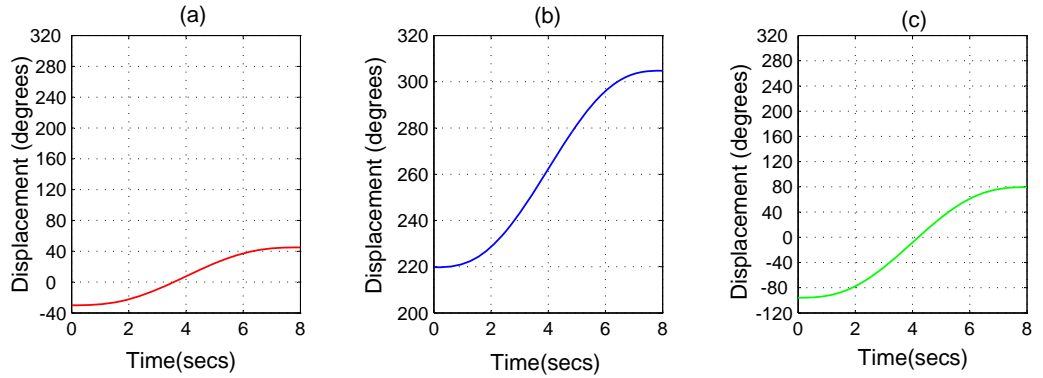


Figure 6.4: **(a)** Boom link's angular displacement trajectory **(b)** Arm link's angular displacement trajectory **(c)** Bucket link's angular displacement trajectory

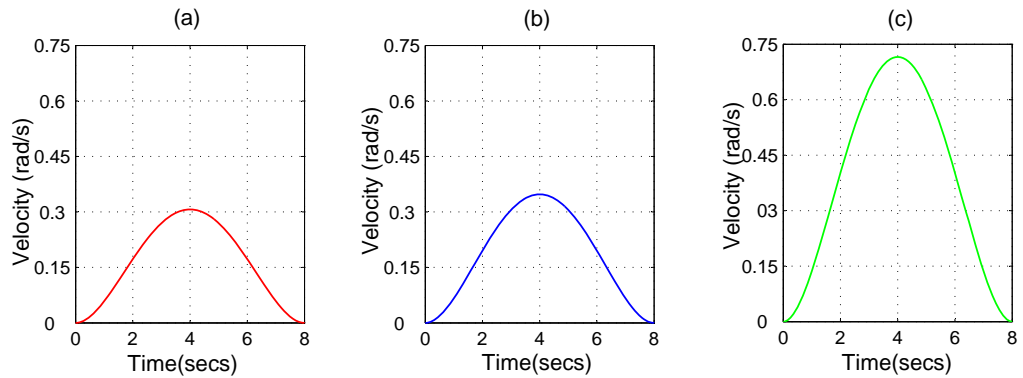


Figure 6.5: **(a)** Boom link’s angular velocity trajectory **(b)** Arm link’s angular velocity trajectory **(c)** Bucket link’s angular velocity trajectory

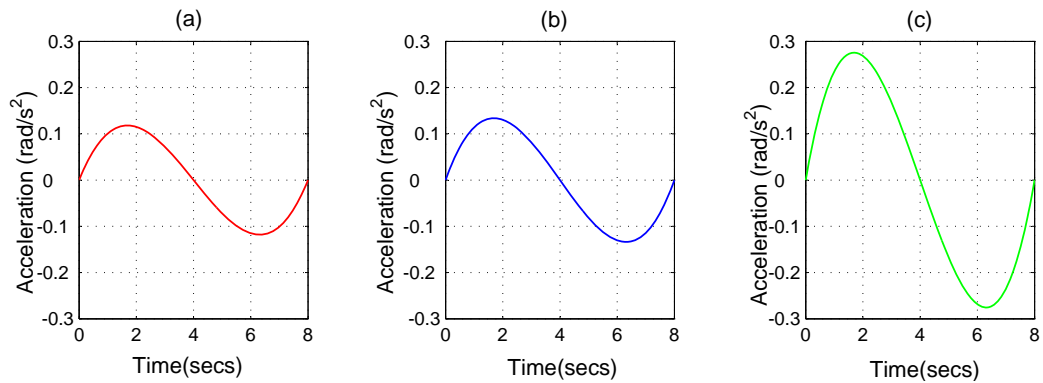


Figure 6.6: **(a)** Boom link’s angular acceleration trajectory **(b)** Arm link’s angular acceleration trajectory **(c)** Bucket link’s angular acceleration trajectory

6.4 Simulink Model for the Inverse Dynamics of the 3 DOF System

Figure 6.7 shows the complete Simulink model of the inverse dynamics of 3dof excavating manipulator. This model is the test-bed for all inverse dynamics simulations done on the system. The whole system is run in the same time frame, and as a result the outputs must match the generated trajectories.

The *joint trajectory generator block* produces the desired boom, arm and bucket

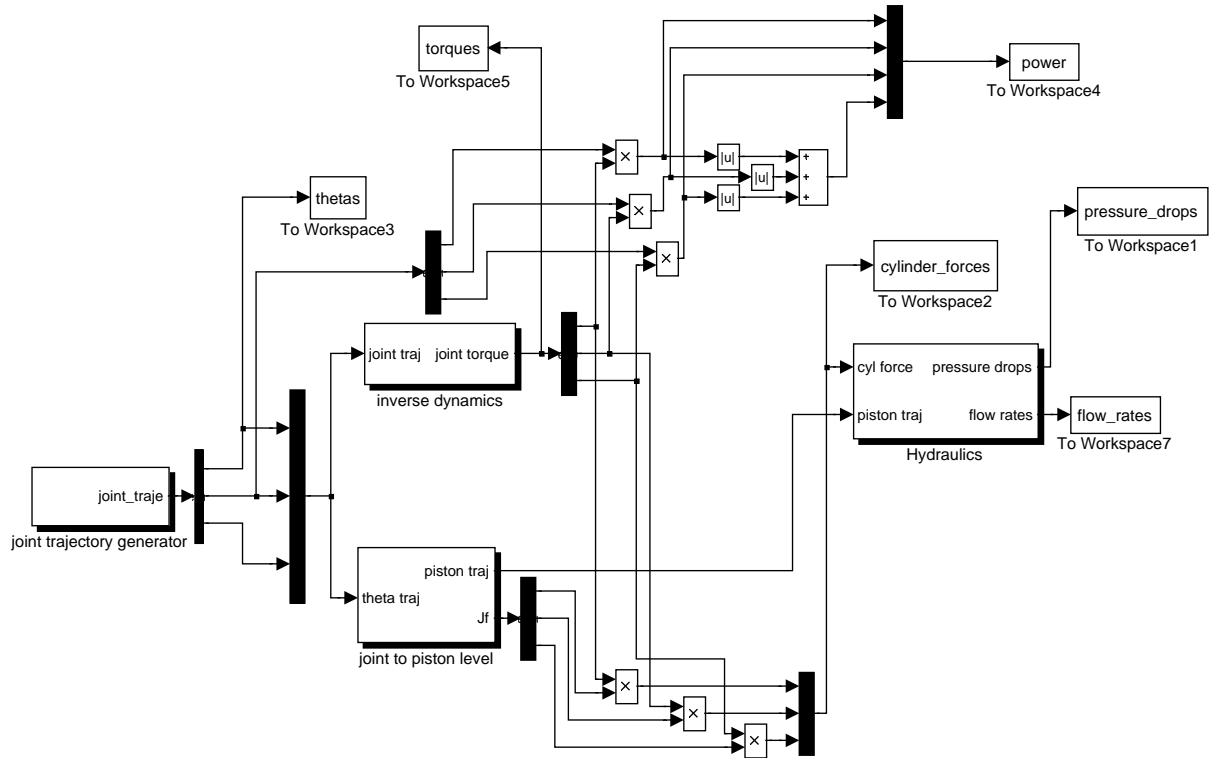


Figure 6.7: The overall Simulink block for the inverse dynamics

quintic polynomial trajectories, that is, the angular displacements, angular velocities and angular accelerations of the links which are shown in Figures 6.4, 6.5 and 6.6. The three signals from the *joint trajectory generator block* each containing the corresponding signals for the boom, arm and bucket link are fed into the *inverse dynamics block* shown in Figure 6.8 to compute the joint torques using Equations 6.16, 6.17 and 6.18 for the bucket, arm and boom links respectively.

As seen in Equations 6.16, 6.17 and 6.18, the joint torques depend on the modulated transformer ratios (r_1 to r_{12}) and the centroid velocities of the links (v_{G2x} , v_{G2y} , v_{G3x} , v_{G3y} , v_{G4x} and v_{G4y}). Also the centroid velocities depend on the modulated transformer ratios and the joint angular velocities of the links as illustrated in section

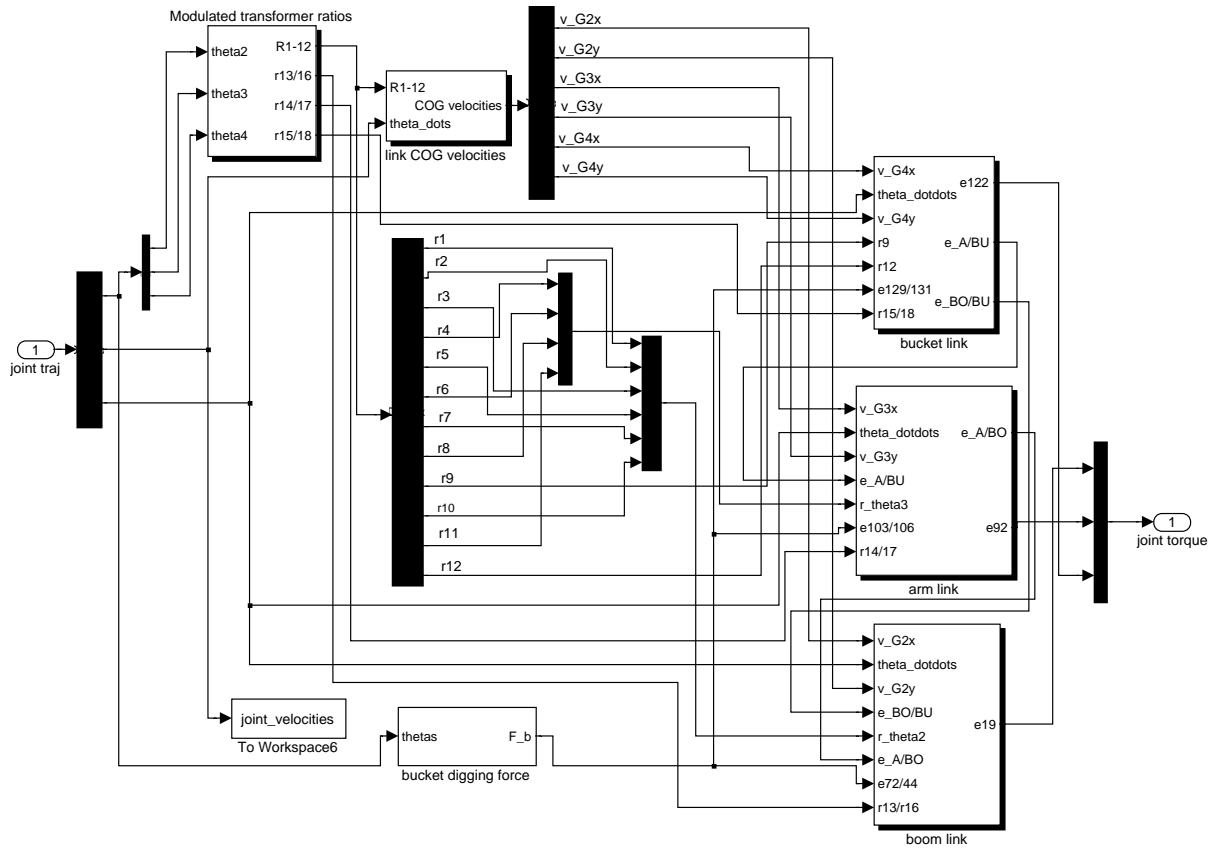


Figure 6.8: The Simulink block for computing the joint torques using inverse dynamics

3.1.2. The ratios are computed in the *modulated transformer ratio block*.

The outputs from the *modulated transformer ratios block* are input to the *Link COG block* for purposes of computing the centroid velocities of the links, which together with the ratios are input into the *Boom link block*, *Arm link block* and *Bucket link block* to determine the joint torque for the corresponding link. This is shown in Figure 6.8.

Also the output from the *joint trajectory generator block* is fed to the *joint to piston level block* as shown in Figure 6.7 where the joint trajectories are converted to

actuator piston trajectories using the relationships in Equations 5.5, 5.6, 5.11, 5.12, 5.20, and 5.21.

6.5 Torque Profiles

From the bond graph model represented in Figure 3.12 inverse dynamics can be performed on the manipulator to compute the torque-time history applied at the three joints of the system in order to accomplish the quintic polynomial trajectory planned for the three links. The torque equations obtained from the bond graph model are;

Bucket link

$$\tau_{bu} = J_4(\ddot{\theta}_2 + \ddot{\theta}_3 + \ddot{\theta}_4) + r_{12} \left(M_4 \frac{d(v_{G4y})}{dt} + M_4 g \right) + r_9 M_4 \frac{d(v_{G4x})}{dt} \quad (6.16)$$

Arm link

$$\begin{aligned} \tau_a = & J_3(\ddot{\theta}_2 + \ddot{\theta}_3) + J_4(\ddot{\theta}_2 + \ddot{\theta}_3 + \ddot{\theta}_4) + r_6 \left(M_3 \frac{d(v_{G3y})}{dt} + M_3 g \right) + r_4 M_3 \frac{d(v_{G3x})}{dt} \\ & + r_8 M_4 \frac{d(v_{G4x})}{dt} + r_{11} \left(M_4 \frac{d(v_{G4y})}{dt} + M_4 g \right) \end{aligned} \quad (6.17)$$

Boom link

$$\begin{aligned} \tau_a = & J_2 \ddot{\theta}_2 + J_3(\ddot{\theta}_2 + \ddot{\theta}_3) + J_4(\ddot{\theta}_2 + \ddot{\theta}_3 + \ddot{\theta}_4) + r_5 \left(M_3 \frac{d(v_{G3y})}{dt} + M_3 g \right) + r_3 M_3 \frac{d(v_{G3x})}{dt} \\ & + r_7 M_4 \frac{d(v_{G4x})}{dt} + r_{10} \left(M_4 \frac{d(v_{G4y})}{dt} + M_4 g \right) + r_1 M_2 \frac{d(v_{G2x})}{dt} \\ & + r_2 \left(M_2 \frac{d(v_{G2y})}{dt} + M_2 g \right) \end{aligned} \quad (6.18)$$

Where all the parameters are as defined in section 3.1. Since all the time histories of the joint variables, that is, the joint displacements, the joint velocities, and the joint accelerations are known from the trajectory planning, Equations 6.16, 6.17 and

6.18 can be utilized to compute the applied torques as a function of time which are required to produce the particular planned manipulator motion.

Table 6.4 shows the eight (8) possible cases of the manipulator link motions which were considered so as to determine which case gives the critical torque profile when the manipulator is moving in free space.

Table 6.4: Manipulator motion cases

Case	Boom cylinder	Arm cylinder	Bucket cylinder
Case EEE	Extending	Extending	Extending
Case EER	Extending	Extending	Retracting
Case ERE	Extending	Retracting	Extending
Case REE	Retracting	Extending	Extending
Case ERR	Extending	Retracting	Retracting
Case RER	Retracting	Extending	Retracting
Case RRE	Retracting	Retracting	Extending
Case RRR	Retracting	Retracting	Retracting

The joint torque profiles required to accomplish the trajectories planned for the eight cases of the manipulator motion as shown in Table 6.4, were simulated and the ERR and REE cases were found to give the same highest values of the torques for all the link joints as depicted in Figures 6.9 and 6.10.

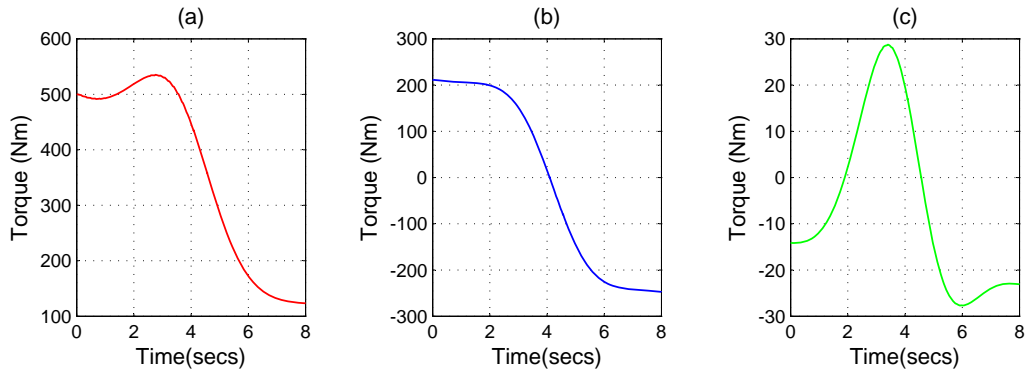


Figure 6.9: The torque profiles at joints, when the manipulator is moving in a free space and for REE case; **(a)** Boom joint torque **(b)** Arm joint torque **(c)** Bucket joint torque

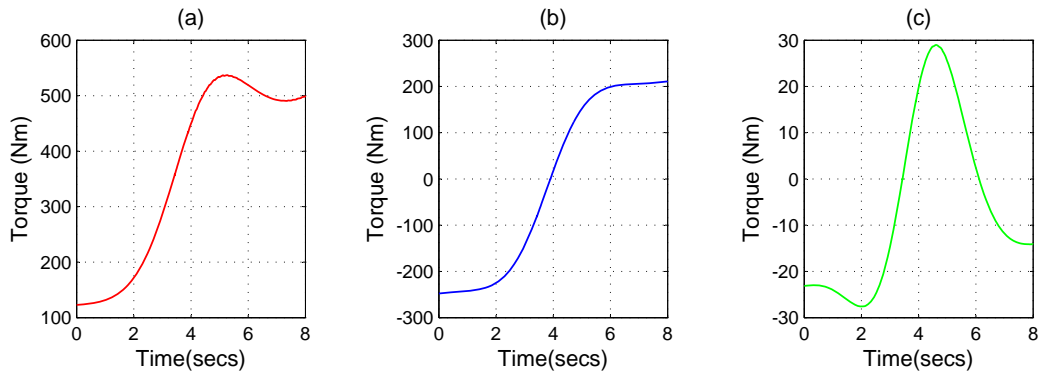


Figure 6.10: The torque profiles at joints, when the manipulator is moving in a free space and for ERR case; **(a)** Boom joint torque **(b)** Arm joint torque **(c)** Bucket joint torque

By observing the nature of the torque profiles, it is seen that,

- The values for the boom torque are the largest followed by those for the arm. This is attributed to the fact that the boom supports the arm which subsequently supports the bucket, therefore the torque which is needed to move the boom link is logically the largest.

- Unlike for the arm and bucket, the boom torque does not move from positive to negative. This is due to the configuration of the boom and the joint limits, that is, there is no instant during the manipulator motion when the boom link takes a vertical position. This is contrary to the arm and bucket links which during manipulator motion, they can both take a vertical position hence making the direction of motion of the links to change relative to gravity.

For the REE case, all the links are at their highest positions at the start of the manipulator motion. Due to this the gravitational effects of the arm and bucket links to the boom link and also the gravitational effect of the bucket link to the arm link are high, therefore large torques are required to initiate motions of the boom and arm links. As motion kicks off, the torques on the boom and arm decreases because the motions of the links are assisted by the gravity. At the end of the manipulator motion, the links take the position and orientation which is the initial orientation for the ERR case, therefore the reverse of what happens in REE case is true for the ERR case.

In conclusion therefore, the cases which lead to highest joint torque requirements are the REE and ERR, and the choice of any of the two cases will reflect the critical condition of the manipulator motion under no loading condition. For the analysis we decide to use the case ERR, and therefore the proceeding profiles represent the case ERR, unless mentioned otherwise.

The joint torque profiles when the bucket is digging a sandy-loam soil is shown in Figure 6.11.

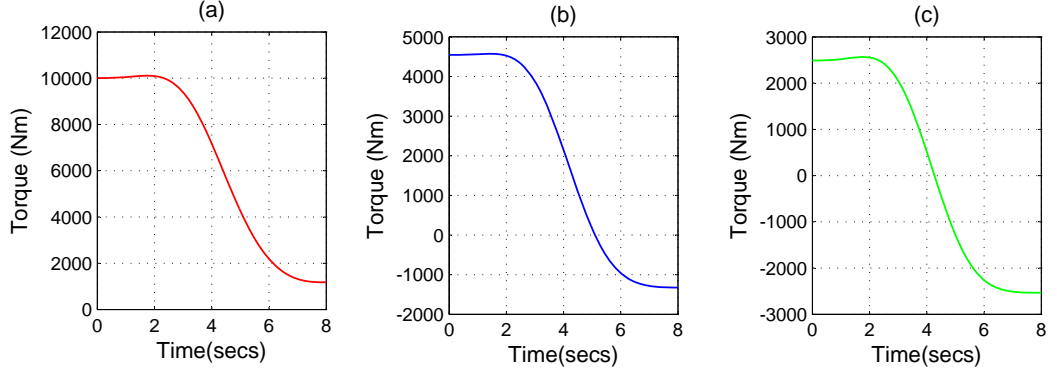


Figure 6.11: The torque profiles at manipulator joints, when the bucket is digging a sandy-loam soil; (a) Boom joint torque (b) Arm joint torque (c) Bucket joint torque

6.6 Power Profiles

The dynamic model obtained also permits either sizing of the system power supply or checking whether the desired manipulator trajectory can be followed without exceeding the power capacity of the supply. The power required for the boom, arm and bucket motion is respectively given as;

$$P_{bo} = \tau_{bo}\dot{\theta}_2 \quad (6.19)$$

$$P_a = \tau_a\dot{\theta}_3 \quad (6.20)$$

$$P_{bu} = \tau_{bu}\dot{\theta}_4 \quad (6.21)$$

Where τ is the torque required to move a link at an angular velocity of $\dot{\theta}$. The total power required for a given trajectory can be obtained by;

$$P_{total} = |P_{bo}| + |P_a| + |P_{bu}| \quad (6.22)$$

assuming there are no power losses. The power requirement profiles for the manipulator are given in Figures 6.12 and 6.13 for the two cases.

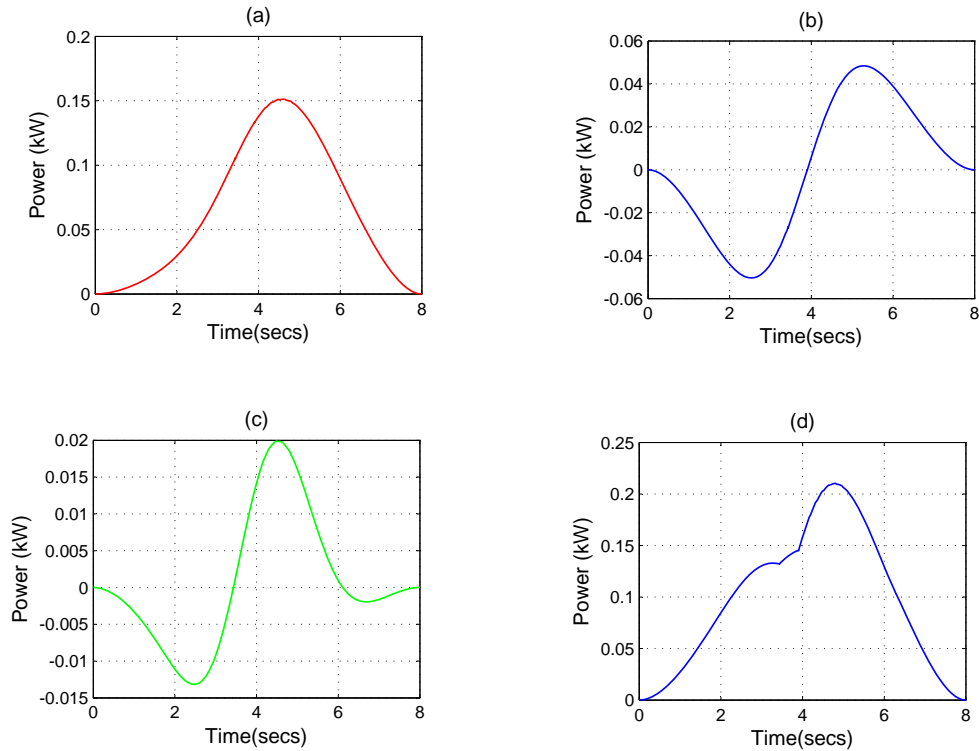


Figure 6.12: **(a)** Boom joint power **(b)** Arm joint power **(c)** Bucket joint power **(d)** Total joints power ;when the manipulator is moving in free space and at the initial cycle times

It is clear that when the manipulator is moving in a free space, the total power consumption is much lower than when the bucket of the manipulator is digging a sandy-loam soil. The peak value for the total power consumption when the bucket is digging a sandy-loam soil is shown to be approximately $5kW$ ($6.7hp$). This value is greater than the power rating of the engine ($6.5hp$) which is to drive the hydraulic pump, implying that, the digging operation cannot be achieved under the given link trajectories without exceeding the power capacity of the prime mover.

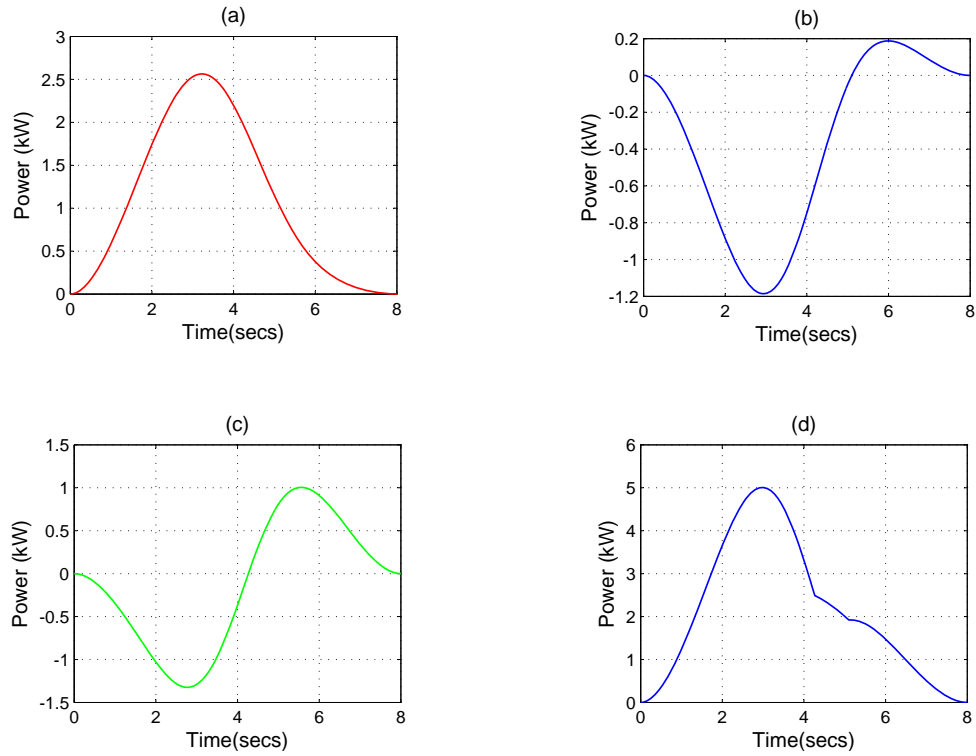


Figure 6.13: (a) Boom joint power (b) Arm joint power (c) Bucket joint power
 (d) Total joints power ;when the bucket is digging a sandy-loom soil
 and at the initial cycle times

The power consumption as seen in Equations 6.19 through 6.22 depends on the joint torque requirements and the angular velocities of the links. Two options are available to reduce the total power requirement of the manipulator. These are;

- Reduce the joint torque requirements for the manipulator, by reducing the mass properties of the links and/or reducing the force exerted to the ground by the bucket.
- Increase the cycle times of the link trajectories. This means that the pump flow rate capacity will be reduced.

In this work, the second option of increasing the cycle times of the link trajectories was used. Generally, the cycle time has a direct impact on the flow rate requirements relative to the link/actuator motion requirements, and on the power requirement of the manipulator. As seen in Equation 6.14 increasing the cycle time t_f will decrease the link velocities, and this will subsequently reduce the power requirement and also the flow rates requirement.

The optimum cycle time necessary to ensure that the power requirement for the manipulator motion when the bucket is digging a sandy-loam soil is reduced was found to be 10s. Figure 6.14 shows the new power requirement profiles for the manipulator.

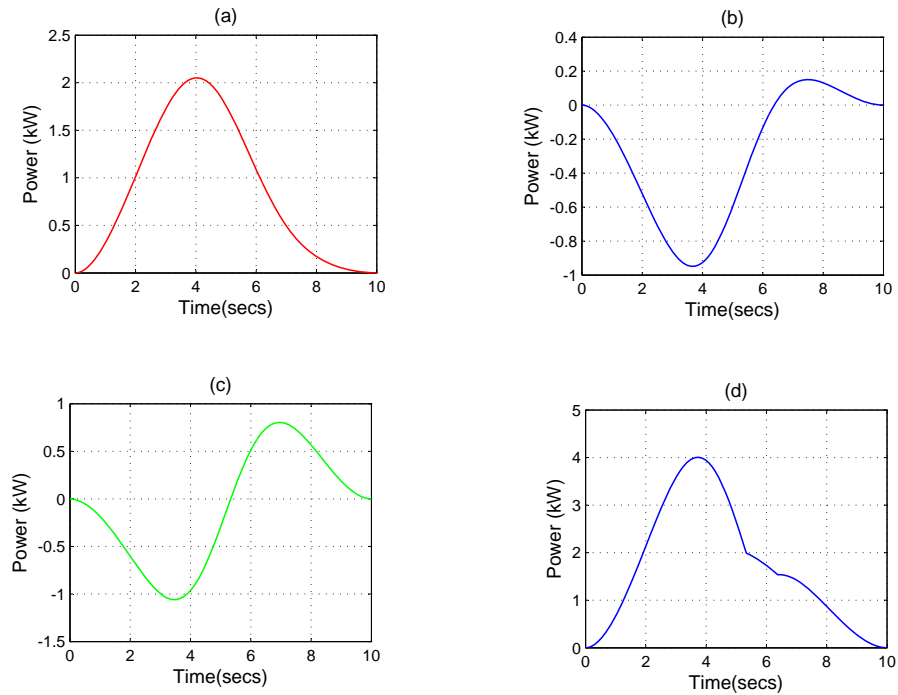


Figure 6.14: **(a)** Boom joint power **(b)** Arm joint power **(c)** Bucket joint power **(d)** Total joints power ;when the manipulator is digging a sandy-loam soil and at the optimal cycle times

6.7 Force Profiles

From the inverse dynamics and in section 6.5, we have obtained the critical torque profiles of the link motions when the manipulator is moving in free space as shown in Figure 6.10, and also the torque profiles when the bucket of the excavator is digging a sandy-loam soil as shown in Figure 6.11. Since the links of the manipulator are driven by hydraulic actuators, we need a mapping from joint torque to cylinder force using manipulator jacobians in Equations 5.8, 5.14 and 5.23. The force profiles for the boom, arm and bucket cylinders for the two cases are plotted in Figures 6.15 and 6.16.

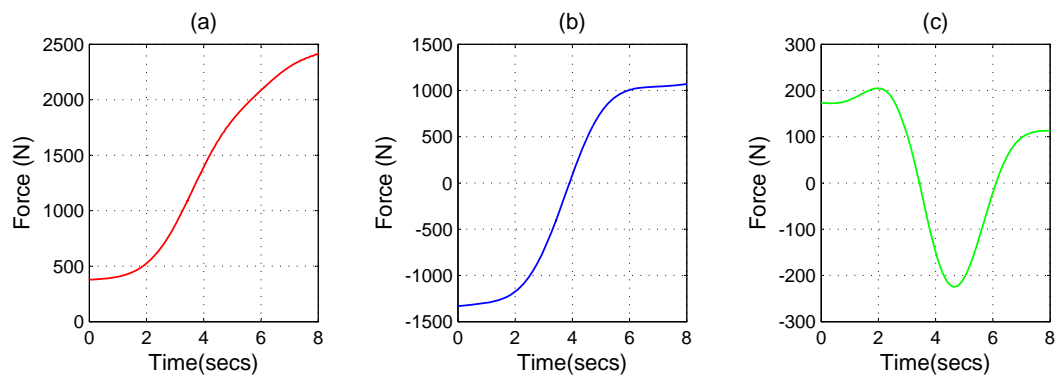


Figure 6.15: (a) Boom cylinder force profile (b) Arm cylinder force profile (c) Bucket cylinder force profile; when the manipulator is moving in a free space

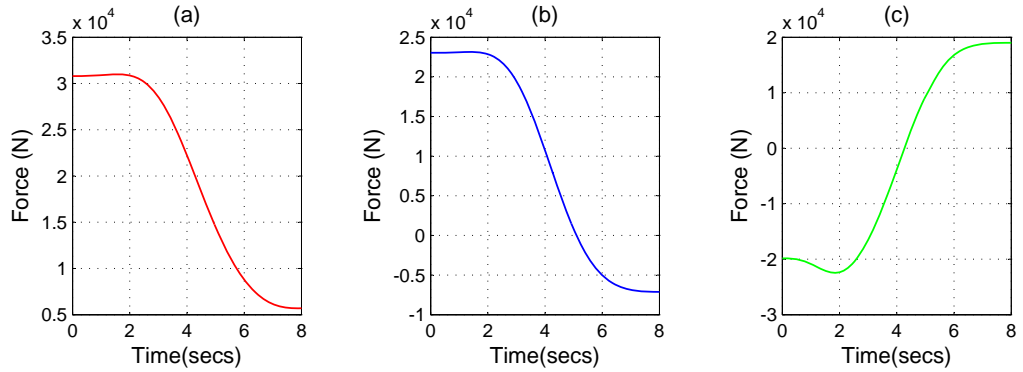


Figure 6.16: (a) Boom cylinder force profile (b) Arm cylinder force profile (c) Bucket cylinder force profile; when the bucket is digging a sandy-loam soil

The reason why the arm and bucket force profiles move from positive to negative is because the forces are related to the corresponding torques by the manipulator jacobians. As illustrated in section 6.5, the torque profiles for the arm and bucket links move from positive to negative.

6.8 Sizing the Hydraulic Actuators and Valves Based on Inverse Dynamics

An important application of the inverse dynamic modeling of hydro-mechanical systems is the sizing of hydraulic components. In this section, the optimal sizes of the actuator pistons as well as the optimal sizes of the spool valve orifice ports of the boom, arm, and bucket cylinders will be determined. For this purpose, the pressure drop profiles across the cylinders and valves need to be plotted from the inverse dynamics.

6.8.1 Pressure Drop Profiles

The hydraulic forces required to produce the torques necessary for manipulator motion results in corresponding pressure drops across the hydraulic cylinders. The expressions for the pressure drop in the boom cylinder, Δp_{bo} , arm cylinder, Δp_a , and bucket cylinder, Δp_{bu} are approximated using equations below;

$$\Delta p_{bo} = \frac{F_{cybo}}{A_{pbo}} \quad (6.23)$$

$$\Delta p_a = \frac{F_{cya}}{A_{pa}} \quad (6.24)$$

$$\Delta p_{bu} = \frac{F_{cybu}}{A_{pbu}} \quad (6.25)$$

As shown in Equations 6.23, 6.24 and 6.25, the pressure drop across a given cylinder is directly proportional to the hydraulic force of the corresponding cylinder. Therefore, the nature of the pressure drop curve is the same with the hydraulic force profile of the corresponding cylinder as shown in Figure 6.17 for the case when the bucket is digging a sandy-loam soil.

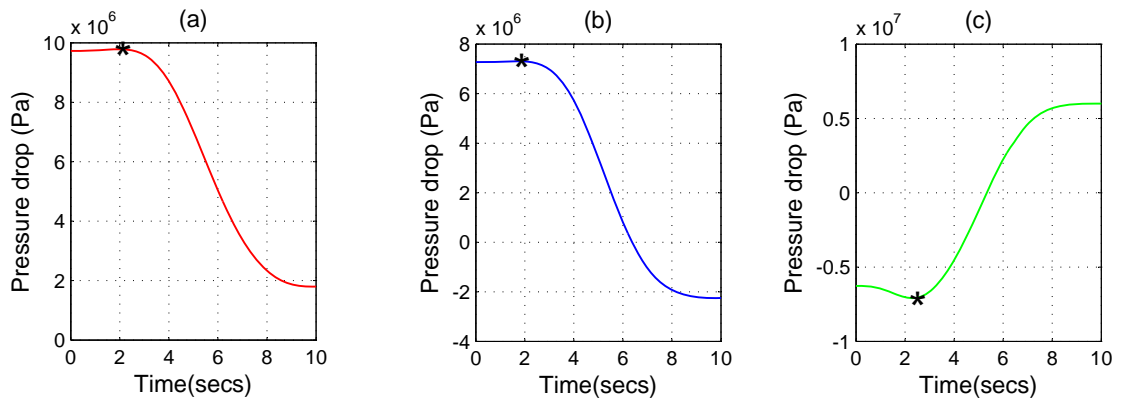


Figure 6.17: The Pressure drop profiles across the cylinders, when the bucket is digging a sandy-loam soil and at original piston diameters; (a) Boom cylinder (b) Arm cylinder (c) Bucket cylinder

Neglecting line pressure drops, the pressure drops at the corresponding valves are approximated as;

$$\Delta p_{bo_v} = p_s - |\Delta p_{bo}| \quad (6.26)$$

$$\Delta p_{av} = p_s - |\Delta p_a| \quad (6.27)$$

$$\Delta p_{bu_v} = p_s - |\Delta p_{bu}| \quad (6.28)$$

Where p_s is the operating pressure. The pressure drop profiles at the valves for the case when the bucket is digging a sandy-loam soil is shown in Figure 6.18.

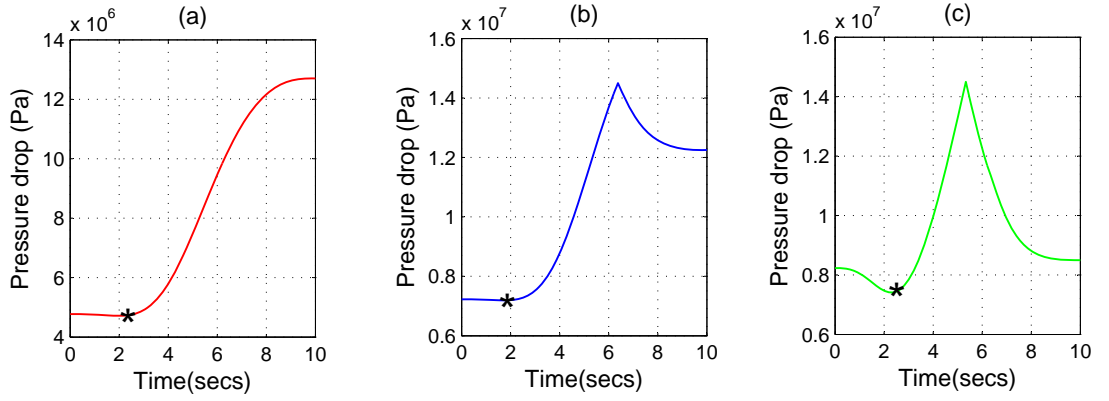


Figure 6.18: The Pressure drop profiles across the cylinder valves, when the bucket is digging a sandy-loam soil and at optimal piston diameters;
 (a) Boom cylinder valve (b) Arm cylinder valve (c) Bucket cylinder valve

6.8.2 Actuator Sizing

As shown in Equations 6.23 through 6.25 the cross sectional area of the piston of a cylinder determines the pressure drop across the cylinder during the working stroke, which is considered to be the extension stroke. And from Equations 6.26 through 6.28 the maximum possible pressure drop (Δp_{max}) across a given cylinder should be equal to the supply pressure (p_s), that is,

$$\Delta p_{max} = p_s \quad (6.29)$$

- If $\Delta p_{max} < p_s$, then this implies that the supply pressure is not used maximally and hence there is no need of such a high pump pressure since the cylinder is oversized.
- If $\Delta p_{max} > p_s$, then the pressure drop across the valve becomes negative and this will result to a negative flow rate through the valve. This is not possible practically and implies that the cylinder is undersized.

The critical case to be considered in sizing the hydraulic cylinders is when the bucket is exerting a digging force to the ground. As seen in Figure 6.17, the maximum pressure drops across the cylinders (points with asterisks) are less than the supply pressure of $p_s = 14.5MPa$. This is also shown in Figure 6.18 where at the point of maximum pressure drop for all the cylinders (points with asterisks), the pressure drops across the corresponding valves do not equal to zero. Therefore it can be concluded that the boom, arm and bucket cylinders are oversized.

The optimal cylinder piston sizes were determined by tuning the piston sizes until that instant when the maximum pressure drops equaled the supply pressure for

all the cylinders. These values were found to be precisely 52.2mm , 45.1mm and 40.9mm for the boom, arm and bucket cylinders respectively, as shown in Figure 6.19.

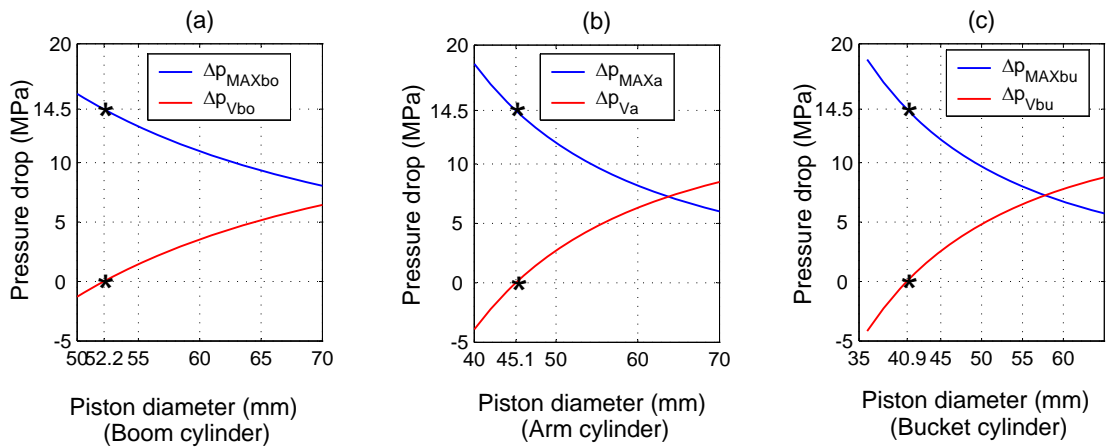


Figure 6.19: The pressure drops versus piston diameters; (a) Boom cylinder
(b) Arm cylinder (c) Bucket cylinder

The resulting pressure drop curves are shown in Figures 6.20 and 6.21.

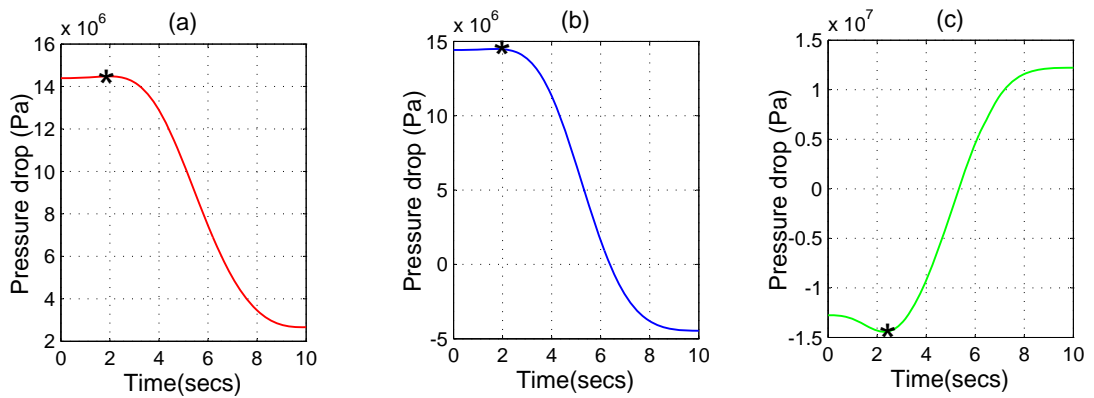


Figure 6.20: The Pressure drop profiles across the cylinders, when the bucket is digging a sandy-loam soil and at optimal piston diameters; (a) Boom cylinder (b) Arm cylinder (c) Bucket cylinder

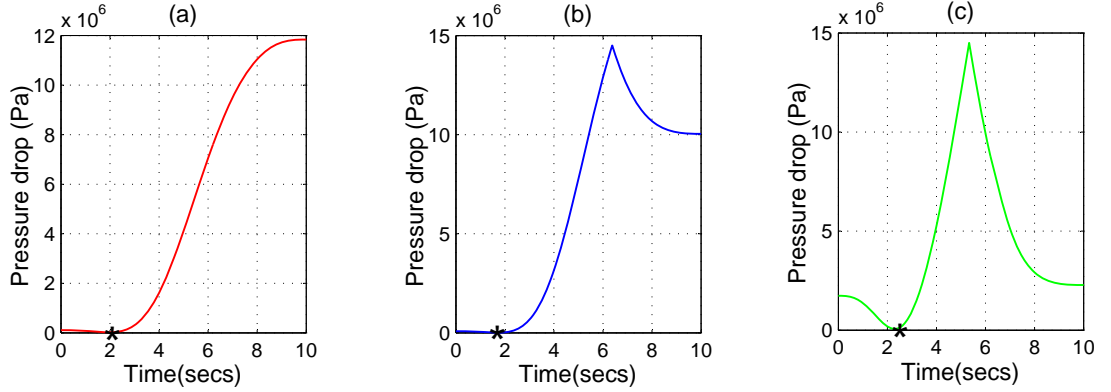


Figure 6.21: The Pressure drop profiles across the cylinder valves, when the bucket is digging a sandy-loam soil and at optimal piston diameters; **(a)** Boom cylinder valve **(b)** Arm cylinder valve **(c)** Bucket cylinder valve

The optimal piston diameters values of the cylinders were rounded to the next imperial values which are available in the market as $2\frac{1}{4}$ " (inches), 2" (inches) and $1\frac{3}{4}$ " (inches) for the boom, arm and bucket cylinders respectively.

6.8.3 Flow Profiles

The fluid flow in the boom cylinder required to produce the desired boom link trajectory, is given by;

$$Q_{bo} = A_{p_{bo}} \dot{x}_{p_{bo}} \quad (6.30)$$

Where Q_{bo} is the flow in the boom cylinder, $A_{p_{bo}}$ is the average area of the boom piston, and $\dot{x}_{p_{bo}}$ is the velocity of the boom piston.

Similarly, for the arm;

$$Q_a = A_{p_a} \dot{x}_{p_a} \quad (6.31)$$

Where Q_a is the flow in the arm cylinder, A_{p_a} is the average area of the arm cylinder

piston, and \dot{x}_{pa} is the velocity of the arm cylinder piston.

Similarly, for the bucket;

$$Q_{bu} = A_{p_{bu}} \dot{x}_{p_{bu}} \quad (6.32)$$

Where Q_{bu} is the flow in the bucket cylinder, $A_{p_{bu}}$ is the average area of the bucket cylinder piston, and $\dot{x}_{p_{bu}}$ is the velocity of the arm cylinder piston.

Figure 6.22 shows the flow in the actuators using a quintic polynomial trajectory for all the joints when the bucket is digging sandy-loam soil and using the sized piston diameters.

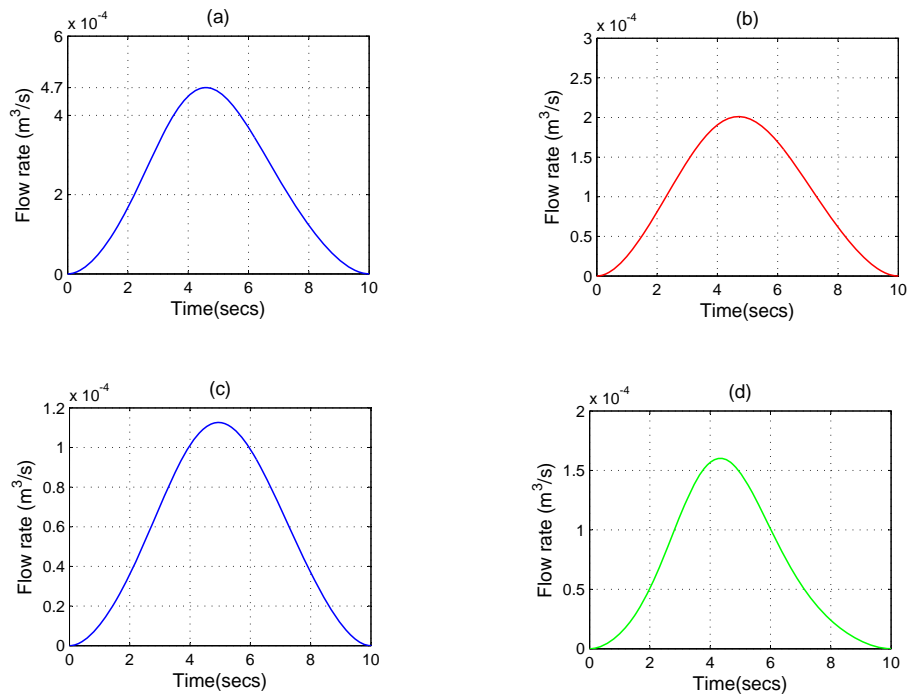


Figure 6.22: (a) Total flow rate profile (b) Flow rate profile to boom cylinder (c) Flow rate profile to arm cylinder (d) Flow rate profile to bucket cylinder

As shown in Equations 6.30, 6.31 and 6.32, the fluid flow to a given cylinder is directly proportional to the linear velocity of the corresponding cylinder piston.

Therefore, the nature of the fluid flow curve is the same with the velocity profile of the corresponding cylinder piston.

The pump flow is the summation of the fluid flow to all the three cylinders since the manipulator links are assumed to move simultaneously. It is also seen that using the pump with the sized flow rate capacity of $4.7 \times 10^{-4} m^3/s$ ($28lit/min$), the engine of the tractor is able to power the excavating mechanism in digging a sandy-loam soil.

6.8.4 Valve Sizing

According to typical industrial practice, valves are selected based on a nominal load and duty cycle. However, no such nominal quantities exist for a manipulator arm whose configuration changes continuously, and may be not loaded, or be loaded on the bucket with scooped media and/or with digging forces. Therefore a systematic methodology for valve sizing is needed.

A valve is properly sized when it can supply the demanded flow at the required pressure drop across it. Therefore to size a valve, flow and pressure requirements must be obtained as a function of time for a given task. Obviously, the task becomes more demanding when the manipulator's bucket is digging a trench.

The flow through the valves for the three actuators is obtained from Equations 6.30 through 6.32, while the pressure drops across the valves is obtained from Equations 6.26 through 6.28. The six equations can be used to plot valve flow versus valve pressure drop for the desired end-point trajectories.

The resulting $Q - \Delta p$ curve should lie below the valve pressure-flow characteristics at full valve opening, $Q_v - \Delta p_v$, typically a curve described by a relationship of the

form;

$$Q_v = C_d A_O \sqrt{\frac{2}{\rho} \Delta p_v} \quad (6.33)$$

Where;

Q_v is the flow rate through a valve.

Δp_v is the pressure drop across the valve.

C_d is the discharge coefficient.

ρ is the fluid density.

A_O is the area of the orifice opening.

If $Q - \Delta p$ curve does not lie below the valve pressure-flow characteristic curve at full valve opening, then the pressure drop across the valve is less since the pressure drop across the actuator is large. Therefore, the valve flow rate is not able to provide the motion to the manipulator at the specified speed at a particular operating pressure. In this case a valve of larger capacity must be specified, or the value of the operating pressure increased. Figures 6.23 and 6.24, show the typical plots of such curves for the two cases.

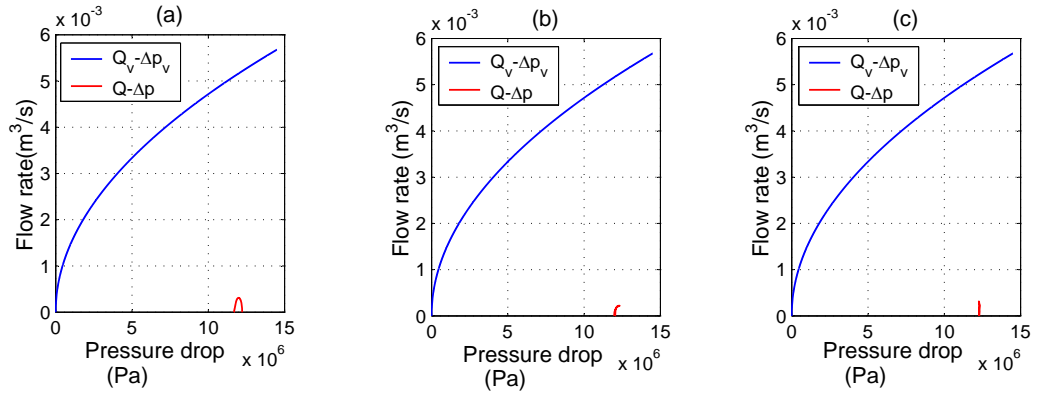


Figure 6.23: Pressure drops versus flow curves, when the manipulator is moving in a free space and at the initial sizes of the valve's orifices; **(a)** Boom cylinder valve **(b)** Arm cylinder valve **(c)** Bucket cylinder valve

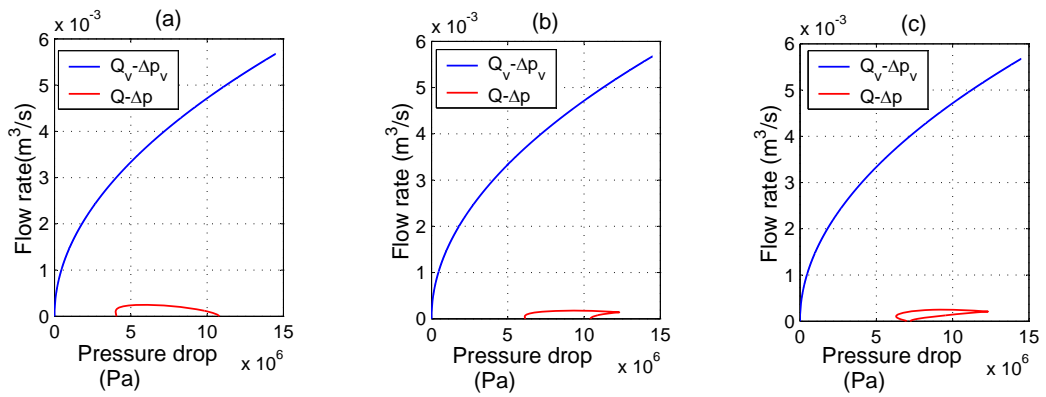


Figure 6.24: Pressure drops versus flow curves, when the bucket is digging a sandy-loam soil and at the initial sizes of the valve's orifices; **(a)** Boom cylinder valve **(b)** Arm cylinder valve **(c)** Bucket cylinder valve

As seen in Figures 6.23 and 6.24, the $Q - \Delta p$ curves for all the cylinder valves and for the two conditions are far below the valve characteristic curves, hence it can be concluded that the manipulator will be able to operate with the selected valves, although the valve orifice ports are seen to be oversized. An optimal orifice port

size should ensure that the peak value of the $Q - \Delta p$ curve is well near the valve characteristic curve.

The optimal orifice port sizes were determined by tuning the radii of the ports until that instant when the peak values of the $Q - \Delta p$ curves for all the valves are well below the characteristic curves. These values were found to be precisely equal to $1.5mm$ for all the cylinder valves. The optimal port diameter values of $3mm$ were rounded to the next imperial values which are available in the market as $\frac{1}{8}$ " (inches). The resulting pressure drop versus flow curves are shown in Figures 6.25 and 6.26 for the two cases.

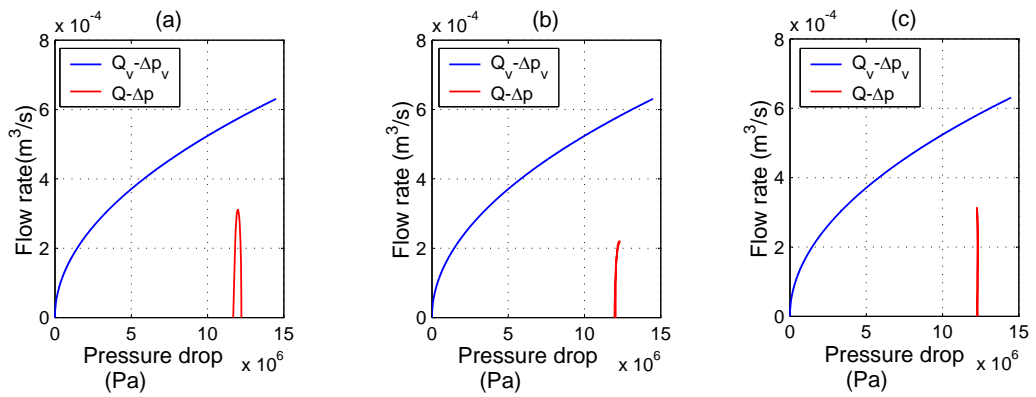


Figure 6.25: Pressure drops versus flow curves, when the manipulator is moving in a free space and at the optimal sizes of the valve's orifices; (a) Boom cylinder valve (b) Arm cylinder valve (c) Bucket cylinder valve

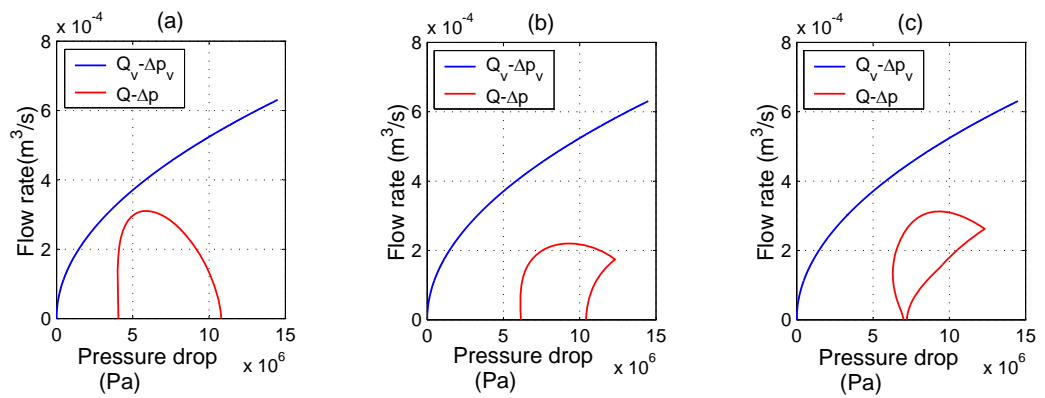


Figure 6.26: Pressure drops versus flow curves, when the bucket is digging a sandy-loam soil and at the optimal sizes of the valve's orifices; (a) Boom cylinder valve (b) Arm cylinder valve (c) Bucket cylinder valve

CHAPTER 7

DYNAMIC RESPONSE USING FORWARD DYNAMICS

7.1 Introduction

One of the main purposes of modeling a dynamic system is to design appropriate control laws for the system. For a system to be controlled, its model should capture the essential dynamic aspects of the system which include but not limited to, the interaction of the domains involved and also the inter-component interactions. The transient and steady state responses of the system were simulated to show the interactions involved in the system. Forward dynamics is concerned with motions which result on a manipulator when the input is the torque at the joints

7.2 Block Expansion

The overall computational bond graph model represented in Figure 5.9 was expanded into block diagrams using the Fakri method [32] which is illustrated in section A.5. The block diagrams were input in a SIMULINK workspace and grouped into subsystems to form a model as shown in Figure 7.1 to 7.3, which form the test bed for all the simulations to be performed in this chapter.

The *hydraulic subsystem block* has piston velocities as the input signal and the cylinder forces as the output signal. When opened this subsystem appears as shown in Figure 7.2. This block also demonstrates the interaction of the hydraulic actuators driving the boom, arm and bucket links. The *hydraulic subsystem block* comprises of the boom, arm and bucket cylinders dynamics.

Each hydraulic cylinder outputs a hydraulic force proportional to the pressure drop

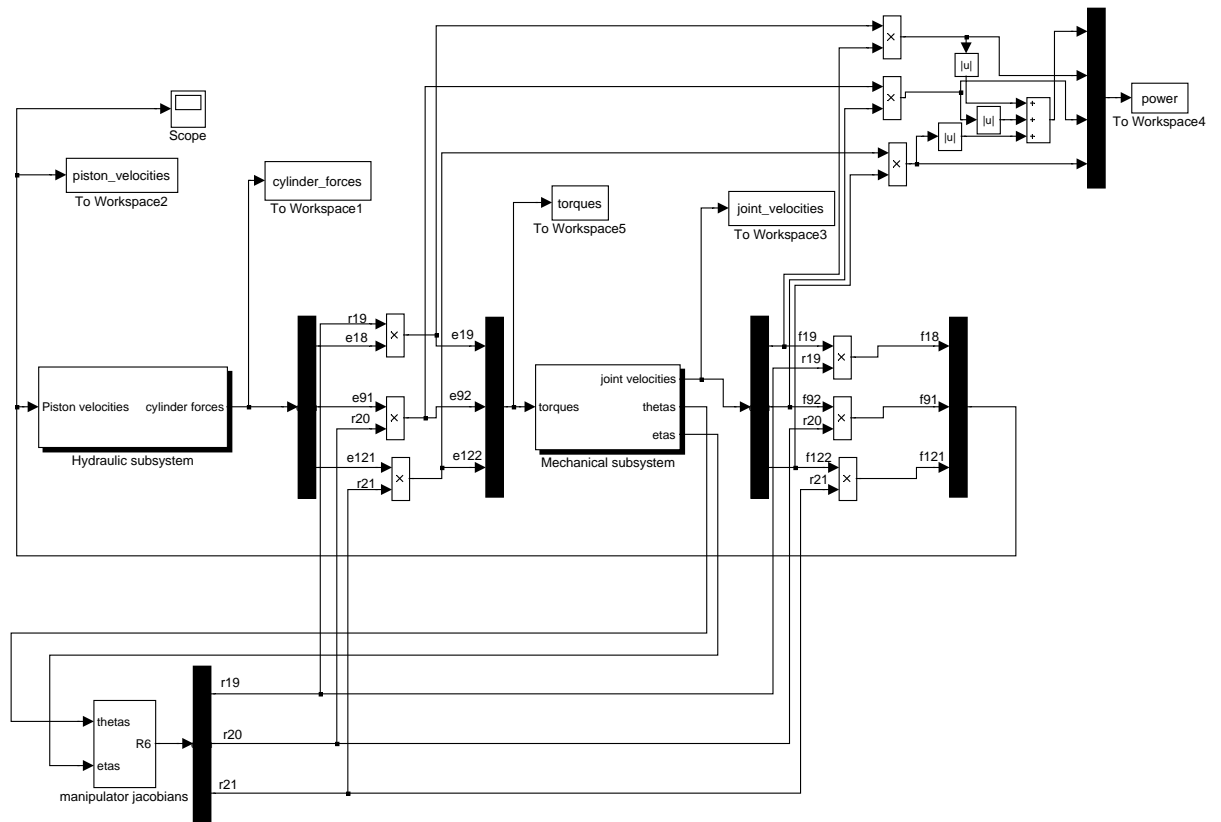


Figure 7.1: The Simulink block diagram representing the bond graph model of the interacting hydraulic and mechanical dynamics

across the cylinder. The boom cylinder, arm cylinder and bucket cylinder forces are denoted as e_{18} , e_{91} and e_{121} respectively. The three force signals are combined into one signal which becomes the overall output signal from the hydraulic subsystem to interact with the mechanical subsystem, as shown in Figures 7.1 and 7.2. The input signal to each of the cylinder block is the inverse of the resistance to fluid flow generated by the directional control valve for each cylinder. As illustrated earlier, these resistances depend with the valve displacement. These valve displacements are considered as the overall input signals to the hydraulic subsystem and they come from the operator.

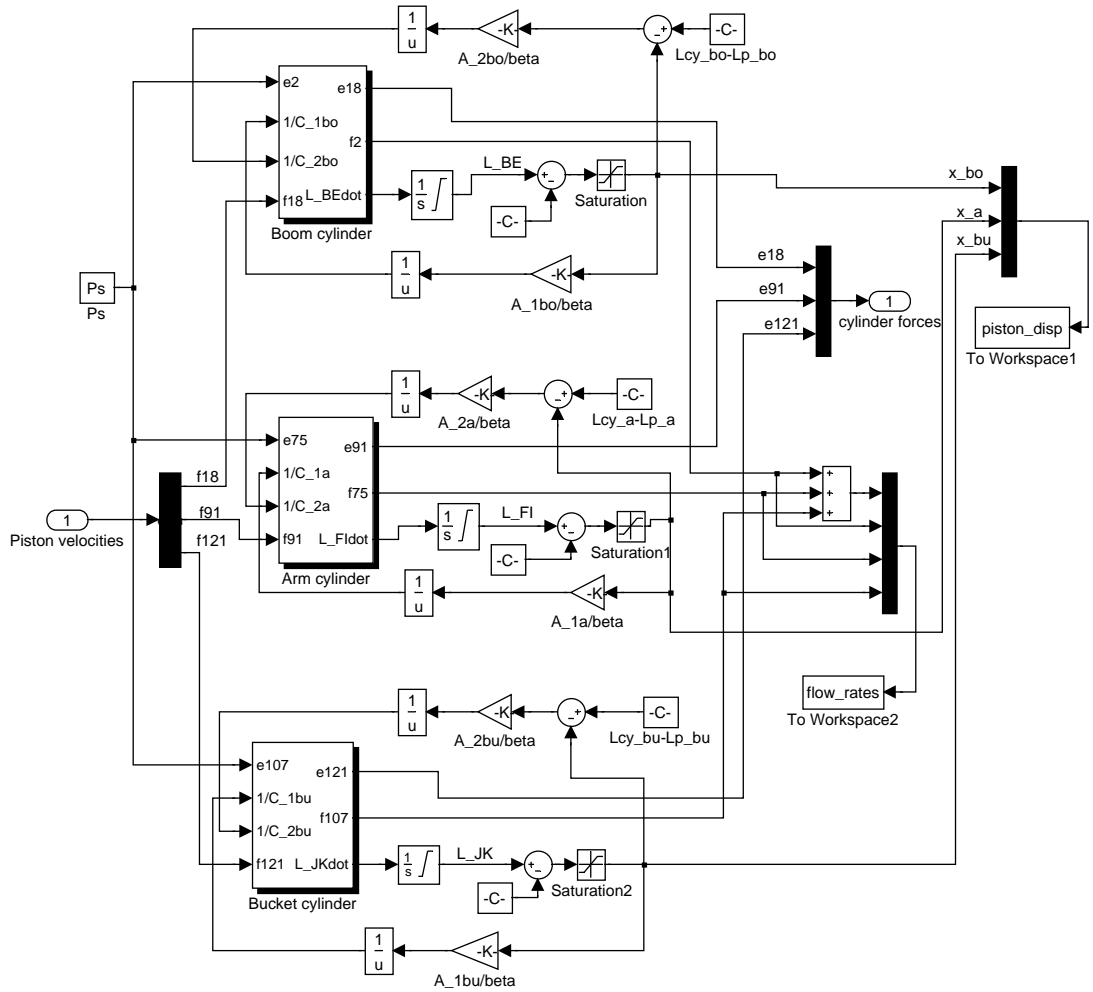


Figure 7.2: The Simulink block for the hydraulic dynamics

As shown in Figure 7.1, the hydraulic cylinder forces are transformed into joint torques by the manipulator Jacobians, which as shown in section 5.2 are modulated transformer ratios denoted as r_{19} , r_{20} and r_{21} for the boom, arm and bucket links respectively. The signals representing these ratios are computed in a *manipulator jacobian block*.

The torque signal obtained by transforming the cylinder force signal using manipulator jacobians is then fed to the *mechanical subsystem block* as an input signal.

Figure 7.3 shows the *mechanical subsystem block* which comprises of blocks representing the mechanical dynamics of the boom, arm and bucket links.

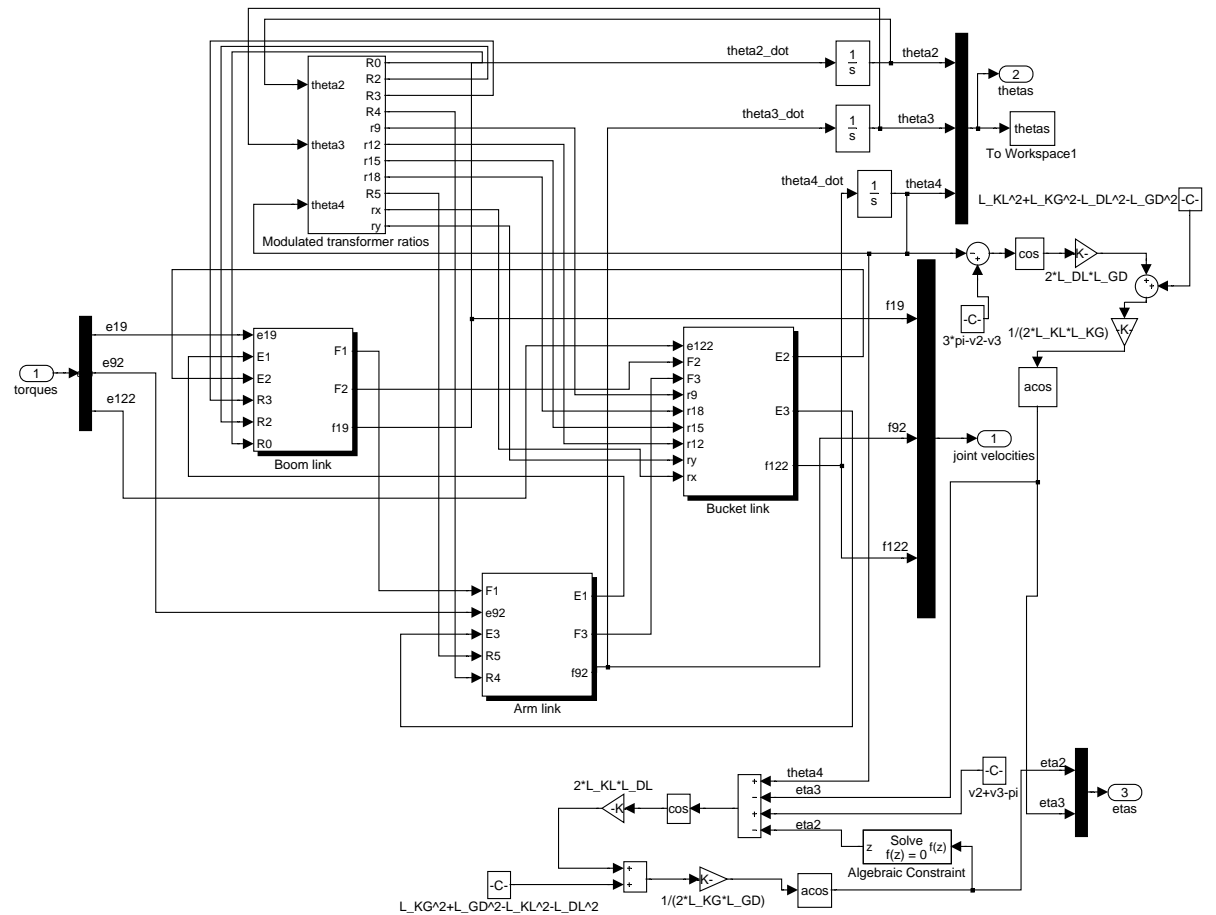


Figure 7.3: The Simulink block for the mechanical subsystem dynamics

Each link block outputs an angular velocity of the corresponding link joint, that is, f_{19} , f_{92} and f_{122} for the boom, arm, and bucket links respectively. The joint velocity signals are combined into one signal which forms the overall output signal from the mechanical subsystem to interact with the hydraulic subsystem, as shown in Figures 7.1 and 7.3. The joint velocities are transformed into piston velocities of the hydraulic cylinders using manipulator jacobians. These piston velocity signals

are input into the hydraulic subsystem and determine the hydraulic fluid flow rate to the actuators. Each joint velocity signal from the link block is integrated to compute the position information for each joint. The initial conditions for the manipulator configuration are given in these integrators. The joint displacements determine the manipulator jacobians and the modulated transformer ratios (r_1 to r_{18}) of the rigid body dynamics of the manipulator. This is the reason why the joint displacements form part of the input signals of the *manipulator jacobians* and *modulated transformer ratio blocks*.

All these SIMULINK blocks have been derived from the causal bond graph model of the excavating mechanism as represented in Figure 5.9. Since the differential causality problem in the bond graph model was addressed, then the ordinary differential equations in the block diagrams are guaranteed to be explicit first order ODES which can be solved by the in build ODE-solvers of the MATLAB/SIMULINK code.

7.3 Transient and Steady-State Responses

The SIMULINK blocks described in section 7.2 were simulated to determine the transient and steady state responses for the displacements, velocities of the cylinder pistons and manipulator links, flow rates to the cylinders and chamber pressures of the cylinders when all the cylinders are extending simultaneously.

During simulations, one of the links, that is the bucket, was stopped suddenly so as to excite the other links as much as possible, and observed if this excitation was felt in the responses of the other links and the hydraulic system. The input commands to the system considered were the orifice opening areas of the spool valves which depend on the spool displacements. Such an input is considered to be a combination

of ramp and step inputs as shown in Figure 7.4. The valve displacements commands come from the operator.

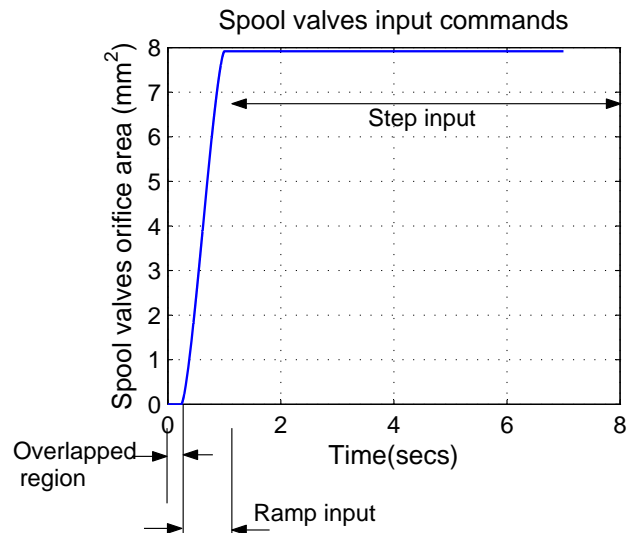


Figure 7.4: The input command to the system

7.3.1 Link Angular Velocity and Displacement Responses

Figure 7.5 shows the simulated responses for the angular displacements and velocities plotted in one axis with two y axes for the three links.

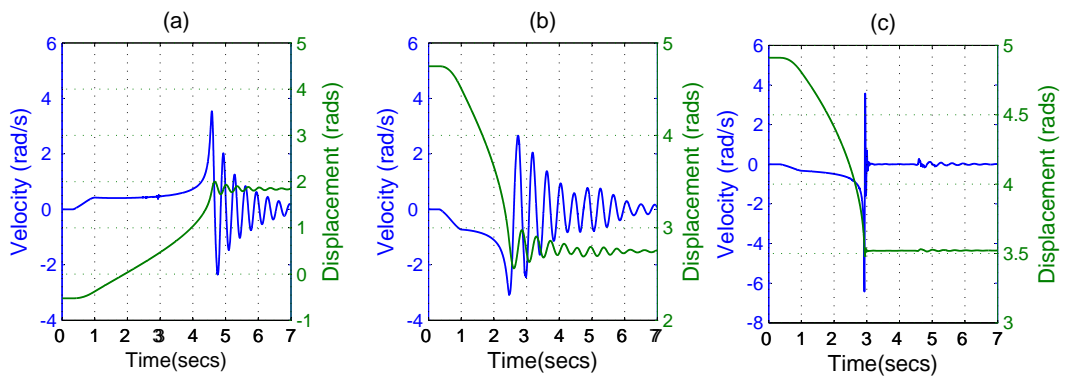


Figure 7.5: The simulated angular velocity and displacement responses for; (a) Boom link (b) Arm link (c) Bucket link

As clearly seen in Figures 7.5 and 7.6, each manipulator link reaches its final angular position after the piston of the corresponding cylinder completes its stroke (for the case of boom and arm) or is stopped (for the case of bucket). Also, after the final angular position is reached, the velocity response curve of the given cylinder drops and settles to zero value as it is expected practically. These response curves show a significant damped oscillations at the settling points. This can be attributed to the springs and dampers which were added to the bond graph model in order to solve the derivative causality problems. The effect of stopping the bucket link suddenly is felt at the velocity response curve of the boom link as an excitement at time 3 seconds as shown in Figure 7.5(a).

7.3.2 Piston Velocity and Displacement Responses

Figure 7.6 shows the simulated responses for the piston displacements and velocities plotted in one axis with two y axes for the three hydraulic cylinders.

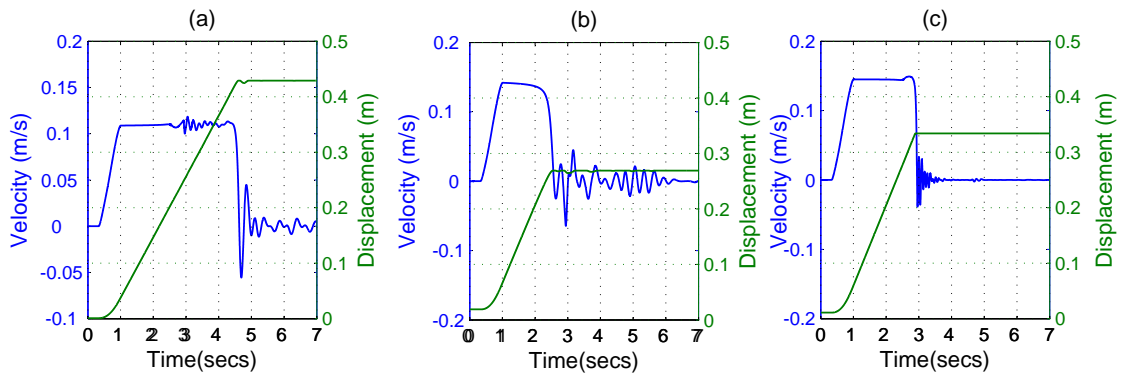


Figure 7.6: The simulated piston velocity and displacement responses for; (a) Boom cylinder (b) Arm cylinder (c) Bucket cylinder

The piston velocity curves have a profile similar to the flow rate response curves due to the fact that flow rate and the piston velocities are related by equation $Q = A_p \dot{x}$,

where Q is the flow rate to the cylinder minus the sum of the internal leakage flow and the compressibility flow. The response curves show clearly that at that time when the piston completes its stroke or stops, the velocity of the piston drops and settles to zero as it is expected practically.

The oscillations occurring in the response curves during settling times can be attributed to the compressibility of the hydraulic oil in the cylinder chambers which during modeling was considered like a spring stiffness. The damping effects to the oscillations can be attributed to the internal leakages in the cylinders which were modeled as R-elements. The effect of stopping the bucket link suddenly is felt at the velocity response curve of the boom cylinder piston as an excitement in form of damped oscillations at times 3 – 4 seconds as shown in Figure 7.6(a).

7.3.3 Flow Rate Responses

Figure 7.7(a) shows the simulated responses for the flow rates of the three hydraulic cylinders plotted in one axis, while Figure 7.7(b) shows the simulated response for the total flow rate.

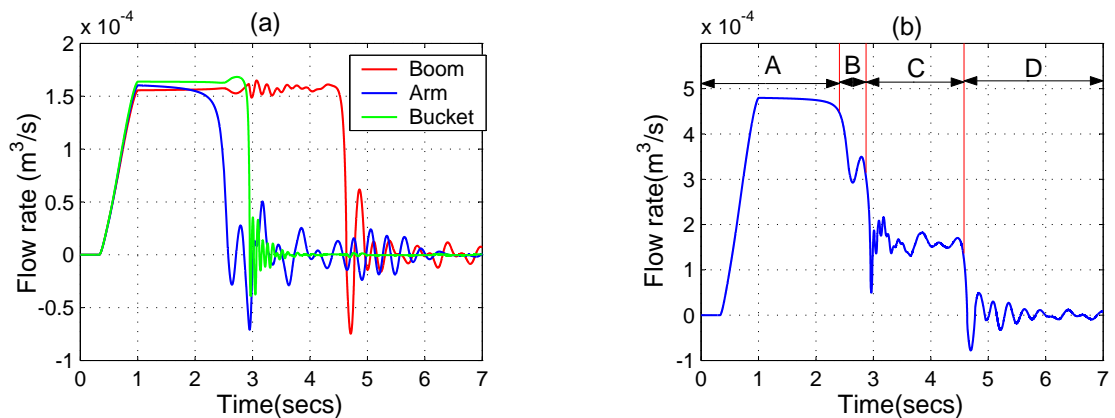


Figure 7.7: The simulated flow rate response; (a) Flow rate responses to individual cylinders (b) Total flow rate

The flow rate responses for all the cylinders reach the steady state value after *1 second*, that is when the spool valve orifices are completely open. The response curve for the boom cylinder which controls the heaviest link has a lowest steady state value, due to the fact that the cylinder moving the heaviest load offers greater resistance to fluid flow, hence the inter-actuator interaction is captured by the model.

The flow rate response curve for the arm cylinder which finishes its stroke first drops to zero value first, then followed by the bucket cylinder which is stopped rapidly after 3 seconds. The excitement caused by stopping the bucket link rapidly is significantly felt at the flow rate response of the boom cylinder at times 3 – 4 seconds as shown in Figure 7.7(a).

Since all the manipulator links are extending simultaneously, the total flow rate response which is the summation of the flows to the actuators is simulated and plotted in Figure 7.7(b). This curve can be divided into four regions, namely A, B, C and D. In *region A* the three cylinders are supplied with fluid flow since they are all moving. This is the region of maximum flow requirement. In *region B* only the boom and bucket cylinders require fluid flow since already the arm cylinder has completed its stroke. In *region C* only the boom cylinder requires fluid flow since the bucket cylinder has been stopped. In *region D* no fluid flow is required since all the links have stopped moving after the boom cylinder has completed its stroke.

7.3.4 Pressure Responses at the Cylinder Chambers

Figure 7.8 shows the simulated pressures in the two chambers of the boom, arm and bucket cylinders plotted in the same axis. It is clearly seen that at the region of ramp input (between 0 and 1 second), the pressures at the two sides of each cylinder

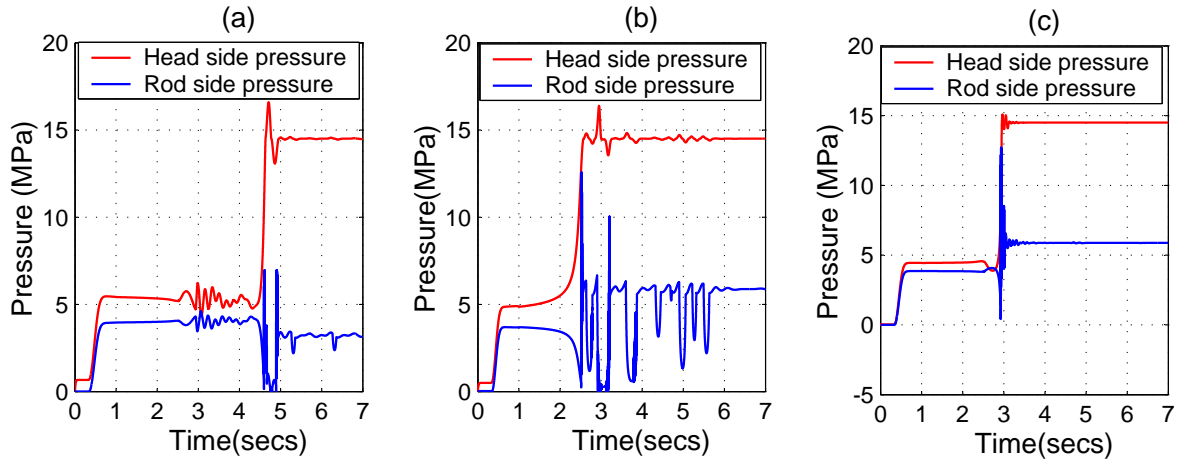


Figure 7.8: The simulated head and rod side pressure responses for; (a) Boom cylinder (b) Arm cylinder (c) Bucket cylinder

increase at the same rate until when the orifices of the valves are completely open. After the cylinder finishes its stroke or is stopped from moving, the pressure at the head side chamber which receives pressurized fluid, increases rapidly to the supply pressure of $p_s = 14.5MPa$. This is because the control action of a constant pressure hydraulic system which ensures that the pressure supplied to the cylinder drops or increases to an appropriate value rather than to the pump supply pressure when the cylinder stroke is finished, was not included in the model. The effect of this is seen in the rod side chamber pressure responses for all the cylinders in form of significant pressure fluctuations.

From the responses plotted, it is seen that the bond graph model developed captures the interactive dynamics, that is, inter-actuator interactions, inter-link interactions and interaction of the hydraulic and mechanical dynamics.

- Inter-actuator interaction is captured since the cylinder actuating the heavier link receives less fluid flow, and the cylinder actuating the lightest link receives

more fluid flow.

- Inter-link interaction is captured since the excitation caused by stopping the bucket link suddenly is witnessed at the response curves of the other links.
- The interaction of the mechanical and hydraulic dynamics is captured since the excitation caused by stopping the bucket link is witnessed at the response curves of the hydraulic system. Also the cylinder actuating the heavier link receives less fluid flow, and the cylinder actuating the lightest link receives more fluid flow.

CHAPTER 8

CONCLUSIONS AND RECOMMENDATIONS

8.1 Conclusions

This research work was primarily concerned with the dynamic modeling of an excavator using the relatively new bond graph method. The dynamic models have been used to size the hydraulic components such as actuators and valves, and to simulate the transient and steady state responses of the system.

The complete excavator model was constructed by modeling the hydraulic actuation system and the manipulator linkage separately, then coupling the two models into a complete model using the manipulator jacobians which were derived through trigonometric analysis. The virtue of bond graphs in modeling multi-domain systems became apparent since the mechanical and hydraulic dynamics of the excavator were modeled using the same method contrary to what dominates the literature, where the mechanical and hydraulic dynamics are modeled using different methods. The mechanical bond graph model of the manipulator was verified by comparing the joint torque expressions of a two link planar manipulator to those obtained by using Newton-Euler and Lagrangian methods as analyzed in robotic textbooks. The expressions were found to agree indicating that the model captures the aspects of rigid body dynamics of the manipulator. Also the bond graph model of the hydraulic system was verified by comparing the open loop state responses to those of an ODE model which has been developed in literature based on the same assumptions. The results were found to correlate very well both in the shape of the curves, magnitude and the response times, thus indicating that the developed model represents the hydraulic dynamics of a valve controlled cylinder.

To develop a mechanical dynamics model of the manipulator, forward recursive equations similar to those applied in iterative Newton-Euler method were used to determine the centroid velocities of the links. This is unlike in Newton-Euler method which requires extra recursive computations to be performed so as to determine the centroid accelerations of the links. In addition, a dynamic model resulted after representing the horizontal and vertical velocities of the links in bond-graphic form, while considering the momenta and weights of the links as the bond graph elements. Newton-Euler method on the other hand requires backward recursion to be performed in order to obtain a dynamic model. This showed that the bond graph method reduces significantly the number of recursive computations required to be performed to a manipulator for a dynamic model to result. It can therefore be concluded that bond graph method is more computationally efficient than the Newton-Euler method in developing dynamic models of manipulators.

Since all the links of the excavating manipulator are driven by hydraulic power, sizing of the hydraulic components become important. Quintic polynomial trajectory was planned for all the links and simulations using inverse dynamics were carried out. Using the pressure drop curves across the cylinders and the valves, the optimal piston sizes for all the cylinders actuating the links were obtained as $2\frac{1}{4}$ " (inches), 2" (inches) and $1\frac{3}{4}$ " (inches) for the boom, arm and bucket cylinders respectively. The flow through a valve, and the pressure drop across it were plotted. This plot was compared with the provided valve characteristic curve to test if the valve under consideration is capable of providing the flow for the motion. Using this methodology, optimal port sizes for all the valves controlling the cylinders were found to be $\frac{1}{8}$ " (inches). The total power requirement for the manipulator was also simulated

for the planned trajectory, and it was found that using a hydraulic pump with the sized flow rate capacity of $4.7 \times 10^{-4} m^3/s$ (*28lit/min*), the engine of the tractor is able to power the excavating mechanism in digging a sandy-loam soil.

Using the optimal design parameters of the hydraulic system, forward dynamic simulations were run to determine the open loop transient and steady state responses of the excavator. The bond graph model developed was found to capture the interactive dynamics, that is, inter-actuator interactions, inter-link interactions and interaction of the hydraulic and mechanical dynamics. This is due to the fact that the excitation caused by suddenly stopping the bucket link during simulation, was felt in the response curves of the other links and also of the hydraulic system. Therefore, it can also be concluded that the dynamic model developed in this work can be applied in designing control laws appropriate in controlling the manipulator motions.

8.2 Recommendations for Future Work

From this research work, the following aspects are suggested for further investigation:

- Inclusion of the swing motion of the manipulator in the model in order to realize full excavating motion using bond graphs.
- Solve the derivative causality in the resulting model of the excavator by transferring the inertial elements of dependent velocities to the ports of independent velocities. This will reduce significantly the time required for simulating the model since the method used in solving the derivative causality in this work (of adding the pad elements) is one of the major reasons behind the longer simulation times.

- When modeling the inter-actuator interaction in this work, it was assumed for simplicity purposes that the supply pressure for all cylinders are equal, although in practice each cylinder in a system of several cylinders operating simultaneously has its own requirement for supply pressure depending on the load and speed required from it. This is the reason why the simulated responses of the head side chamber pressures for all the cylinders indicated a rapid increase to the supply pressure value at the end of a cylinder stroke. Therefore a detailed inter-actuator model which captures this aspect should be developed using bond graphs.
- Use the model developed in this work to design and simulate the controllers for controlling the dynamics and motions of the excavator.
- Fabricate and incorporate the excavating mechanism to the tractor, and subsequently perform experiments which will help to validate the developed models experimentally.

REFERENCES

- [1] Muvengei, O. M., “Design of an Excavating Mechanism to be used with Juja Diesel Tractor JK01,” Tech. Rep., Department of Mechanical Engineering, J.K.U.A.T, 2006.
- [2] Anton, H. H., *Fluid Power handbook: System Applications and Components*, vol. 2. Gulf Publishing Company- Houston, Texas, 1993.
- [3] Ferreira, J. A. Oliveira, J. E. and Costa, A V., “Modelling of the Hydraulic Systems For Hardware-in-the Loop Simulation,” in *Proceedings of the 8th IEEE international Conference*, October 2000.
- [4] Cheol-Gyu, P. and Kwang-Ho, L., “A Simulation Environment for Excavator Dynamics,” Tech. Rep., Daewoo Heavy Industries and Machinery Ltd, Republic of Korea, 2004.
- [5] Beater, P. and Otter, M., “Multi-domain Simulation: Mechanics and Hydraulics of an Excavator,” in *Proceedings of the 3rd International Conference*, pp. 331–340, November 2003.
- [6] Krishnaswamy, K., *Passive Teleoperation of Hydraulic Systems*. PhD thesis, University of Minnesota, May 2004.
- [7] Margolis, D. and Shim, T., “Bond Graph Modelling for Nonlinear Hydromechanical Dynamics in Backhoes,” Tech. Rep., University of Michigan-Dearborn, June 2003.

- [8] Koivo, A. Kacaoglan, E. and Andrade-Celto, J., “Modelling and Control of Excavator Dynamics During digging Operation,” *Journal of Aerospace Engineering*, vol. 9, no. 1, pp. 10–18, 1996.
- [9] Vaha, P. K. and Skibiniewski, M. J., “Dynamic Model of Excavator,” *Journal of Aerospace Engineering*, vol. 6, pp. 148–158, 1993.
- [10] Cannon, H. N., “Extended Earthmoving with an Autonomous Excavator,” Master’s thesis, Robotics Institute, Carnegie Mellon University, Pittsburgh, 1999.
- [11] Nguyen, Hong Q., *Robust Low Level Control of Robotic Excavation*. PhD thesis, Australian Centre for Field Robotics, The University of Sydney, March 2000.
- [12] Zangh, Q. and Duqiang, W., “Modelling and Simulation of an Electrohydraulic Steering System,” in *Proceedings of ASAE/CSAE-SCGR Annual International Meeting*, 1999.
- [13] Paynter, Henry M., *Analysis and Design of Engineering Systems*. MIT Press Publishers, Cambridge, 1961.
- [14] Margolis, D. and Karnopp, D., “Bond Graphs For Flexible Multibody Systems,” *Journal of Dynamic Systems*, vol. 101, pp. 50–57, 1979.
- [15] Denavit, J., and Hartenberg, R. S., “A Kinematic Notation for Lower-Pair Mechanisms Based on Matrices,” *Journal of Applied Mechanics*, pp. 215–221., 1955.
- [16] Fu, K.S. Gonzalez, R. C. and Lee, C.S., *Robotics: Control, Sensing, Vision and Intelligence*. McGraw Hill Book Publishing Company, 1987.

- [17] Craig, J.J., *Introduction to Robotics: Mechanics and Control*. Addison-Wesley Publishers, USA, 1986.
- [18] Luh, J.Y. Walker, M.W. and Paul, R.P, “On-line Computational Scheme for Mechanical Manipulators,” *Journal of Dynamic Systems, Measurement and Control*, vol. 120, pp. 69–76, 1980.
- [19] Udwadia F. E. and Kalaba, R.E., “A New Perspective on Constrained Motion,” in *Proceedings: Mathematical and Physical Sciences, The Royal Society*, pp. 407–410, November 1992.
- [20] Falco, D. Pennestri, E. and Vita, L., “The Udwadia-Kalaba Formulation: A Report on its Numerical Efficiency in Multibody Dynamic Simulation and on its Teaching Effectiveness,” in *Proceedings: Multibody Dynamics, Eccomas Thematic Conference*, June 2005.
- [21] Hollerbach, J. M., “A Recursive Lagrangian Formulation of Manipulator Dynamics and a Comparative Study of Dynamics Formulation Complexity,” in *IEEE Transactions*, pp. 730–736, 1980.
- [22] Book, W. J., “Recursive Lagrangian Dynamics of Flexible Manipulator Arms,” *The Int. Journal of Robotics Research*, vol. 3, pp. 87–101, 1984.
- [23] Lin, J., and Lewis, F. L., “A Symbolic Formulation of Dynamic Equations For a Manipulator With Rigid and Flexible Links,” *The Int. Journal of Robotics Research*, vol. 13, no. 5, pp. 454–466, 1994.

- [24] Tran, D., “ A Presentation of Kane’s Method for Formulating Equations of Motion ,” *Journal of La Recherche Aerospatiale (English Edition)*, no. 3, pp. 1–21, 1991.
- [25] Anand, V., Kansal, H. and Singla, A., “Some Aspects in Bond graph Modeling of Robotic Manipulators: Angular Velocities from Symbolic Manipulation of Rotation Matrices,” Tech. Rep., Department of Mechanical Engineering, Sant Longowal Institute of Engineering and Technology, 2003.
- [26] Karnopp, D.C., Margolis, D. and Rosenberg, R., *System Dynamics: Modelling and Simulation of Mechatronic Systems*. John Wiley and Sons Publishers, New York, 2000.
- [27] Karnopp, D.C. Margolis, D.L. and Rosenberg, R.C., *System Dynamics; A Unified Approach*. John Wiley and Sons Publishers, New York, 2nd ed., 1990.
- [28] Karnopp, D.C. and Rosenberg, R.C., *Introduction to Physical System Dynamics*. McGraw Hill Publishers, Newyork, 1983.
- [29] Breedveld, P., “Bond graphs,” in *Encyclopedia of Life Support Systems, Modeling and Simulation*, June 2003.
- [30] Wellstead, Peter E., *Introduction to Physical System Modeling*. Electronic Publisher, Control System Principles, 2005.
- [31] Gawthrop, P. and Smith, L., *Metamodeling: Bond Graphs and Dynamic Systems*. Prentice Hall International Publishers, UK Limited, 1996.

- [32] Fakri, F., Rocaries, A. and Carrierre, A., “A Simple Method for Conversion of Bond graph Models in Representation by Block Diagrams,” in *Proceedings of the International Conference on Bond Graph Modeling and Simulation*, 1997.
- [33] Dickinson, S. J., “Unified Component Modeling of Dynamic Mechatronic Systems with Bond Graphs,” Tech. rep., Engineering Department, Lanchaster University, UK, Oct. 2004.
- [34] Broenink, J. F., “Introduction to Physical Systems Modeling with Bond Graphs,” Tech. rep., Department of Electrical Engineering, University of Twente, Netherlands, 1999.
- [35] Alekseeva, T. V. and Bromberg, A. A., “Machines for Earthmoving Work, Theory and Calculations,” Tech Rep., Balkema, Rotterdam, 1985.
- [36] Zelenin, A. N. Balovnev, V. I. and Kerov, L. P., “Machines for Moving the Earth,” Tech. Rep., Balkema, Rotterdam, 1986.
- [37] Terzaghi, K., *Theoretical Soil Mechanics*. Wiley Publishers, New York, 1947.
- [38] Reece, A. R., “The Fundamental Equation of Earth Moving Mechanics,” in *Proceedings of Institute of Mechanical Engineers*, 1964.
- [39] Luth, H. J. and Wismer, R. D., “Performance of Plain Soil Cutting Blades in Soil,” in *Transactions of the American Society of Agricultural Engineers*, 1965.
- [40] McKyes, E., *Soil Cutting and Tillage*. Elsevier Publishers, 1985.
- [41] Koivo, A., “Kinematics of Excavator (back hoe) for Transferring Surface Materials,” *Journal of Aerospace Engineering*, vol. 7(1), pp. 7–31, 1994.

- [42] Sanjiv, S., “Learning to Predict Resistive Forces During Robotic Excavation,” Tech. Rep., Field Robotics Centre, Carnegie Mellon University, Pittsburgh, 1996.
- [43] Bin, M., “System Modeling, Identification and Coordinated Control Design for an Articulated Forestry Machine,” Master’s thesis, Department of Mechanical Engineering, McGill University, June 1996.
- [44] Sarkar, S., “Dynamic Modeling of an Articulated Forestry Machine for Simulation and Control,” Master’s thesis, Department of Mechanical Engineering, McGill University, Canada, June 1996.
- [45] Blackburn, R. G and Sheare, J., *Fluid Power Control*. Technology Press of M.I.T and John Wiley Publishers, 1960.
- [46] Merritt, H. E., *Hydraulic Control Systems*. Wiley and Sons Publishers, New York, 1967.
- [47] McCloy, D. and Martin H.R, *Control of Fluid Power: Analysis and Design*. Ellis Horwood Publishers Limited, England, 2 ed., 1980.
- [48] Borutzky, W., “An Energetically Consistent Bond Graph Model of a Double Acting Hydraulic Cylinder,” in *Proceedings of European Simulation Multiconference*, pp. 203–207, June 1993.
- [49] Dransfield, P. and Teo, M. K., “Using Bond graphs in Simulating an Electromechanical System,” *Journal of Franklin Institute*, vol. 308, no. 3, pp. 173–184, 1984.

- [50] Bernard, B. W., “Predicting the Dynamic Response of a Hydraulic System Using Power Bond graphs,” Master’s thesis, Monach University, Melbourne, Australia, October 1983.
- [51] Krishna, M., *Optimal Motion Generation for Hydraulic Robots*. PhD thesis, March 1999.
- [52] Singh, N., “Coordinated Motion Control of Heavy Duty Industrial Machines with Redundancy,” *Journal of Robotica*, vol. 13, pp. 623–633, 1995.
- [53] Margolis, D and Shim, T, “Instability due to Interacting Mechanical and Hydraulic Dynamics in Backhoes,” *Journal of Dynamic Systems, Measurement and Control*, 2003.
- [54] Sagirli, A. Bogoclu, M E. and Omurlu, V E., “Modelling the Dynamics and Kinematics of a Telescopic Rotary Crane by the Bond graph Method (part 1),” *Journal of NonLinear Dynamics*, vol. 33, pp. 337–351, 2003.

APPENDIX A

BOND GRAPH MODELING

A.1 Foundation and Basic Concept of Bond Graphs

The essential feature of the bond graph approach is the representation of energetic interactions between systems and system components, by a single line or energy bond. A bond graph is the combination of bonds, while a bond is a path through which power is flowing from one point to another. Therefore a bond graph shows the flow of power that occurs in a system. The bond is represented as a half arrow indicating the supposed direction of energy flow, between the ports to which it is attached. The bond may be annotated by symbols representing the effort (above the bond) and flow (below the bond) as shown in Figure A.1.

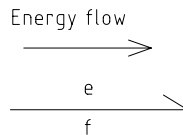


Figure A.1: Bond Representation

Choosing energy as the exchange variable for a model leads naturally to the use of two generalized variables for any dynamic system, which are the effort $e(t)$ and the flow $f(t)$, whose product gives the power flowing between the elements in the system. For example; voltage, pressure, and force are effort variables, while current, flow rate and velocity are the corresponding flow variables. The momentum $p(t)$, and displacement $q(t)$ are the energy variables which are given as [31,34],

$$p(t) = \int e(t) dt \quad (\text{A.1})$$

and

$$q(t) = \int f(t) dt \quad (\text{A.2})$$

The generalized variables for the common individual domains are shown in Table A.1 [31,34].

Table A.1: Generalized variables for each energy domain.

Domain	Flow (f) variable	Effort (e) variable	Generalized displacement variable	Generalized momentum variable
Mechanical translation	Linear velocity, v	Force, F	Linear displacement, $x = \int v dt$	Linear momentum, $M_x = \int F dt$
Mechanical rotation	Angular velocity, ω	Torque, τ	Angular displacement, $\theta = \int \omega dt$	Angular momentum, $M_\theta = \int \tau dt$
Hydraulics	Flow rate, Q	Pressure, p	Fluid volume, $V_f = \int Q dt$	Flow momentum, $\psi = \int P dt$
Thermodynamics	Entropy flow rate, \dot{S}	Temperature, T	Entropy, $S = \int \dot{S} dt$	
Electric	Current, I	Voltage, V	Charge, $q_e = \int I dt$	Lines, $\lambda = \int V dt$
Magnetic	Flux rate, $\dot{\phi}$	MMF, M	Flux linkage, $\phi = \int \dot{\phi} dt$	

A.2 Basic Bond Graph Elements

A.2.1 Energy Sources

The basic bond graph sources are the effort source (SE), and flow source (SF), where the type of the source defines the variable controlled by the source. Examples are external forces, voltage and current sources, ideal motors, hydraulic pumps, etc.

Figure A.2 shows the symbolic representation of SE and SF-elements.



Figure A.2: SE and SF-element representation

Energy sources are ideal in the sense that either the effort or the flow variable is independent of the co-variable. The value of the co-variable is defined by the system which the source supplies. For example, a battery is an effort source and if the system consists of a resistor, then the resistor determines the current (flow variable) from the battery.

Sources can be modulated by another system variable, as is often the case with control systems. Such a source is referred to as a Modulated Effort or Flow Source designated as MSE, or MSF respectively. The constitutive relation for an effort source is $e = e_0$ and for a flow source, $f = f_0$, where e_0 and f_0 are (possibly modulated) constants.

A.2.2 Energy Stores

The two basic bond graph energy storing elements are the flow store and effort store. The flow store element stores energy as the time integral of the flow variable applied

to its port, and is called the capacitive element (*C-element*). Examples of *C-elements* are, the mechanical springs, electrical capacitors, hydraulic fluid compliance, etc. The effort store element stores energy as the time integral of the effort variable applied to its port, and is called the inertial element (*I-element*). Examples of *I-elements* are, mass, fluid inertance, moment of inertia, electrical inductors, etc. Figure A.3 shows the symbolic representation of C and I-elements



Figure A.3: C and I-elements representation

For the effort-accumulating stores (*I-elements*), the general constitutive relation has the form [31, 34];

$$f = \frac{1}{I}\phi(p) \quad (\text{A.3})$$

where $\phi(p)$ is a function of the integrated effort or generalized momentum p given by;

$$p = \int e dt \quad (\text{A.4})$$

In a similar way, the flow-accumulating store (*C-element*) has a general constitutive relation of the form [31, 34];

$$e = \frac{1}{C}\phi(q) \quad (\text{A.5})$$

where $\phi(q)$ is a function of the integrated flow or generalized displacement q given by;

$$q = \int f dt \quad (\text{A.6})$$

A.2.3 Energy Dissipators

Energy dissipators are elements which dump energy out of the system into its environment. A single type of energy dissipator referred to as the resistive element (*R-element*) is required in order to model the basic phenomena encountered in electrical resistors, mechanical friction, etc. The effort and flow variables of the *R-element* are statically constrained by a nonlinear or linear function. Examples of the *R-elements* are, the electrical resistors, mechanical dashpots, orifices, etc. Figure A.4 shows the symbolic representation of R-element.

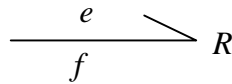


Figure A.4: R-element representation

The constitutive relation for a *R-element* is given as [31, 34];

$$e = Rf \tag{A.7}$$

A.2.4 Junctions

These are the elements which conserve energy and distribute it between other elements in a system. They represent the model structure, and are called multi-ports, indicating that they have two or more ports for transferring energy. The constitutive relation which is common to these elements is that, the sum of all the energy flows into the junction is zero , i.e,

$$e_1f_1 + e_2f_2 + e_3f_3 + \dots\dots\dots + e_nf_n = 0 \tag{A.8}$$

where subscripts 1, 2, 3,, *n* indicate the ports through which the energy is flowing into the element.

In the junction elements, either effort or flow variable is fixed and the co-variables must therefore sum to zero according to the energy conservation Equation A.8. This implies that there are two types of junctions (*i.e effort and flow junctions*) because either the effort or the flow variable may be fixed at a specific junction.

Figure A.5 shows the symbolic representation of an effort junction, which is also called 0-junction. In a 0-junction, the efforts are equal and the algebraic sum of the flows is always zero [31, 34], that is,

$$e_1 = e_2 = e_3 \quad (\text{A.9})$$

and

$$f_1 + f_2 + f_3 = 0 \quad (\text{A.10})$$

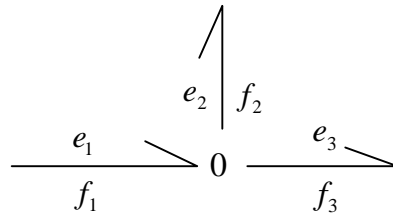


Figure A.5: 0-junction representation

Figure A.6 shows the symbolic representation of a flow junction, which is also called 1-junction.

In a 1-junction, the flows are equal and the algebraic sum of the efforts is always zero [31, 34], that is,

$$f_1 = f_2 = f_3 \quad (\text{A.11})$$

and

$$e_1 + e_2 + e_3 = 0 \quad (\text{A.12})$$

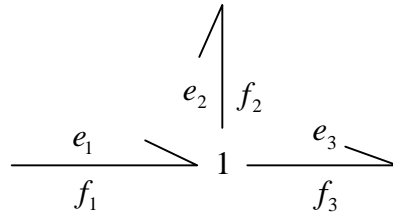


Figure A.6: 1-junction representation

A.2.5 Transformer and Gyrator Elements

If the energy transfer element also transforms one of the effort or flow variables, then the co-variables must be transformed such that the energy conservation relationship in Equation A.8 still holds. Figure A.7 shows the representation of the such elements which are categorized as either transformer (*TF-element*) or gyrator elements (*GY-element*).



Figure A.7: Transformer and Gyrator element representation

A *TF-element* has a constitutive relation where the efforts on the two ports are constrained by the relationship [31, 34],

$$e_1 = r e_2 \quad (\text{A.13})$$

where the transformer ratio r , is either a constant or may be dependent on some other system variable, resulting to a Modulated Transformer (*MTF-element*). For energy conservation to hold at any instant we have

$$e_1 f_1 - e_2 f_2 = 0$$

$$f_2 = r f_1 \quad (\text{A.14})$$

Physical examples of transformer elements are, mechanical lever, hydraulic cylinder piston, a two-port electrical transformer, etc.

A *GY-element* has a constitutive relation where the input effort and the output flow are constrained by the relationship [31, 34],

$$e_1 = n f_2 \quad (\text{A.15})$$

where the gyrator ratio n , is either a constant or may be dependent on some other system variable, resulting to a Modulated Gyrator (*MGY-element*). For energy conservation to hold at any instant we have

$$\begin{aligned} e_1 f_1 - e_2 f_2 &= 0 \\ e_2 &= n f_1 \end{aligned} \quad (\text{A.16})$$

Physical example of transformer elements is the fixed field DC motor where the back electro-magnetic field (e.m.f) generated is proportionally related to the motor shaft speed by the motor gyrator ratio, and the input current is related to the load torque by the same constant.

A.3 Causality in Bond Graph Model

Causal analysis is the determination of the signal direction of the bonds. Causal analysis is in general completely covered by modeling and simulation software packages that support bond graphs. Therefore in practice causal analysis need not be done by hand. Besides derivation of state equations, causal analysis can give insight into the correctness and competency of the model.

A short stroke called causal stroke perpendicular to the bond at one of its ends as shown in Figure A.8 indicate the computational direction of the effort variable.

Accordingly, the other end so called the open end of the bond represents the computational direction of the conjugate flow variable. The position of the causal stroke is completely independent of the position of the half arrow that indicates the direction of power in the bond.

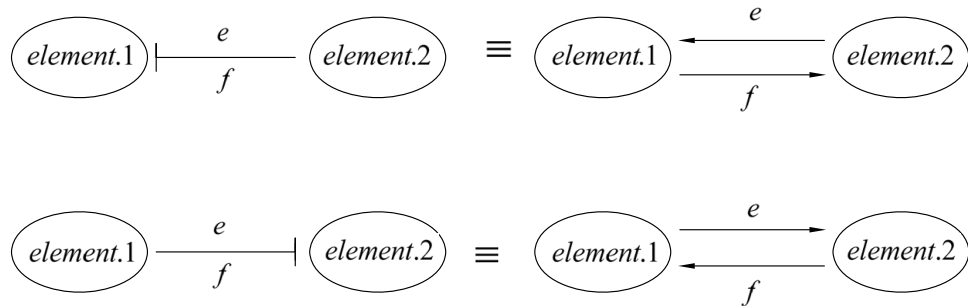


Figure A.8: Definition of the causal stroke

A.3.1 Causal Port Properties

Each type of port has a certain causal property. The following main classes of causal port properties [27, 31, 34] can be distinguished and are shown in Table A.2,

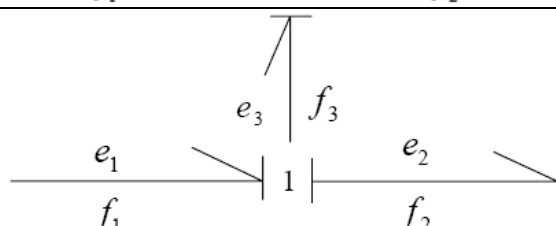
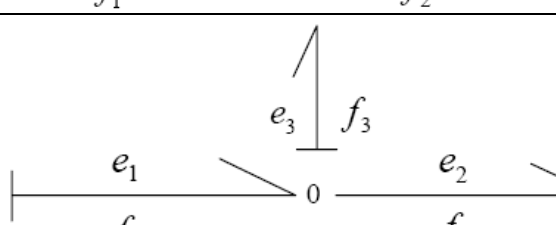
- Ports with *fixed causality* - There is only one option for causality by definition. Examples are the *SE*-element with fixed effort-out causality, and the *SF*-element with fixed flow-out causality.
- Ports with *preferred causality* - For some reason, depending on the type of model manipulation, a causal form can have preference. The most common example is the preferred integral causality of storage ports (*I*-element and *C*-element). This is because numerical integration is preferred over numerical differentiation during simulation.

- Ports with *arbitrary or free causality* - In some cases causality can be chosen at will. Example is the R -element whose causality can be chosen at will in order to complete causality in a model.
- Ports with *causal constraints* - Multi-port elements can have causal constraints between their ports. Examples are the;
 - 1-junction : only one port with effort-in causality is allowed.
 - 0-junction : only one port with flow-in causality is allowed.
 - TF -element : One effort-out and one flow-out causality is allowed.
 - GY -element : Either two effort-out causalities or two flow-out causalities is allowed.

A.3.2 Causality Assignment

Based on the above causal port properties, all sorts of causality assignment algorithms can be applied for different purposes. The common purpose is to write the model equations in a form suitable for simulation, i.e., maximizing the number of storage ports with integral causality.

Table A.2: Causal properties for bond graph elements.

Causal property	Bond graph elements	Bond graph representation
Fixed causality	SE-element	$SE \xrightarrow[e]{f}$
	SF-element	$SF \xleftarrow[e]{f}$
Preferred causality	C-element with integral causality	$\xrightarrow[e]{f} C$
	I-element with integral causality	$\xleftarrow[e]{f} I$
Free causality	R-element with flow-in causality	$\xrightarrow[e]{f} R$
	R-element with flow-out causality	$\xleftarrow[e]{f} R$
Causal constraint	Transformer element with effort out-flow out causality	$\xrightarrow[e_1]{f_1} TF:r \xleftarrow[e_2]{f_2}$
	Transformer element with effort in-flow in causality	$\xleftarrow[e_1]{f_1} TF:r \xrightarrow[e_2]{f_2}$
	Gyrator element with flow in-effort out causality	$\xrightarrow[e_1]{f_1} GY:n \xleftarrow[e_2]{f_2}$
	Gyrator element with effort in-flow out causality	$\xleftarrow[e_1]{f_1} GY:n \xrightarrow[e_2]{f_2}$
	1-junction	
	0-junction	

The most common algorithm is called Sequential Causality Assignment Procedure, which involves the following steps [29,31,34];

1. If there is an energy source element in the bond graph model, assign a fixed causality to it and propagate this along the nodes with causal constraints until propagation terminates due to multiple possibilities. Repeat this step until all energy source ports are augmented with fixed causality.
2. If there is an energy store element in the bond graph model, assign a preferred causality to it and propagate this causality along the nodes with causal constraints until propagation terminates due to multiple possibilities. Repeat this step until all storage ports are augmented with integral causality.
3. If not all ports are causal at this point, there exists at least two ports with arbitrary causality, resulting in a number of possibilities that all will lead to causal paths between ports of elements that are described by algebraic constitutive relations thus causing algebraic signal loops. Choose the causality of these ports not only in such a way that the number of algebraic loops is minimized, but also in such a way that the loop gains of these algebraic loops are smaller than one as much as possible.

A.3.3 Integral and Derivative Causality

The energy storing elements contain information about the system inputs and state variables p and q , thus permitting the system dynamics to be fully represented. The emphasis in bond graph literature has been on the transformation of graphs to state equations. When a bond graph model is transformed into its state equation form, the causality of interest for energy stores is termed as integral causality, where the constitutive relations of the energy stores are in the form given in Table A.3. A mixture of integral and derivative causality may occur in real physical systems,

but only those stores exhibiting integral causality result to state variables. This implies that the order of the set state of equations is smaller than the order of the system. Therefore causal analysis results in an explicit computational model which can easily be computed numerically. Three methods are available in literature which have been successfully applied in solving any differential causality which may arise in a system's bond graph model.

- Add elements - The decision to neglect certain elements in the system is withdrawn. This method was used in [34] to solve the derivative causality in an electro-motor hoisting device's bond graph model.
- Use of pad elements - Pad elements are normally representation of missing or unknown stiffness in the system. This method is applied to mechanisms and manipulators. Padded models though ensuring integral causality, may result to stiff ordinary differential equations which slows down the simulation process. This method was proposed in [26] and was successfully applied in [53] to address the derivative causality in a bond graph model of a backhoe.
- Transforming the inertial elements of dependent velocities to the ports of independent velocities. This method was successfully applied in [54] to address the derivative causality problem in a bond graph model of a telescopic rotary crane.

A.4 Generation of Equations

A causal bond graph contains all information to derive the system dynamical equations in either transfer function or state space form. However the most natural form

in which to frame the equations of motion for bond graph purposes is the state space description. For fairly small bond graphs, the state space description can be obtained in straightforward manner by hand, but for larger systems the algorithm becomes so tedious and complex such that bond graph softwares such as, ENPORT, MSI, CAMP-G and 20-SIM are used to obtain the state space equations of the model.

The following procedure is used to generate state equations from a bond graph;

- Using the constitutive relations of all the elements in computational form, develop the set of mixed differential and algebraic equations. This comprises of $2n$ equations of a bond graph having n bonds. n equations compute efforts and n equations compute flows, or derivatives of them.
- Eliminate the algebraic equations, and substitute the summation equations of the junctions into the differential equations of the storage elements to get m state equations where m is the number of energy storage elements in the model.

A.5 Block Diagram Expansion

Since a causal bond graph represents a bi-lateral signal flow with fixed directions, it can always be expanded into a block diagram. The most common procedure is the Fakri [32] method, which is presented in Table A.3 for every individual bond graph element.

Table A.3 (Contd): Block diagram expansion for bond graph elements

Table A.3: Block diagram expansion for bond graph elements

Element	Bond graph representation	Constitutive Relations	Block diagram expansion
C-element with integral causality		$e = \frac{1}{C_1} q$ $q = \int f dt$	
I-element with integral causality		$f = \frac{1}{I_1} p$ $p = \int e dt$	
R-element with flow-in causality		$e = R_1 f$	
R-element with flow-out causality		$f = \frac{1}{R_1} e$	

A.6 Simulation of a Bond Graph Model

Once an explicit computational model is arrived at, simulation of the system states can be done using either of the following procedures;

- The state equations derived from the model using procedure in section A.4

Transformer element with effort out-flow out causality		$e_1 = re_2$ $f_2 = rf_1$	
Transformer element with effort in-flow in causality		$e_2 = \frac{1}{r}e_1$ $f_1 = \frac{1}{r}f_2$	
Gyrator element with flow in-effort out causality		$e_2 = gf_1$ $e_1 = gf_2$	
0-junction		$e_1 = e_2 = e_3$ $f_3 = f_1 - f_2$	
1-junction		$f_1 = f_2 = f_3$ $e_3 = e_1 - e_2$	

can be solved using the in-built ODE-solvers of the MATLAB software.

- The block diagram expansion of the bond graph model obtained using rules in section A.5 can be input using click-and-drag in a SIMULINK workspace

and the system states simulated.

- The causal bond graph model obtained using procedures in section A.3 can be input in the workspace of one of the softwares supporting the bond graphs using click-and drag way, and the states simulated. Such softwares are; CAMP-G, 20-SIM, ENPORT, TUTSIM, SYMBOL-90 among others.